

Dublin City University

School of Mechanical and Manufacturing Engineering

A Thesis Presented For The Degree Of Doctor Of Philosophy

Development of a Microfluidic Device and Imaging System for the Monitoring of Anti-platelet Therapy

by

Peter M. McCluskey B.Eng

Supervisors: Dr. Brian G. Corcoran

Dr. Nigel J. Kent

September, 2015

Declaration

I hereby certify that this material, which I now submit for assessment on the programme of study leading to the award of Doctor of Philosophy is entirely my own work and has not been taken from the work of others save and to the extent that such work has been cited and acknowledged within the text of my work.

Signed: _____ (Candidate) ID No. _____

Date: _____

”The trouble with having an open mind, of course, is that people will insist on coming along and trying to put things in it.”

Terry Pratchett

Acknowledgements

This body of work would not have been possible without the team at the Biomedical Diagnostics Institute (BDI), Royal College of Surgeons in Ireland and my supervisors Brian Corcoran and Nigel Kent. Brian Corcoran, your ability to guide me through the maze that is the academic world and explain problems and identify the fundamental issues with such clarity, was of immeasurable benefit over the last few years. Nigel Kent, Thank you for putting up with the crazy ideas and the late night emails. Unlike flow rate within a microfluidic channel, your help when problems occurred, and guidance during the writing of this thesis cannot be measured.

The CVD1/CVD2 team, you know who you are. I've enjoyed working with you all for the past few years and look forward to working with you all again in the future. Dermot Kenny, your guidance and attention to detail was always challenging and helped make my research more robust. Tony Ricco, your willingness to assist and breadth of knowledge across seemingly unrelated topics was invaluable. An extra special thank you goes to Niamh Gilmartin and Bincy Josek with whom I spent so much time, and without whom it would not feel like I started this journey only last week.

And finally a big thank you to Rramji Lakshmanan, who sat next to me, and therefore had to put up with me.

Thanks must also go to my family and friends. To James for making me the late night dinners and putting up with the mess of papers and “stuff I’m working on”. To Lina, you have stood by me and supported me from the start and not once complained about the late nights, sitting and writing for hours, and everything else that goes along with a PhD. Lina “never met anybody sillier than me till I met you”.

And finally, for real this time. Thank you everyone for supporting me when I was sick, you all made a hard time so much easier.

Thanks also to the Science Foundation Ireland for funding this work: This work was supported by Science Foundation Ireland under Grant No. 10/CE3/B1821.

Abstract

This work details the development of two distinct prototype point-of-care diagnostic systems to be used to determine the efficacy of anti-platelet therapies. Novel microfluidic chips were designed for each system, to enable the on-chip testing of multiple anti-platelet therapies. The prototypes work with whole blood and integrate with a new detection method used to determine the percentage of platelets adhered to an array of fibrinogen spots. The system uses customised image analysis software to objectively quantify single platelet binding events from a single blood sample, without the need to add any form of labelling to the blood. The system was validated by comparing the percentage of platelets adhered from ‘normal’ blood samples compared to samples treated with an established platelet therapy. These treatments inhibit a specific receptor on the platelet surface, thus interfering with stable adhesion to fibrinogen, rendering platelets “less sticky”. This prototype point-of-care device could allow for the automated testing of large numbers of patient samples, potentially diagnosing individuals at risk of suffering a cardiovascular event or undiagnosed bleeding disorder.

Contents

Abstract	vi
Contents	i
Abbreviations	v
1 Introduction	1
1.1 Platelets	2
1.1.1 Platelet Response to Vascular Injury	2
1.1.2 Anti-Platelet Therapies	5
1.2 Platelet Function Analysis	5
1.2.1 Summary of Devices	12
1.3 Individual Platelet Adhesion (iPA)	13
1.3.1 Labelling Used Within iPA Assay	15
1.4 Microfluidic Channels And MEMS Development	16
1.4.1 BioMEMS for Cell Based Analysis	20
1.5 Fabrication	21
1.6 Thesis Aims and Objectives	27
Bibliography	29
2 Theoretical Background	38
2.1 Fluid Flow Within Channels	40

2.1.1	Steady Flow Between Parallel Plates	40
2.1.2	Degas-Driven Flow Model	43
2.1.3	Rocking Table	47
Bibliography		51
3	Characterisation Of Degas-Driven Flow	53
3.1	Principles Of Degas Driven Flow	55
3.2	Manufacture of PDMS Chip	57
3.3	Flow Rate Detection Software	59
3.3.1	Analyses of Complex Channel Geometries	61
3.3.2	Summary	63
3.4	Characterisation of DDF Flow	64
3.4.1	Discussion and Conclusion	71
Bibliography		72
4	Degas-Driven Device Design	74
4.1	DDF Shear Results in Whole Blood	74
4.2	Design of DDF Devices to Integrate iPA	77
4.2.1	Effect of Anti-platelet Drugs Use of iPA	83
4.2.2	Discussion of Results	84
4.2.3	Conclusions	86
Bibliography		88
5	Integration of an iPA assay into a Prototype Device for Point-of-Care	90
5.1	Introduction	90
5.2	Optimisation of the iPA Assay	91
5.3	Prototype Design	98

5.3.1	Research Chip	101
5.4	Design of Integrated Chip	104
5.5	Summary	109
5.6	Discussion And Conclusions	110
	Bibliography	112
6	System Automation	113
6.1	Introduction	113
6.1.1	MATLAB Software	114
6.2	Matched Feature Methods	115
6.3	Label-Free Detection	120
6.3.1	Characterisation of Spot for LFD	120
6.3.2	Results	125
6.3.3	Conclusions	126
	Bibliography	128
7	Conclusions	129
7.0.4	Future Work	131
	Bibliography	133
A	Platelet Surface Receptors	135
B	Biological Background	137
B.0.5	Materials Used	137
B.0.6	Patterning on Poly(cycloolefin) Sheet	138
B.0.7	Blood Collection and Sample Preparation	139
C	Equations of Motion	140
C.1	Conservation of Mass	140

C.2	Equations of Linear Momentum	142
D	Flow Detection Software	147
D.1	Software Overview	147
D.2	Simple Channel Detection	149
D.3	Complex Channel Detection	151
E	Mini Individual Platelet Adhesion (MiPA) Unused Chip Designs	155
E.1	Movement Of Rocking Table	155
E.2	Comparison of Substrates Used With iPA	156
E.3	Integrated Chip Designs	157
F	Detection Software Principles	163
F.1	Blob Analysis	163
F.1.1	Spot Region Detection	166
	List of Figures	169
	List of Tables	181

Abbreviations

AAEP	The Average Area Of Exposed PDMS
ADP	Adenosine Diphosphate
AMFM	Automated Matched Feature Method
APTES	3-Aminopropyltriethoxysilane
ARCTIC	Adjust Antiplatelet Therapy For Coronary Stenting
BioMEMS	Bio-Microelectromechanical
CAD	Computer-Aided Design
CADP	Collagen And ADP
CCFD	Complex Channel Flow Detection
CEPI	Collagen And Epinephrine
CFD	Computational Fluid Dynamics
CLR	Common Language Runtime
CMOS	Complementary Metal-Oxide-Semiconductor
CoG	Centre Of Gravity
COiPA	Chip Optimised Individual Platelet Adhesion
COP	Cyclic Olefin Polymer
CVD	Cardiovascular Disease
DDF	Degas Drivenow
DXF	Drawing Exchange Format
ECM	Extracellular Matrix
FPA	Foot Print Area
GRAVITAS	Gauging Responsiveness With A Verifynow Assay Impact On Thrombosis And Safety
HPF	High-Pass Filter
HPS	Hermansky-Pudlak Syndrome
iPA	Individual Platelet Adhesion
LFD	Label-Free Detection
LoaC	Lab-On-A-Chip
LOG	Laplace Of Gaussian

MEMS	Microelectromechanical Systems
MFM	Matched Feature Methods
MiPA	Mini Individual Platelet Adhesion
MPF	Mid-Pass Filter
PDMS	Polydimethylsiloxane
Plavix	Clopidogrel
PMMA	Polymethylmethacrylate
POCT	Point-Of-Care Test
PPF	Parallel Plate Flow
PPP	Platelet Poor Plasma
PRP	Platelet Rich Plasma
PRU	Platelet Reaction Units
PSA	Pressure Sensitive Adhesive
PSD	Primary Secretion Defects
RBC	Red Blood Cells
RGB	Red Green Blue
SDK	Software Development Kit
SIMBAS	Stand-Alone Self-Powered Integrated Microfluidic Blood Analysis System
SPD	Storage Pool Disease
TEG	Thromboelastography
uCP	Micro-Contact Printing
VWD	Von Willebrand Disease
VWF	Von Willebrand Factor

Chapter 1

Introduction

Cardiovascular disease (CVD) is the leading cause of death and disability in the world [1], within the EU alone 1.9 million deaths were attributed to CVD with an estimated cost to the economy of almost 196 billion Euro a year [2]. 54% of this 196 billion is due to health care costs, 24% due to productivity losses and 22% due to the informal care of people with CVD [2]. Individuals with high blood pressure, high cholesterol, obesity, physical inactivity, unhealthy diets and diabetes all have an increased chance of developing CVD and thereby suffering a cardiovascular event [3]. Heart attack and stroke are the most prevalent cardiovascular events and occur as a result of the formation of thrombosis i.e. a clot that blocks the flow of blood in the heart or brain.

Individuals at increased risk of suffering a cardiovascular event such as a heart attack or stroke are routinely treated with anti-platelet therapies such as acetylsalicylic acid (Aspirin), while clopidogrel (Plavix) is also used alongside Aspirin for the prevention of thrombosis after placement of an intracoronary stent [4]. Although clopidogrel is a highly effective anti-platelet therapy, it has been shown that there is a wide inter-individual variability of response to clopidogrel, with about one-third of patients treated exhibiting

a suboptimal inhibition of platelet function (increasing the risk of thrombosis) [5]. The ability to tailor drug treatments based on the results of a cost effective, standardised and clinically relevant device for testing of platelet function, could reduce the risk of cardiovascular events in at-risk groups [6]. There is potential for anti-platelet tests to be used for diagnostic applications, where test results may indicate further investigation or treatment with an antiplatelet therapy is required. Devices have been demonstrated that can monitor platelet function but to date these assays are utilised as laboratory research tools and have not being adequately developed for point-of-care use [7, 8].

1.1 Platelets

The human platelet has approximate dimensions of between $2\ \mu m$ to $4\ \mu m$ by $0.5\ \mu m$. Their mean volume is between $7\ fL$ and $11\ fL$. [9]. Platelets are the second most numerous corpuscles in whole blood with between 150 and 450×10^9 per litre, in a normal sample of blood. Platelets are anucleated cells that typically circulate for 10 days. Whole blood platelets tend to concentrate near the wall while red blood cells (RBC) remain in the centre of the flow [10]. This places the platelets at the optimum location to respond to damage at the vessel wall, allowing for the formation of a haemostatic plug or thrombus [10].

1.1.1 Platelet Response to Vascular Injury

Platelets play a vital role by stemming blood loss (haemostasis) and initiating tissue healing in response to damage to the endothelial cells that line the vascular wall. Platelets within a healthy individual circulate through the blood vessels, without the need to interact with one another or with the

vascular wall. The term haemostasis comprises all the acute response mechanisms that are initiated to stop bleeding when blood vessels are damaged. During the primary haemostatic response there are three distinct stages a platelet will pass through, Activation, Adhesion and Aggregation. Figure 1.1 shows a cross-section of a blood vessel with both red blood cells and circulating platelets highlighted. When a platelet comes into contact with an area of damaged endothelial cells, surface receptors cause the platelet to become activated. Once the platelet is activated, it will adhere to the damaged area and begin to recruit more circulating platelets that in turn start to aggregate, thereby beginning the formation of a haemostatic plug.

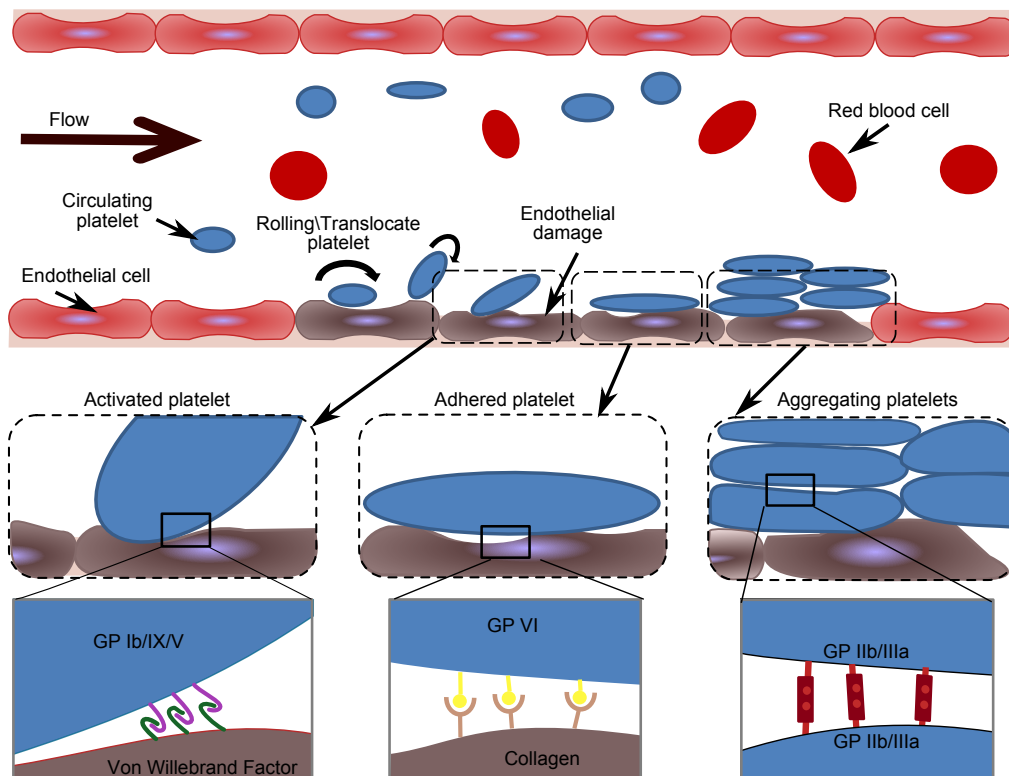


Figure 1.1: A cross-section of a vessel with vascular damage showing platelets in their different states of response seen during vascular injury.

Activation

When damage occurs at the wall of the blood vessel Von Willebrand Factor (VWF) becomes exposed on the surface of the damaged sub-endothelium. Platelets are initially bound to this damaged surface via interactions between VWF and Glycoprotein (GP Ib/IX/V) resulting in the activation of the platelet [11]. The interaction between the platelets and damaged endothelium slows the platelets and causes a characteristic translocating or rolling of the platelets along the damaged surface (Figure 1.1).

Adhesion

Platelet adhesion plays an important role in normal platelet haemostasis whereby platelets will adhere at sites of vascular damage, disruption, endothelial dysfunction, and exposed sub-endothelial collagen or lipid deposits. These areas can be found in ruptured or eroded atherosclerotic plaques [11, 12]. Specific platelet membrane glycoproteins are recognised by the adhesive protein Collagen and allow the platelets to adhere when Collagen becomes exposed within the vessel wall and interacts with the platelet receptor GP VI (Figure 1.1).

Aggregation

Glycoproteins are also critical for cell–cell interactions as a change in the membrane receptor GPIIb/IIIa allows fibrinogen to form multiple cross-links between GPIIb/IIIa on adjacent platelets (Figure 1.1) [13]. The formation of a haemostatic plug at sites of vascular damage is started by the recruitment of circulating platelets and continues until the plug is fully formed. A lattice of fine fibrin acts to reinforce the plug against the pressure of the blood and starts to stem blood loss. Pathologic thrombosis occurs

when this process is affected by disease, leading to life threatening events such as acute myocardial infarction and deep venous thrombosis.

1.1.2 Anti-Platelet Therapies

The surface of a platelet is covered in a variety of receptors which bind to specific molecules during the different stages of haemostasis. Anti-platelet drugs can block these receptors, thus reducing thrombus formation. Clopidogrel (Plavix) is an anti-platelet drug that blocks the P2Y₁₂ receptor and is used for the prevention of thrombosis after placement of an intracoronary stent [11]. By testing platelet adhesion or aggregation a measurement of platelet function can be determined and thereby a measure of the efficacy of the anti-platelet therapy. With a number of studies showing the response to an anti-platelet drug may vary from patient to patient [6], there is a need for a reliable, reproducible and cost effective test to measure an individual's response to these drugs.

1.2 Platelet Function Analysis

Many of the well-established platelet function tests were designed for the diagnosis and treatment of bleeding disorders. The most common assays to evaluate anti-platelet drug effects, including flow cytometry and the gold standard, light-transmission platelet aggregometry, are mainly restricted to specialised facilities and require the sample to be processed before use [14]. While a small number of automated devices that work with whole blood are available, they are mainly restricted for laboratory use only and are not routinely used as a point-of-care test (POCT) [15]. A POCT can be defined as medical testing at or near the site of patient care.

Bleeding Time

First used by Duke in 1910, bleeding time is the time it takes for a standardised skin cut of fixed depth and length to clot [16, 17]. Bleeding time is not a useful predictor of the risk of haemorrhage (uncontrolled bleeding). Patients who may have recently taken aspirin or anti-inflammatory agents cannot be reliably identified using bleeding time. By the 1990s bleeding time had been replaced by light transmission aggregometry as the gold standard for the diagnosis of platelet disorders [18].

Light Transmission Aggregometry

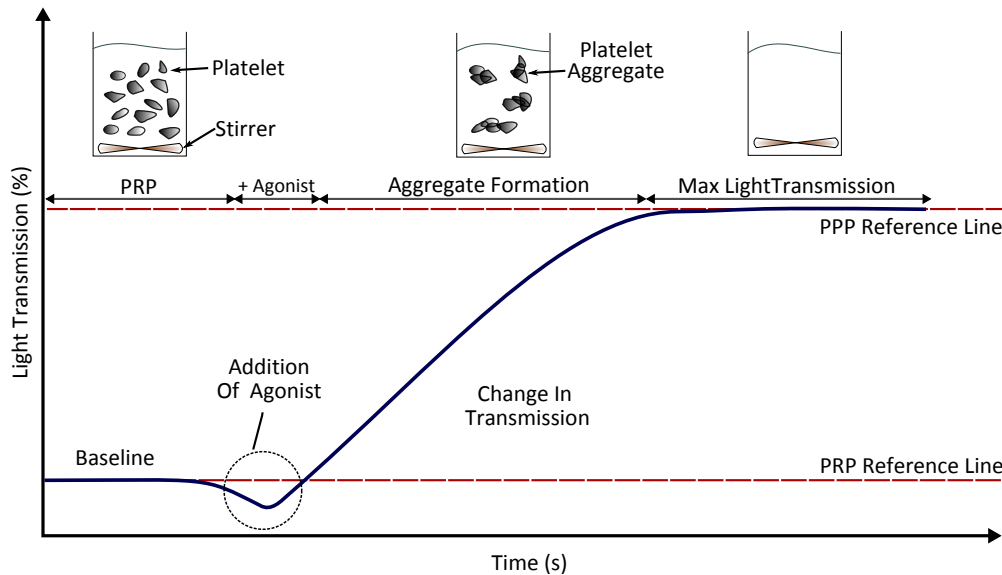


Figure 1.2: Light Transmission Aggregometry

Light transmission aggregometry (LTA) is a laboratory based technique invented in the 1960s and is currently the gold standard for the measurement of platelet function [11]. LTA requires a whole blood sample to be processed to create platelet rich plasma (PRP) and platelet poor plasma (PPP). Whole blood is centrifuged at 170-200 g for 10 minutes to create the PRP, while PPP is prepared by centrifugation (after removal of PRP) at a minimum of

1500 g for 15 minutes [19]. Platelet aggregation is calculated by passing a beam of light through the PRP. The amount of light to pass through the sample is detected with the use of a silicon photodiode, with the change in the percentage of light transmitted through the sample corresponding to the rate at which the plasma is aggregating or disaggregating. Figure 1.2 shows a standard aggregation curve with both the PPP and PRP reference levels shown, with the slope of the curve between these two points indicating the rate of platelet aggregate formation. The PPP reference level indicates the maximum light that can pass through the PRP after an agonist has been added. The PRP is stirred continually whilst testing is taking place, as the absence of stirring will lead to a significant reduction in aggregation. When an agonist is added there is an initial drop in the transmission of light below the PRP reference before the agonist is absorbed into solution and aggregation begins. Figure 1.2 shows an ideal curve and assumes 100% aggregation after a given time, in reality the aggregation will plateau at a maximum value for the sample being tested.

LTA has a number of limitations as a technique for use within a point-of-care device as it requires a specialised laboratory with specialised personnel, is time-consuming, expensive and needs the blood to be processed. The preparation of both PRP and PPP requires a minimum of 25 minutes and the use of a centrifuge before the plasma is manually separated from the whole blood sample. The results from a single sample can depend on the device used and the laboratory at which they were processed. The high level of manual handling of blood, training required and equipment costs also make the test impractical as a point-of-care device.

PFA-100[©]

Platelets mainly bind to subendothelial collagen exposed upon vascular injury and can bind directly to the exposed collagen through two major receptors; the integrin $\alpha2\beta1$ and glycoprotein *GPVI*. This binding takes place at shear rates $> 1500 \text{ s}^{-1}$. Two examples of platelet function assays at work at high shear rates are the Analyzer-100 (PFA-100[©]) and the Impact-R[©] cone and plate(let) [11, 15].

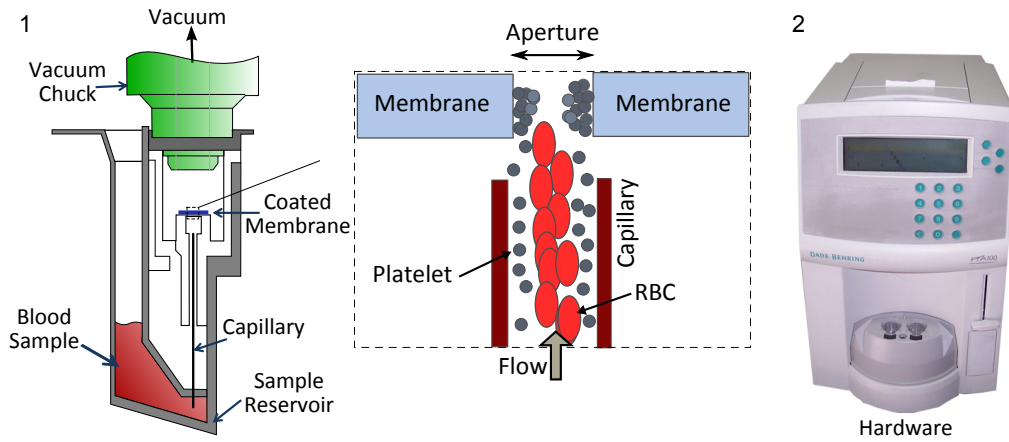


Figure 1.3: PFA-100[©]

PFA-100[©] uses a single use membrane that can be coated with collagen and epinephrine (CEPI) or collagen and ADP (CADP). Figure 1.3 shows a cross-section of the PFA cartridge alongside a photo of the device. The enlarged area shows the whole blood sample been drawn from the reservoir and aspirated into a capillary and through a $147 \mu\text{m}$ aperture cut into the membrane. A negative pressure is then applied to the sample to achieve flow at a shear rate of between 5000 and 6000 s^{-1} , as a haemostatic plug is formed across this aperture [14]. The amount of time required for the occlusion of the aperture by the haemostatic plug is regarded as the measurement of platelet function in this assay. Von Willebrand disease (VWD), primary secretion defects (PSD), Hermansky-Pudlak syndrome, (HPS) and storage

pool disease (SPD) are not related to platelet function, but may affect the time for the haemostatic plug to occlude the aperture [20]. PFA-100 has a limited use when trying to detect the specifics of platelet function as these disorders are not related to platelet function but can affect the "time-to-plug". The device is also limited to testing only one agonist at a time and requires the blood to be pipetted into the sample reservoir of a cartridge. The PFA-100 is therefore a single agonist test that requires manual blood handling, making it better suited for laboratory use only.

Cone and Plate(let) Analyser

The cone and plate(let) analyser was originally developed by Varon and monitors platelet adhesion and aggregation to a plate coated with collagen or extracellular matrix (ECM) under high shear conditions of 1800 s^{-1} . A commercial version was later developed by DiaMed [11].

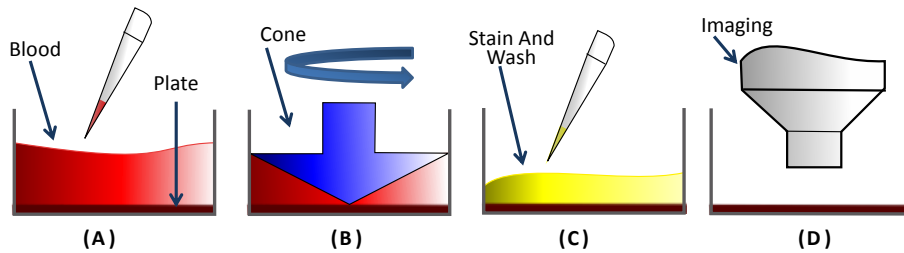


Figure 1.4: (A) Whole blood is first loaded into the well.(B) The cone is lowered into the well and rotated and the blood sheared. (C) The plate is then washed and the platelets stained. (D) The platelets can now be imaged.

Figure 1.4 shows the principle behind the cone and plate system. Whole blood is first loaded into the well covering a plate coated with extracellular matrix (ECM) before a cone is lowered into the well and rotated in order to shear the blood. After a fixed time the plate is removed, washed and the adhered platelets stained to allow for imaging. Although the Impact-R[©] (DiaMed) is a commercially available cone and plate(let) analyser, the system still requires the use of trained personnel and therefore remains a

tool for specialist use only [14]. Platelet adhesion in this assay is only read at one time point and as platelet adhesion is a dynamic process potentially useful clinical data could be lost by taking only one reading.

VerifyNow[®]

VerifyNow[®] is an automated cartridge-based system available for the testing of anti-platelet therapies in the clinic. The system tests a whole blood sample for its response to anti-platelet agents such as Clopidogrel GP IIb/IIIa inhibitors.

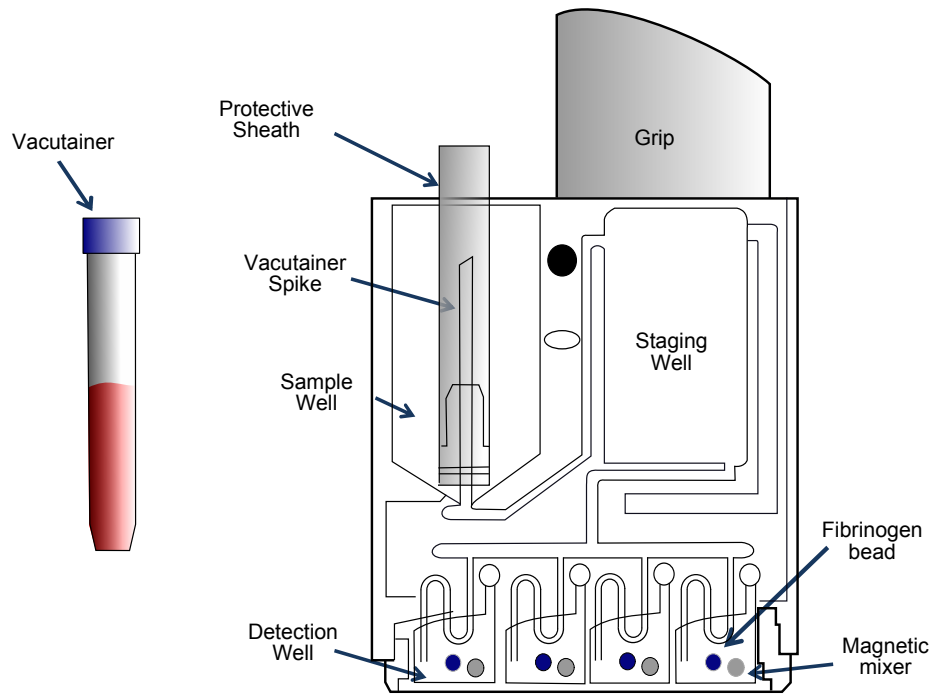


Figure 1.5: VerifyNow[®] cartridge

The VerifyNow system is based around a single-use cartridge shown in Figure 1.5 and works with the BD Vacutainer (Becton, Dickinson and Company) also shown in Figure 1.5. The Vacutainer is a sterile glass or plastic tube with a vacuum inside, the vacuum facilitates the draw of a blood sample. Figure 1.6 shows the operation of the cartridge once it had

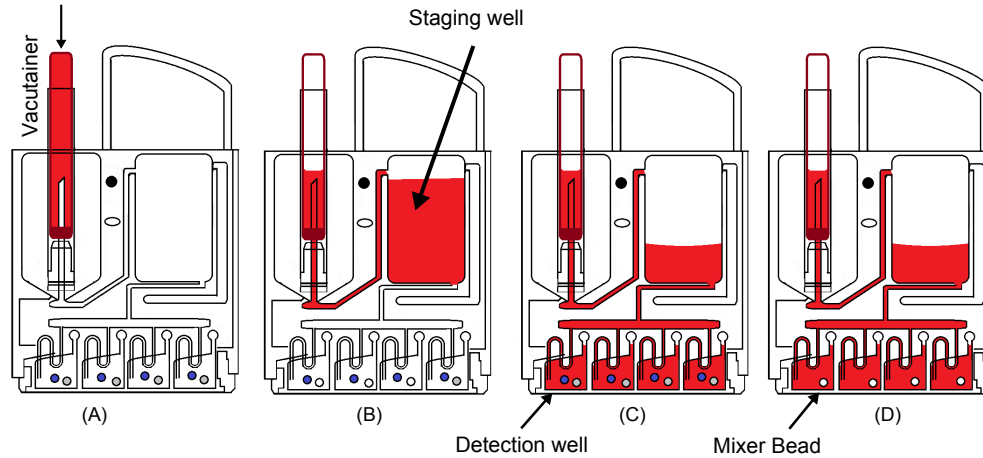


Figure 1.6: (A) vacutainer is connected. (B) A vacuum pumps the blood into the staging well. (C) Blood is moved from the staging well into the detection wells. (D) Blood is mixer bead to help the aggregation of platelets.

been connected to the VerifyNow system. A full Vacutainer is inserted into the cartridge through the use of the Vactainer spike. The VerifyNow device applies a vacuum to pump the blood into the staging well at the right of the cartridge. The blood is heated before the pressure is reversed and the blood is moved from the staging well into the detection wells. A fibrinogen bead within the detection wells dissolves into the blood before a magnetic mixing bead, contained in the wells, is moved in order to mix the blood and help the aggregation of platelets. After mixing is complete, light is passed through each of the detection wells and measurements are taken before the system can return an output value in platelet reaction units (PRU). The ability of the assay to use whole blood and the automated test platform give the system a number of advantages over LTA. However, the inflexibility of the cartridge allows only one therapy to be tested at a time with a separate Vacutainer (10 ml) of blood required for each test.

Two large scale studies have been undertaken using the VerifyNow sys-

tem [21, 22]. The Gauging Responsiveness with a VerifyNow P2Y12 assay: Impact on Thrombosis and Safety (GRAVITAS) and The Bedside Monitoring to Adjust Antiplatelet Therapy for Coronary Stenting (ARTIC). The GRAVITAS trial enrolled 5429 patients with coronary artery disease (predominantly, albeit not uniquely, with stable disease) [22]. The trial found that using VerifyNow to test platelet function did not affect the primary end point of cardiovascular death, myocardial infarction or stent thrombosis and the determination of a suitable clinically relevant cut-off level using the VerifyNow was challenging. The ARTIC studies randomly assigned 2440 patients scheduled for coronary stenting to a strategy of platelet-function monitoring [21]. The study found no significant improvements in clinical outcomes when using the VerifyNow system for platelet-function monitoring [21].

1.2.1 Summary of Devices

A communication by the scientific and standardisation committee of the International Society on Thrombosis and Haemostasis [23], reported a series of points highlighting the issues with use and development of the current flow tests used to evaluate bleeding risk. These points include:

1. Use and quantity of controlled collagen as adhesive substrate
2. Time-dependent measurement of thrombus build-up
3. Use of non-anticoagulated blood, preferably at physiological cation concentrations
4. Use of single-pass, small capacity flow devices

While the list was specifically generated with a view towards VonWillebrands disease, many of the points are of a generic nature and can be applied

to many platelet function assays. Each device in this section was examined for their use as a point-of-care device for testing the effectiveness of anti-platelet therapies and compared against the above list. The review showed that while many of the devices have a number of advantages there are still many challenges to overcome. Although LTA remains the gold standard for the testing of platelet function, the requirement to centrifuge the blood in order to create PPP and PRP, and cost of ownership makes LTA unsuitable as a point-of care (POCT) device. With the possibility that more than just platelet function may affect the results from the PFA-100, the device is better suited to a laboratory where additional testing is available. The VerifyNow[®] system goes a long way towards meeting the needs of any possible POCT device. However, it is still mainly used as a laboratory tool due to its relatively high cost. Many patients are on dual anti-platelet therapy requiring more than one cartridge per patient, making this assay costly and may preclude the VerifyNow[®] being used as a part of routine screening. Furthermore, two large scale studies also report no significant improvements in clinical outcomes when using the VerifyNow[®] system. It is clear from this review that at present there is no suitable POCT currently available for the testing of platelet function, and continued research into this area is required if one is to be developed.

1.3 Individual Platelet Adhesion (iPA)

Individual Platelet Adhesion (iPA) allows for the adhesion of a single platelet onto a 6 μm fibrinogen dot. Whole blood is incubated at room temperature for 30 minutes and rocked at 35 oscillations per minute. While iPA has been successfully demonstrated for the monitoring of patients undergoing anti-platelet therapy it has not yet been integrated into a chip [24].

For this thesis the iPA assay was used, as a starting point, for the re-

search and development of two prototype devices that have both successfully integrated the iPA assay. The first device is based on degas-driven flow, detailed in Chapter 4. The second prototype takes advantage of the rocking-table to create flow across the fibrinogen dots, detailed in Chapter 5.

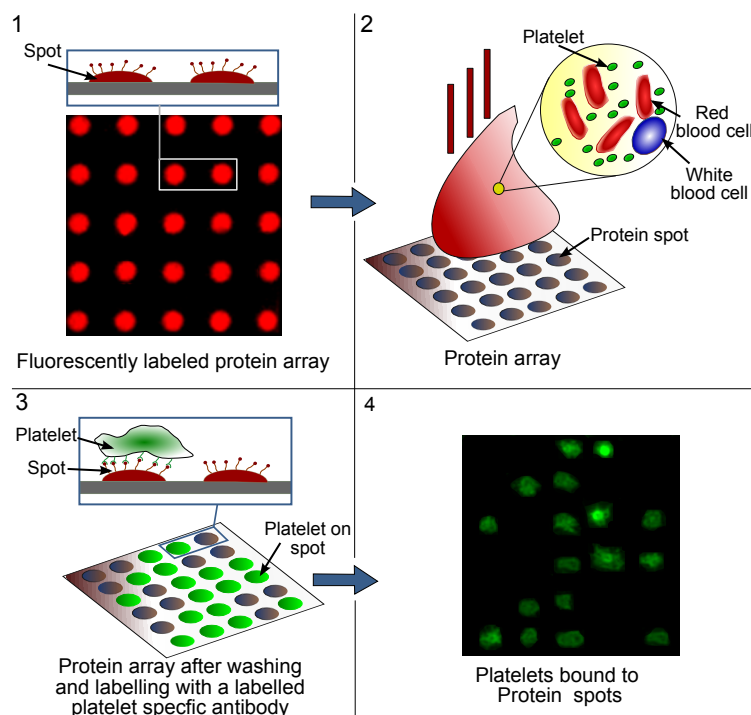


Figure 1.7: Whole blood is incubated on a substrate array of platelet-specific protein. Single platelets adhere to the protein spots, creating arrays of single platelets on the substrate and the percentage adhesion is quantified by use of fluorescence microscopy.

A novel method for the measurement of platelet function has recently been demonstrated by Basabe-Desmonts et. al. This method allows for separation of individual platelets from whole blood. As only a single platelet binds to a spot a digital quantification of platelet function is possible [25].

1 mL of citrated whole blood is placed covering the protein patterned surface and incubated for 30 minutes. The blood is rocked to prevent other blood cells from blocking the protein spots. Once incubated the slide is

washed and the platelets labelled (Figure 1.7) [25]. Using fluorescence microscopy the now labelled platelets can be counted and the percentage adhesion calculated. The use of this assay for the monitoring of patients on both dual and single anti-platelet therapies was demonstrated by Ana Lopez-Alonso *et. al.* [24].

1.3.1 Labelling Used Within iPA Assay

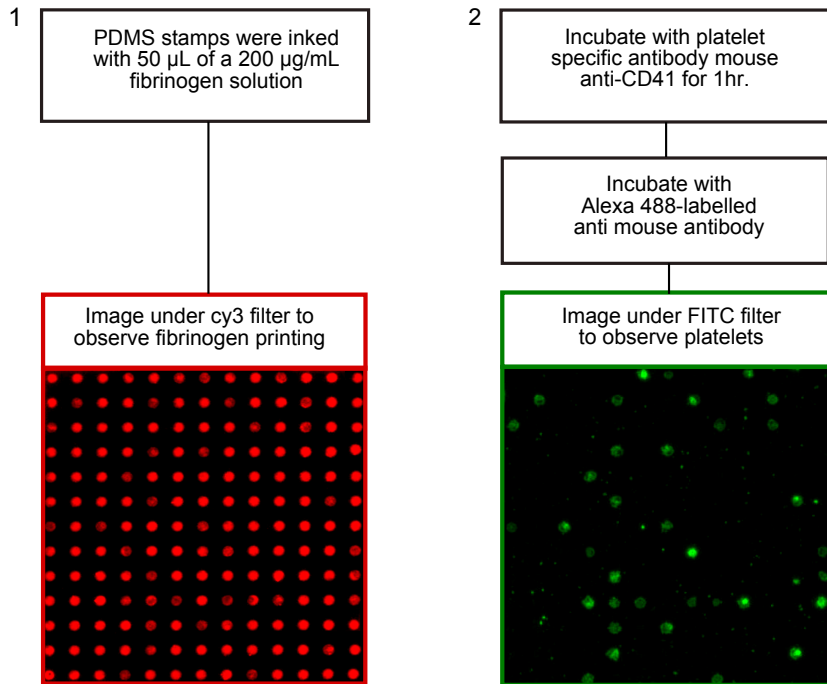


Figure 1.8: Use of labelling within the iPA assay. 1) cy3 label used to label the $6\ \mu\text{m}$ fibrinogen spots, arrayed in squares of 13×13 . 2) Image of platelets adhered to spots, labelled with Alexa-488 and visible under FITC filter.

Figure 1.8 shows the labelling techniques used as part of the iPA assay. Fibrinogen is mixed with Cy3 labelled bovine serum albumin (BSA, $25\ \mu\text{g}/\text{mL}$) before being applied to a PDMS stamp and μ -contact printed onto the selected substrate. Labelling of platelets bound to the fibrinogen spots takes place after the assay has been run and the substrate washed. This is achieved by first incubating with a platelet specific antibody (mouse

anti-CD41) for 1 hour before incubating with a secondary Alexa-488 labelled anti-mouse antibody for 30 minutes. The Alexa-488 dye has an excitation value of 495 *nm* and an emission value of 519 *nm*.

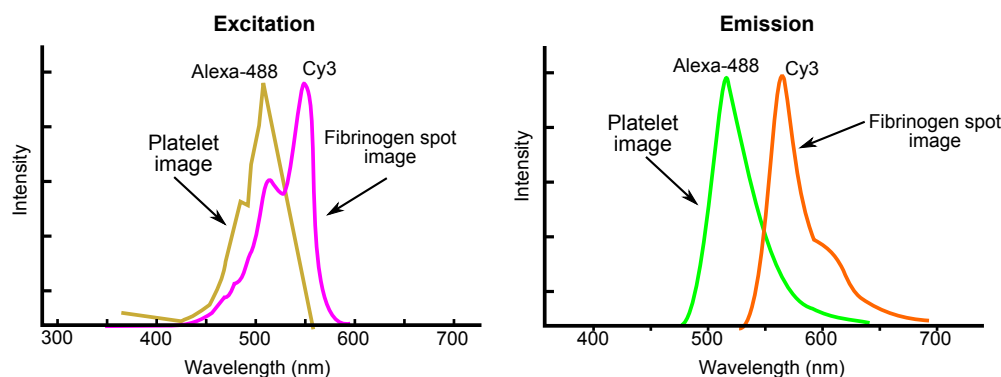


Figure 1.9: Excitation and emission wavelength values for fluorescent dyes uses as part of the iPA assay, Alexa-488 and Cy3 are shown.

Figure 1.9 shows the excitation and emission for both Alexa-488 and Cy3. Alexa-488 dye (platelet image) has an excitation value of 495 *nm* and an emission value of 519 *nm* and Cy3 dye (fibrinogen spots image) has an excitation value of 550 *nm* and an emission value of 570 *nm*. The emission value for the fibrinogen spots is far enough away from that of the platelets to allow for two separate images to be produced, with the use of a suitable filter. The protein array is shown in red (Figure 1.8) while the platelet image is shown in green; by matching each platelet to a protein spot the % of occupied spots can be calculated.

1.4 Microfluidic Channels And MEMS Development

A microfluidic channel can be defined as having one or more of its dimensions less than 1 *mm*, and the volume of the channel can be as little as a few nanoliters [26]. This allows for a small sample size, reducing the amount

of reagents used when compared to traditional devices. These reductions often lower the final device cost, particularly when expensive reagents are used [27, 28]. Fluids used within these devices include, bacterial cell suspensions, protein and antibody solutions. Whole blood can also be used within these devices with properties such as temperature, red blood cell count, and clotting factors effecting how a blood sample can flow through a microfluidic channel. The flow characteristics of blood must therefore be considered when designing the channels used within this project.

$$Re = \frac{\text{inertial forces}}{\text{viscous forces}} = \frac{\rho V_{avg} L}{\mu} \quad (1.1)$$

The Reynolds number, Re , is a dimensionless number (Equation 1.1), given the ratio of inertial forces to viscous forces and plays an important role in the design of microfluidic devices. The Re is also used to characterise the type of flow within a channel as laminar for values less than 1500 and turbulent for values over 2500, while for Re values between 1500 and 2500 the flow is considered to be transitioning between fully laminar and fully turbulent [29]. For microfluidic channels the Re is generally less than 100, allowing for flow in a microfluidic channel to be considered as laminar.

It is generally assumed that the no-slip boundary condition can be applied once the flow is laminar and pressure driven. However, this assumption may not be valid within a microfluidic channel with complex behaviour at a liquid/solid interface where wetting, shear rate, pressure, surface charge, surface roughness, impurities and dissolved gas may challenge this assumption [30]. This boundary condition allows for a simplification of the equations, by assuming the fluid velocity at the walls is zero. The importance of these assumptions are further developed in Chapter 2.

MEMS

Microelectromechanical systems (MEMS) are defined as having both miniaturised mechanical and electromechanical elements that can be fabricated using micro-fabrication techniques such as photo lithography, chemical vapour deposition, plasma enhanced chemical vapour deposition and sputtering [31]. Mechanical machining and laser ablation can also be used to fabricate MEMS. Mechanical machining of MEMS can be used when fabricating prototype devices or a small number of commercial devices, with the cost of equipment and the time required to machine each device making it impractical for large scale production. While micro-machining methods such as photo lithography allows for large volumes of devices to be fabricated the cost of setup can make it unsuitable for small volumes. MEMS have been developed since the 1970s for use in devices such as pressure sensors, temperature sensors, accelerometers, altimeter and gas chromatography. The mobile phone is an example of the advances in MEMS enabled devices from its microwave transmitter to the touch-screen used on smartphones, indicating how MEMS devices play an ever-increasing role in daily life [32]. The dimensions of a MEMS device can vary from well below one micron to as big as several millimetres. The types of MEMS devices can vary from relatively simple structures having no moving elements to devices with a high level of complexity and millions of moving parts such as complementary metal-oxide-semiconductor (CMOS) used in computer memory [33]. MEMS devices that integrate microfluidic channels are also available and are widely used within both the laboratory and the clinical environments. As the Reynolds number within a microfluidic channel is very low and the flow is almost always laminar mixing of the sample can be difficult, as mixing is only through diffusion across the streamlines. The design of any microfluidic device will need to allow time for mixing, if the assay requires

the blood to be mixed with a reagent before testing.

MEMS microfluidic devices have the potential to be of use as a point-of-care device when they offer an advantage over traditional flow based devices, where per-unit cost, automation or the cost of reagents play a key role [28]. Devices designed to miniaturise analytical or bioanalytical techniques by integrating them into a micro-fabricated format are generally included under the umbrella term Lab-on-a-Chip (LoaC)

BioMEMS

Bio-Microelectromechanical (BioMEMS), with a focus specifically on biological applications can be considered to be LoaC devices. LoaC devices are typically advantageous because they have:

- low fluid volumes required, because of the low internal chip volumes.
- safer platform for biological, chemical or radioactive samples (only a small sample volume is required).
- higher analysis and control speed of the chip.
- better efficiency due to short mixing times (short diffusion distances).
- faster heating as a result of short distances, high wall surface-to-fluid volume ratios and small heat capacities.
- compactness of the systems due to large integration of functionality and small volumes.
- lower fabrication costs, allowing for mass-produced and cost-effective disposable chips.

BioMEMS is a rapidly growing area of MEMS and uses some of the same micro-fabrication technologies as MEMS. BioMEMS allows for the

integration of microfluidic channels and sensor(s) onto a single chip that can be fabricated reproducibly using current available technologies [34]. Implantable devices such as retinal implants, systems to deliver drugs and devices for the stimulation and recording of the central nervous system are amongst only a few possible applications being developed using BioMEMS [35]. Point-of-care devices could also benefit from the on-going development of BioMEMS.

1.4.1 BioMEMS for Cell Based Analysis

Many BioMEMS devices aim to reduce the cost and sample size of current and future cell-based assays. Relatively inexpensive MEMS technology is ideal for use in the next generation of cell culture and cell analysis tools where large numbers of single cells or small cell populations can be investigated in a cellular microenvironment of increased physiological relevance, when compared to current methods [36]. There are currently a significant number of MEMS-based flow devices available across a number of different applications [37, 37–39]. A common flow chamber design used in cell-based MEMS is known as a parallel plate flow chamber.

Parallel Plate

Parallel plate flow chambers are the design of choice for many applications where the shear effects on biological species play an important role. A significant body of work has already been carried out on the effect flow conditions can have on assays, where shear rate is an integral part of the assay design [40–42]. A body of work has also been developed, investigating the implications of adjusting variables such as aspect ratio, entrance length and inlet design on overall performance of a parallel plate flow device [43–45]. The combination of these research areas allow for the design of parallel-

plate flow chambers where the fluid behaviour can be readily understood and modelled. The low aspect ratio of parallel plate flow chambers is a key consideration in their design, where the width of the channel (b) is far in excess of the height (a) allowing for a significant simplification of the governing equations and making any calculations for shear relatively simple. This is further explained in Chapter 2.

1.5 Fabrication

For a Lab-on-a-Chip device to be practical, its fabrication must be both rapid and reproducible. MEMS devices were predominantly silicon-based [46], allowing both rapid and reproducible fabrication. However silicon's lack of optical transparency makes it unsuitable for MEMS devices where imaging of a surface is required. The ability to fabricate MEMS using an optically transparent medium is particularly important in the area of BioMEMS, where the facility to make use of optical detection strategies and microscopy measurements make a transparent medium of significant advantage. Once modified, many of the existing semiconductor techniques could be applied to a glass substrate, allowing optically transparent BioMEMS to be fabricated. Glass is well suited as an optically transparent substrate, as it is both chemically and biologically compatible. These devices are often a single-use item and have proved relatively expensive for mass fabrication. There is a need for methods to manufacture multiple devices reproducibly, with a short lead time and at a low cost. Polymers offer an alternative to glass and have become popular for use as material for BioMEMS or Lab-on-a-Chip devices [47, 48]. Polymers are available in a wide range of low-cost biochemically compatible materials, each with different characteristics that are relatively easy to process and prototype, giving polymers a number of advantages over silicon or glass. The manufacturing of polymer-based

devices can be divided into two distinct subgroups, direct or replication techniques.

Direct and Replication Techniques

Direct-machining typically involves the removal of material in order to produce the desired pattern; in the case of MEMS devices this pattern is defined by the network of fluidic channels of a controlled depth and width. Typical polymer direct-machining techniques involve micro milling [49] or laser writing [50] and allow for flexible and offer short lead times making them particularly suited to prototyping of MEMS devices. Replication techniques typically involve the fabrication of a relatively expensive master which will be used to produce all subsequent devices. The master typically needs to be of a high quality and finish. The manufacture of the master may include using traditional machining techniques such as milling or turning, photolithographic techniques may also be considered. Common methods of replication include embossing [49, 51, 52], injection moulding [53, 54], or die cutting techniques. Once in use, the masters may also wear out and need to be replaced. Although there is an initial investment, in both time and increased cost, needed to manufacture a master the cycle time (per device) is typically significantly shorter than direct machining. This can make replication better suited to production of a large number of devices or where the cost or lead time of direct machining techniques proves prohibitive.

Photolithography

One of the most widely used fabrication techniques for the manufacture of microfluidic channels is photolithography. The process starts with an opaque plate (photomask) on which a transparent pattern has been made so that light can only pass through the pattern; these geometric patterns

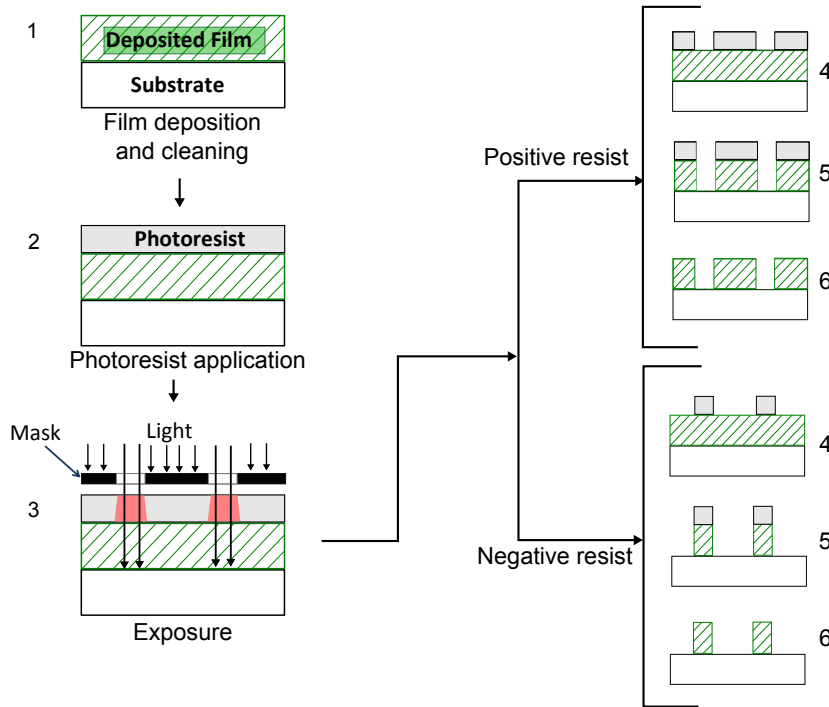


Figure 1.10: Steps required to fabricate microfluidic channels using photolithography. (1) The wafer is cleaned and readied for use in photolithography. (2) A photoresist is then deposited onto a substrate. (3) The mask is applied along with a light source, to transfer the pattern onto the wafer. (4) Development. (5) Etching. (6) Resist removal.

layout the path of the channels to be created. A wafer, normally silicon, is prepared by first cleaning away any organic or inorganic contaminants, before a light-sensitive chemical (photoresist) is spin-coated onto the surface. Ultraviolet excimer lasers are widely used as a light source in photolithography and operate at 248 nm (krypton fluoride laser) and t 193 nm (argon fluoride laser). The light is passed through the photomask transferring the channel design onto a photoresist before a chemical treatment is then used to engrave the exposed pattern into a base material beneath (Figure 1.10). Photoresists are classified into two groups, positive resists and negative resists. When positive resists are exposed to light they dissolve quickly in the developers while the unexposed regions of negative resists are easily removed. Once developed the photoresist is washed off, leaving the pattern

engraved into the base material allowing for complex channel designs, enabling multiple tests to run simultaneously across a number of channels on a single chip. Microfluidic and electronic components can also be integrated onto a single chip, at a low cost, allowing for the development of disposable chips with integrated sensors. These chips could be used to preform chemical reactions, and calibration-free analytical measurements with small quantities of complex samples such as whole blood [28].

Lamination Technologies

Lamination technologies are well suited to planar flow devices, allowing for rapid development of 3D fluidics at a low cost.

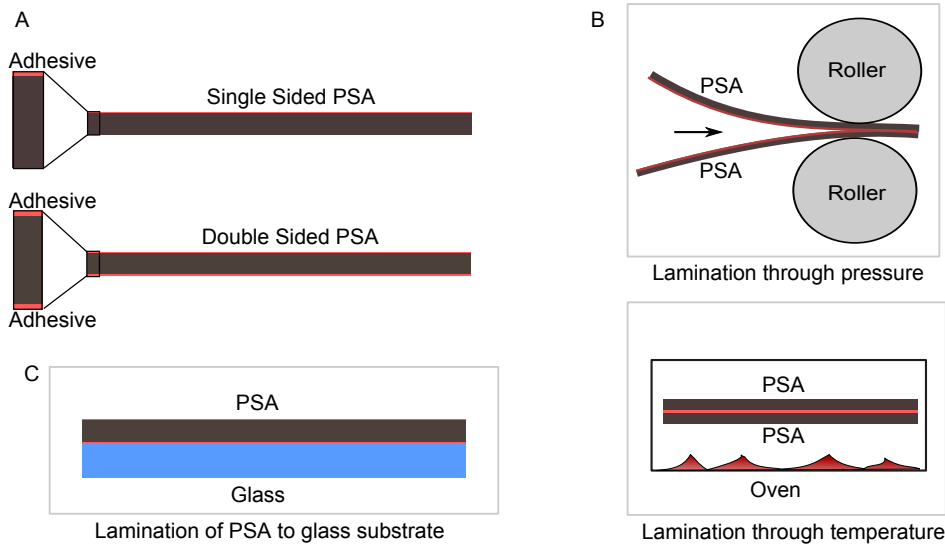


Figure 1.11: Lamination technologies. A) Types of PSA. B) Lamination through pressure and temperature. C) glass substrate laminated with PSA.

Figure 1.11 shows a cross-section of a thin polymer commonly used within lamination technologies. When an adhesive material is applied on one or both sides of the polymer a product known as pressure sensitive adhesive (PSA) is created. Figure 1.11-B shows how PSA can be activated through either pressure or in some cases temperature; in the figure, two

pieces of PSA are being laminated together. Glass (with its biocompatibility and optical properties) can be used as a substrate for hybrid chips. When combined with a channel cut into PSA and laminated a flow device can be easily manufactured.

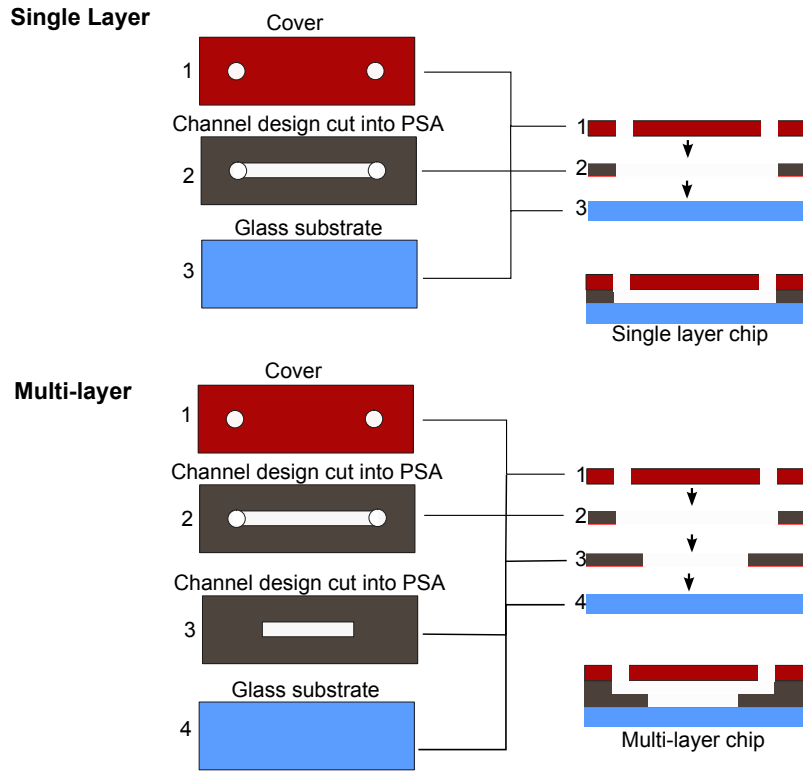


Figure 1.12: Technique to allow both single and multi-layer μ scale structures.

Figure 1.12 shows a single layer flow device with a simple channel and an inlet and outlet. The cover and glass substrate are laminated between the layer of double sided PSA containing the channel. To create a 3D structure this pressure sensitive adhesive (PSA) is stacked in layers of a single thickness or can be combined into layers of different thicknesses. The technique allows for both single and multi-layer μ -scale structures to be cut, manufactured and assembled at a low cost. These structures can range from complex multi-channel designs, which integrate many different flow characteristics, to straight channels with a single inlet and outlet used in

parallel plate flow. PSA can also be cut to create 3D moulds, with the raised area of PSA allowing the channel geometry to be transferred to the casting material.

Polydimethylsiloxane in Microfluidic Devices

Poly (dimethylsiloxane) (PDMS) is an excellent material for the fabrication and rapid prototyping of microfluidic devices which incorporate biological samples. PDMS is nontoxic, has a low curing temperature and allows a reversible seal to be formed between the material and substrate [55, 56]. This elastomeric polymer has been used across a range of different applications from standard planar fluidic devices [57], complex devices integrating microfluidics valves [58] and a number of different pumping techniques described by Grover *et al.* and Dallas *et al.* [59, 60]. 3D devices can also be created by laminating thin layers of PDMS atop one another, while a UV/Ozone cleaning system is used to bind each layer [61]. This type of 3D microfluidic device was demonstrated by van Midwoud *et al.* for the in-vitro assessment of interorgan drug metabolism using both intestinal and liver slices [62]. When PDMS is placed under a vacuum any gas within the bulk is evacuated. Once returned to atmosphere gas is slowly reabsorbed into the PDMS. This ability allows self-powered integrated devices containing a dead end channel to be created. This technique has been demonstrated with both an on-chip sequential injection immunoassay [63] and within a chip designed for the analysis of blood samples [64]. These devices do not require any external connections, tethers, or tubing commonly used with pumping systems such as a syringe pump. Along with device manufacture, PDMS can be used in other areas of MEMS development, such as protein patterning. PDMS is also the preferred material used to create the stamps needed for microcontact printing (μ CP). This method was developed by Kumar

and Whitesides for the patterned transfer of thiols onto gold surfaces [65]. Basabe-Desmonts and Lopez-Alonso *et al.* used spots patterned using μ CP for the measurement of platelet function in whole blood [24, 25]. PDMS is ideally suited for use with BioMEMS devices, with the ability to mould μ channels from silicon masters to the development of power-free pumps. The combination of silicon masters and PDMS has opened up the area of μ CP, allowing complex designs or simple arrays of spots to be patterned reproducibly and at a low cost. While PDMS may not be ideal for large-scale manufacture of MEMS devices, it is well suited for rapid prototype development and continues to be used in BioMEMS design.

1.6 Thesis Aims and Objectives

The aim of the project is to develop a device that would allow a clinician to test a patient's responsiveness to anti-platelet therapies and as a diagnostic tool for individuals at risk of suffering a cardiovascular event. Using current technologies in the field of microfluidics a prototype device has been designed to address the challenge of integrating the use of whole blood, mixing of reagents, delivery of blood, imaging system and the analysis of the sample. The prototype lab-on-a-chip device should be demonstrated to show a detectable difference in an individual's response in both the presence and absence of an anti-platelet therapy such as Cangrelor.

Key Objectives

1. To investigate and characterise how channel geometry affects blood within a biological assay used to detect the effects of anti-platelet therapies on an individual.
2. To identify and develop new technologies that can be used to design and build a single-use prototype point-of-care device to test anti-platelet therapies.
3. To develop new image processing techniques that will allow for the automated quality control of a printed protein surface.
4. To develop a technique to automate acquisition of results from complex protein arrays used with the prototype device.

Bibliography

- [1] World Health Organization. Causes of death 2008: data sources and methods. *World Health Organization, Geneva*, 2010(September 2010):1–28, 2010.
- [2] Peter Scarborough Melanie Nichols, Nick Townsend and Mike Rayner. European cardiovascular disease statistics. *European Heart Network*, 3:11–35, 2012.
- [3] K. Jamrozik, R. Taylor, and A. Dobson. *International Encyclopedia of Public Health*. Elsevier, 2008.
- [4] Carl Whatling Timothy D. Warner, Sven Nylander. Anti-platelet therapy: cyclo-oxygenase inhibition and the use of aspirin with particular regard to dual anti-platelet therapy. *British Journal of Clinical Pharmacology*, 72(4):619–634, 2011.
- [5] Jan Pospisil, Milan Hromadka, Ivo Bernat, and Richard Rokyta. Review Article Special issue : Thrombosis STEMI The importance of balance between antithrombotic treatment and bleeding risk. *Cor et Vasa*, 55(2):e135–e146, 2013.
- [6] M Cattaneo. Response variability to clopidogrel: is tailored treatment, based on laboratory testing, the right solution? *Journal of thrombosis and haemostasis : JTH*, 10(3):327–36, March 2012.

- [7] MJ Santos-Martínez and Adriele Prina-Mello. Analysis of platelet function: role of microfluidics and nanodevices. *Analyst*, 136(24):5120–6, December 2011.
- [8] Alan D Michelson, Verifynow Accumetrics, San Diego, and Plateletworks Helena Laboratories. Methods for the Measurement of Platelet Function. *The American Journal of Cardiology*, 103(3):20A–26A, 2009.
- [9] Rajbabu Pakala and Ron Waksman. Currently available methods for platelet function analysis: advantages and disadvantages. *Cardiovascular revascularization medicine : including molecular interventions*, 12(5):312–22, 2011.
- [10] D M Wootton and D N Ku. Fluid mechanics of vascular systems, diseases, and thrombosis. *Annual Review of Biomedical Engineering*, 1(1):299–329, 1999.
- [11] Deepak L. Bhatt. *Platelets in Cardiovascular Disease*. Imperial College Press, 2008.
- [12] B. B. Vargaftig & J. Benveniste M. Chignard, J. P. Le Couedic, M. Tence. The role of platelet-activating factor in platelet aggregation. *Nature*, 279:799–800, 1979.
- [13] S. Moncada. Arachidonic Acid Metabolites and the Interactions between Platelets and Blood-Vessel Walls. *The New England journal of medicine*, 300(20):1142, 1979.
- [14] Paul Harrison. Platelet function analysis. *Blood Reviews*, 19(2):111–123, March 2005.
- [15] Alan D Michelson, Andrew L Frelinger III, and Mark I Furman. Current Options in Platelet Function Testing. *The American Journal of Cardiology*, 98(10, Supplement 1):S4–S10, 2006.

- [16] W. Duke. The relation of blood platelets to hemorrhagic disease. *The Journal of the American Medical Association*, 55(14):1185, 1910.
- [17] I. M. Nilsson S. Magnusson C. Borchgrevink. The duke and ivy methods for determination of the bleeding time. *Thrombosis Diathesis Haemorrhagica*, 10:223–234, 1963.
- [18] A. D. Michelson and Alan D. Michelson. *Platelets*. CA Academic, San Diego, 2011.
- [19] M. Christie,D.J., Avari,T., Carrington,LR., Cohen,E., DeBiase,B., Harrison,P., Kickler,T., Kottke-Marchant,K., Ledford-Kraemer,M.R., Rand,M.L., Schmaier,A.H., & McCabe White. Platelet function testing by aggregometry: approved guideline. *Clinical and Laboratory Standards Institute*, 28(31), 2008.
- [20] Paul Harrison. The role of PFA-100 testing in the investigation and management of haemostatic defects in children and adults. *British Journal of Haematology*, 130(1):3–10, July 2005.
- [21] Christophe Pouillot, Patrick Henry, D Ph, Pascal Motreff, Eric Van Belle, Hélène Rousseau, Pierre Aubry, Jacques Monségu, Pierre Sabouret, Stephen A O Connor, B Ch, Jérémie Abtan, Mathieu Kerneis, Christophe Saint-etienne, Olivier Barthélémy, Farzin Beygui, Johanne Silvain, Jean-Philippe Collet, Thomas Cuisset, Eric Vicaut, and Gilles Montalescot. Bedside monitoring to adjust antiplatelet therapy for coronary stenting. *The New England Journal of Medicine*, 367(22):2100–9, November 2012.
- [22] Matthew J Price, Dominick J Angiolillo, Christopher P Cannon, and Eric J Topol. Platelet reactivity and cardiovascular outcomes after percutaneous coronary intervention: a time-dependent analysis of the

- Gauging Responsiveness with a VerifyNow P2Y12 assay: Impact on Thrombosis and Safety (GRAVITAS) trial. *Circulation*, 124(10):1132–7, September 2011.
- [23] J J Zwagina, K S Sakariassen, M R King, T G Diacovo, E F Grabowski, G Nash, M Hoylaerts, and J W M Heemskerk. Can blood flow assays help to identify clinically relevant differences in von Willebrand factor functionality in von Willebrand disease types 1-3? 1. *Journal of Thrombosis and Haemostasis*, 5(12):2547–2549, 2007.
- [24] Dermot Kenny Ana Lopez-Alonso, Bincy Jose, Martin Sommers, Karl Egan, David P. Foley, Antonio J. Ricco, Sofia Ramstrom, Lourdes Basabe-Desmonts. Individual Platelet Adhesion (iPA) Assay: Measuring Platelet Function and Anti-Platelet Therapies in Whole Blood via Digital Quantification of Cell Adhesion. *Analytical Chemistry*, 85(13):6497–6504, 2013.
- [25] L Basabe-Desmonts, S Ramstrom, a J Ricco, and D Kenny. Single-step separation of platelets from whole blood coupled with digital quantification by interfacial platelet cytometry (iPC). *Langmuir : the ACS journal of surfaces and colloids*, 26(18):14700–6, September 2010.
- [26] Guo AJ van Rossmalen Zhang. *More than Moore: Creating High Value Micro/Nanoelectronics Systems (Google eBook)*. Springer, 2010.
- [27] A E Kamholz, E A Schilling, and P Yager. Optical measurement of transverse molecular diffusion in a microchannel. *Biophysical Journal*, 80(4):1967–72, April 2001.
- [28] B H Weigl, P Yager, and P.; Weigl, B.H.;Yager. Microfluidic diffusion-based separation and detection. *Science*, 283(5400):346, 1999.

- [29] M.; Çengel, Y.A.;Cimbala, J.M.;Kanoglu. *Fluid mechanics: Fundamentals and applications*. McGraw-HillHigher Education, 2006.
- [30] Eric Lauga, MP Brenner, and HA Stone. Microfluidics: The No-Slip Boundary Condition. In *Handbook of Experimental Fluid Dynamics*, chapter 15. Springer, New-York, 2005.
- [31] G M Rebeiz. *RF MEMS*. Wiley Online Library, 2003.
- [32] Tai-Ran Hsu. *MEMS & Microsystems: Design, Manufacture, and Nanoscale Engineering*. John Wiley & Sons, 2008.
- [33] J B Waldner. *Nanocomputers and Swarm Intelligence*, volume 189. ISTE, 2008.
- [34] Robert Langer Amy C. Richards Grayson, Rebecca S. Shawgo, Audrey M. Johnson, Nolan T. Flynn, Yawen Li, Michael J. Cima. A BioMEMS review: MEMS technology for physiologically integrated devices. *Proceedings of the IEEE*, 92(1):6–21, January 2004.
- [35] A.C.R. Grayson, R.S. Shawgo, A.M. Johnson, N.T. Flynn, Y. Li, M.J. Cima, and R. Langer. A BioMEMS Review: MEMS Technology for Physiologically Integrated Devices. *Proceedings of the IEEE*, 92(1):6–21, January 2004.
- [36] D A Beebe. Folch, The Science and Applications of Cell Biology in Microsystems,. *Lab Chip*, 5:10–11, 2005.
- [37] Dario Bogojevic, M Dean Chamberlain, Irena Barbulovic-Nad, and Aaron R Wheeler. A digital microfluidic method for multiplexed cell-based apoptosis assays. *Lab Chip*, 12(3):627–34, February 2012.
- [38] Edmond W K Young, Erwin Berthier, David J Guckenberger, Eric Sackmann, Casey Lamers, Ivar Meyvantsson, Anna Huttenlocher, and

- David J Beebe. Rapid prototyping of arrayed microfluidic systems in polystyrene for cell-based assays. *Analytical chemistry*, 83(4):1408–17, February 2011.
- [39] Linas Mazutis, John Gilbert, W Lloyd Ung, David A Weitz, Andrew D Griffiths, and John A Heyman. Single-cell analysis and sorting using droplet-based microfluidics. *Nature protocols*, 8(5):870–91, May 2013.
- [40] Peter Schall and Martin van Hecke. Shear Bands in Matter with Granularity. *Annual Review of Fluid Mechanics*, 42(1):67–88, January 2010.
- [41] S Dhinakaran, A M Afonso, M A Alves, and F T Pinho. Steady viscoelastic fluid flow between parallel plates under electro-osmotic forces: Phan-Thien-Tanner model. *Journal of colloid and interface science*, 344(2):513–20, April 2010.
- [42] H Lu, L Y Koo, W M Wang, D A Lauffenburger, L G Griffith, and K F Jensen. Microfluidic shear devices for quantitative analysis of cell adhesion. *Analytical Chemistry*, 76(18):5257–5264, September 2004.
- [43] Roger Van Kruchten, Judith M E M Cosemans, and Johan W M Heemskerk. Measurement of whole blood thrombus formation using parallel-plate flow chambers - a practical guide. *Platelets*, 23(3):229–42, January 2012.
- [44] D P Bakker, A van der Plaats, G J Verkerke, H J Busscher, and H C van der Mei. Comparison of Velocity Profiles for Different Flow Chamber Designs Used in Studies of Microbial Adhesion to Surfaces. *Applied and Environmental Microbiology*, 69(10):6280–6287, 2003.
- [45] I Papautsky, B K Gale, S Mohanty, T A Ameel, and A B Frazier. Effects of rectangular microchannel aspect ratio on laminar friction constant. *Proceedings of SPIE-The International Society for Optical*

- Engineering, Proceedings of the 1999 Microfluidic Devices and Systems II, Santa Clara*, 3877:147–158, 1999.
- [46] S A Wang W. Soper. *Bio-MEMS Technologies and Applications*. CRC Press, 2007.
- [47] H Becker and C Gartner. Polymer microfabrication methods for microfluidic analytical applications. *Electrophoresis*, 21(1):12–26, 2000.
- [48] Mauro Ferrari, editor. *BioMEMS and Biomedical Nanotechnology, Volume 4*. Springer, mauro ferr edition, 2006.
- [49] É Tyrrell, C Gibson, B D MacCraith, D Gray, P Byrne, N Kent, C Burke, and B Paull. Development of a micro-fluidic manifold for copper monitoring utilising chemiluminescence detection. *Lab Chip*, 4(4):384–390, 2004.
- [50] H Klank, J P Kutter, and O Geschke. CO 2-laser micromachining and back-end processing for rapid production of PMMA-based microfluidic systems. *Lab Chip*, 2(4):242–246, 2002.
- [51] Vasiliy N Goral, Yi-Cheng Hsieh, Odessa N Petzold, Ronald A Faris, and Po Ki Yuen. Hot embossing of plastic microfluidic devices using poly(dimethylsiloxane) molds. *Journal of Micromechanics and Microengineering*, 21(1):017002, January 2011.
- [52] Jesse Greener, Wei Li, Judy Ren, Dan Voicu, Viktoriya Pakhareno, Tian Tang, and Eugenia Kumacheva. Rapid, cost-efficient fabrication of microfluidic reactors in thermoplastic polymers by combining photolithography and hot embossing. *Lab Chip*, 10(4):522–4, February 2010.

- [53] R Blue, N Kent, L Polerecky, H McEvoy, D Gray, and B D MacCraith. Platform for enhanced detection efficiency in luminescence-based sensors. *Electronics Letters*, 41(12):682–684, 2005.
- [54] Usama M Attia and Jeffrey R Alcock. A review of micro-powder injection moulding as a microfabrication technique. *Journal of Micromechanics and Microengineering*, 21(4):043001, April 2011.
- [55] L.F. Wang, Q. Ji, T.E. Glass, T.C. Ward, J.E. McGrath, M. Mugli, G. Burns, and U. Sorathia. Synthesis and characterization of organosiloxane modified segmented polyether polyurethanes. *Polymer*, 41(13):5083–5093, June 2000.
- [56] Y Xia and G M Whitesides. Soft lithography. *Angew. Chem. Int. Ed.*, 37(5):550–575, 1998.
- [57] M L Chabinye, D T Chiu, J C McDonald, A D Stroock, J F Christian, A M Karger, and G M Whitesides. An integrated fluorescence detection system in poly (dimethylsiloxane) for microfluidic applications. *Analytical Chemistry*, 73:4491–4498, 2001.
- [58] M A Unger, H P Chou, T Thorsen, A Scherer, and S R Quake. Monolithic Microfabricated Valves and Pumps by Multilayer Soft Lithography. *Science*, 288(5463):113–116, 2000.
- [59] W H Grover, A M Skelley, C N Liu, E T Lagally, and R A Mathies. Monolithic membrane valves and diaphragm pumps for practical large-scale integration into glass microfluidic devices. *Sensors & Actuators: B. Chemical*, 89(3):315–323, 2003.
- [60] J M Berg, R Anderson, M Anaya, B Lahlouh, M Holtz, and T Dallas. A two-stage discrete peristaltic micropump. *Sensors & Actuators: A. Physical*, 104(1):6–10, 2003.

- [61] Paul M van Midwoud, Geny M M Groothuis, Marjolijn T Merema, and Elisabeth Verpoorte. Microfluidic biochip for the perfusion of precision-cut rat liver slices for metabolism and toxicology studies. *Biotech and Bioeng*, 105(1):184–94, January 2010.
- [62] Geny M.M. Groothuis Paul M. van Midwoud, Midwoud, Marjolijn T. Merema, MT, Elisabeth Verpoorte. A microfluidic approach for in vitro assessment of interorgan interactions in drug metabolism using intestinal and liver slices. *Lab Chip*, 10(20):2778–2786, 2010.
- [63] Kazuo Hosokawa, Kae Sato, Naoki Ichikawa, and Mizuo Maeda. Power-free poly(dimethylsiloxane) microfluidic devices for gold nanoparticle-based DNA analysis. *Lab Chip*, 4(3):181–5, June 2004.
- [64] Ivan K Dimov, Lourdes Basabe-Desmonts, Jose L Garcia-Cordero, Benjamin M Ross, Younggeun Park, Antonio J Ricco, and Luke P Lee. Stand-alone self-powered integrated microfluidic blood analysis system (SIMBAS). *Lab Chip*, 11(5):845–50, March 2011.
- [65] Amit Kumar and GM Whitesides. Features of gold having micrometer to centimeter dimensions can be formed through a combination of stamping with an elastomeric stamp and an alkanethiol "ink". *Appl Phys Lett*, 63(d):2002–2004, 1993.

Chapter 2

Theoretical Background

The study of fluid mechanics has allowed the definition of laws that govern how a fluid acts whether at rest (static), under flow (kinematics), and the effect of forces on fluid motion (dynamics). In common usage the word fluid is generally considered only to include liquids while within the area of fluid mechanics the word has a much broader definition that includes substances that continually deform (flow) under an applied shear stress including liquids, gases, plasmas and plastic solids. Substances that do not flow under stress are in turn classed as solid thus giving the technical difference between a fluid and a solid. Therefore, *A solid can resist shear stress by a static deformation. A fluid cannot* [1]. This definition facilitates the application of principles of classical continuum mechanics to determine if a substance is a fluid or solid. By applying Newton's second law of motion to a body of fluid Claude-Louis Navier and George Gabriel Stokes developed a set of equations to describe the motion of a fluid in response to these forces (See Appendix E). Known as the Navier-Stokes equations, they are particularly useful in describing a large number of fluid-based phenomena including the studies of the ocean currents [2], blood flow in the heart [3], and compressible flow across an aerofoil [4]. When the complexity of many real world problems

is added to the second order and non-linear nature of the equations they become computationally intensive to solve and in many cases only approximate solutions can be obtained. The development of Computational Fluid Dynamics (CFD) has allowed many different solution strategies to become available to the desktop user. CFD software packages are available from both free and commercial sources. When considering the application of fluid mechanics to MEMS devices, a number of assumptions can be made to allow for a significant simplification of the governing equations. The flow in microsystems are predominantly laminar due primarily to the small length scales of these devices. This allows the removal of the rotational components of the Navier-Stokes equations and dictates that viscous effects dominate over inertial effects, thereby also removing gravitational aspects for many devices. An exact solution for some microfluidic devices can be obtained by making some further assumptions and in the case of devices incorporating a whole blood sample the assumption that the blood is Newtonian fluid can also be made [5]. Although blood is non-Newtonian this assumption can be justified when considering the shear thinning response of whole blood as shown in Figure 2.1.

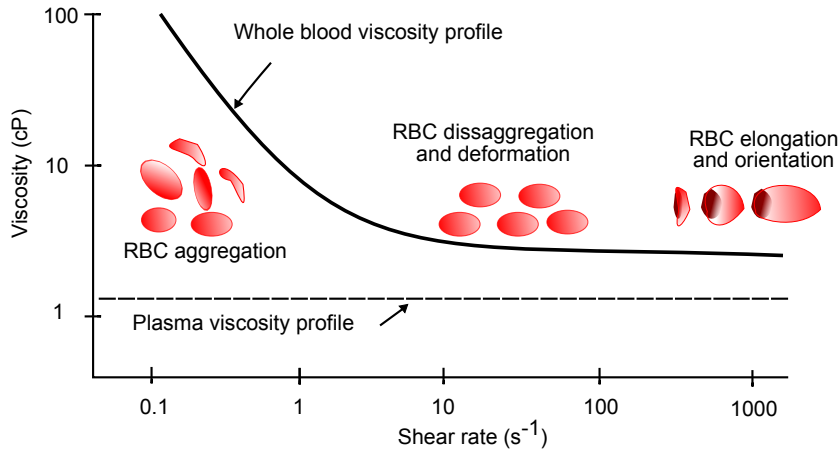


Figure 2.1: Diagram showing the relationship between apparent viscosity of normal blood, plasma at various shear rates made [6].

Figure 2.1 shows that as the shear rate increases. The deformation of the red cells starts, causing a reduction in the recorded viscosity. The rate of deformation starts to stabilise at about 10 s^{-1} and has fully completed at a shear rate of 50 s^{-1} , after which the viscosity of blood remains constant [7]. For the purposes of this work whole blood can be considered a Newtonian fluid as platelet response to shear is typically in the range of 50 s^{-1} to 1000 s^{-1} [8].

2.1 Fluid Flow Within Channels

Section 3.1 introduces the concept of degas-driven flow. A degas-driven channel flow can be approximated as steady flow between parallel plates. However, the flow rate within the channel of a degas-driven device is nonlinear. A model that accounts for the diffusivity of air in Polydimethylsiloxane (PDMS) is also detailed in this section.

Chapter 5 introduces a sealed device that uses a rocking-table to create flow within the channel. The flow rate within these channels can be approximated by treating it as flow down an inclined plane. The theoretical background for these conditions has also been detailed within this section.

2.1.1 Steady Flow Between Parallel Plates

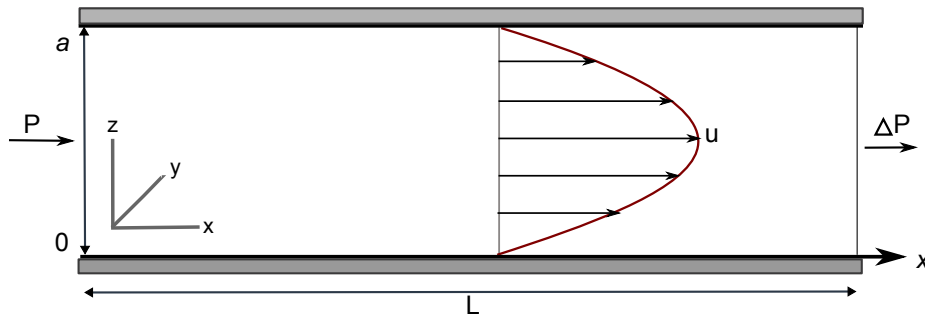


Figure 2.2: Flow between parallel plates.

Consider a fluid of viscosity μ , flowing between two fixed, infinitely wide parallel plates of length L , separated by a distance a as shown in Figure 2.2. Assuming the flow is steady (all partial derivatives with respect to time are zero), parallel (the xy -component of velocity u is zero everywhere), fully developed and laminar, and there is a constant pressure drop along the length L the Navier-Stokes equations can be simplified, with a full derivation included in Appendix C. Under these conditions the flow can be considered one dimensional, with the velocity u constant along the z direction. When these conditions are applied Navier-Stokes equations can be reduced to yield the equation for flow between stationary horizontal plates shown in Eq. 5.1, where Q is the fluid flow rate, p is the pressure, a and b are channel height and width, and μ is the fluid viscosity [9].

$$Q = \frac{a^3 b}{12\mu} \frac{dp}{dx} \quad (2.1)$$

Shear Rate

Shear rate is an important parameter to be considered when blood is flown between parallel plates. The adhesion of platelets can be dependent on both a minimum and maximum shear rate. To calculate the wall shear force, τ_w , we use the shear force equation.

$$\tau_w = \mu \left| \frac{du}{dz} \right|_{z=0, z=a} = \frac{a}{2} \frac{dp}{dx} \quad (2.2)$$

For practical analysis, Eq. 2.1 and Eq. 2.2 can be combined to give

$$\tau_w = \frac{6\mu Q}{a^2 b} \quad (2.3)$$

which allows the calculation of wall shear force in terms of chamber dimensions, fluid viscosity and volume flow rate.

Aspect Ratio

Eq. 5.1 shows the approximate expression for the flow rate in flat rectangular channels. This is a highly aspect-ratio-dependent approximation of volume flow rate and breaks down as the aspect ratio approaches 1. In the case of an aspect ratio of one third, $a = w/3$, the error is as much as 23%, where a is the channel height and w is the width. This error falls to 7% for an aspect ratio of one tenth, $a = w/10$ [10]. During the design of microfluidic channels the aspect ratio needs to be greater than one tenth for an error less than 7%.

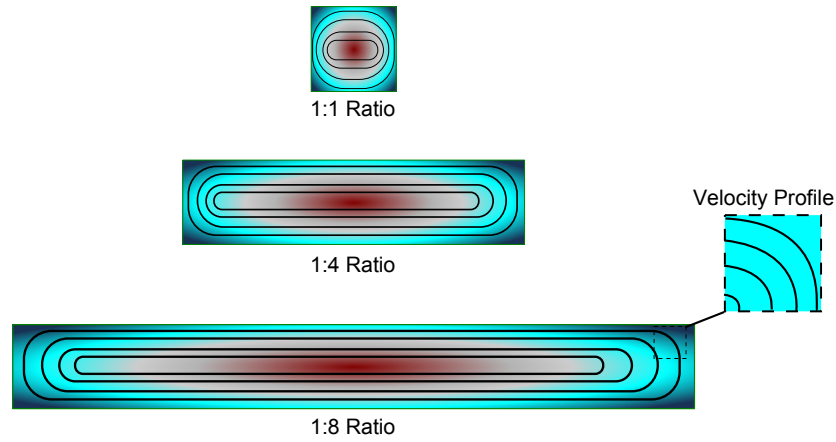


Figure 2.3: Velocity profiles through rectangular ducts of varying aspect ratios.

Figure 2.3 shows channels with an aspect ratio of 1:1, 1:4 and 1:8, with the velocity profile highlighted for each. Comparing the velocity profile between channels of increasing aspect ratio (1:1 to 1:8) the impact upon the profile as a result of the vertical wall is decreased, thereby allowing for the flow to be assumed as one dimensional. This simplification in the governing equations also allows for the flow rate, and therefore the shear rate, to be considered constant across most of the channel width.

2.1.2 Degas-Driven Flow Model

The same equations derive for flow between parallel plates can be used for flow within a degas-driven flow (DDF) channel. The flow rate within a DDF channel decreases over time, while flow within a parallel plate flow device remains constant. The channel designs developed within Chapters 3 and 5 utilise DDF and therefore a model used to approximate the change in flow rate with respect to time is derived.

DDF allows for passive pumping along a dead-end channel and is detailed within Section 3.1. DDF does not require any tubing, additional equipment or power source typically used with other pumping methods. DDF utilises both the gas solubility and permeability properties of PDMS to transport a fluid along a channel length. The channel is moulded within the PDMS block and has only one inlet, created by punching a hole into one end of the channel, to create a dead end channel.

A degas-driven flow model has been proposed by Liang *et. al.* to describe the air flux from the micro channel into the PDMS bulk [11], denoted in the Eq. 2.4 as $Flux_{air}$. The model takes advantage of the equation described by Hosokawa *et. al.* [12] and was adapted with the addition of a scaling factor (C_{atm}), required to account for the difference in the geometries of the two systems. Eq. 2.4 was derived from Fick's laws of diffusion assuming a 1-D system and concentration of air (C_{PDMS}) inside the PDMS of zero after degassing and before the experiments. Where the air concentration in the atmosphere is C_{atm} , D_{PDMS} is the diffusivity of air in PDMS, L_{PDMS} the thickness of PDMS, and t_{idle} represents the post-vacuum idle time before loading the liquid into the channel.

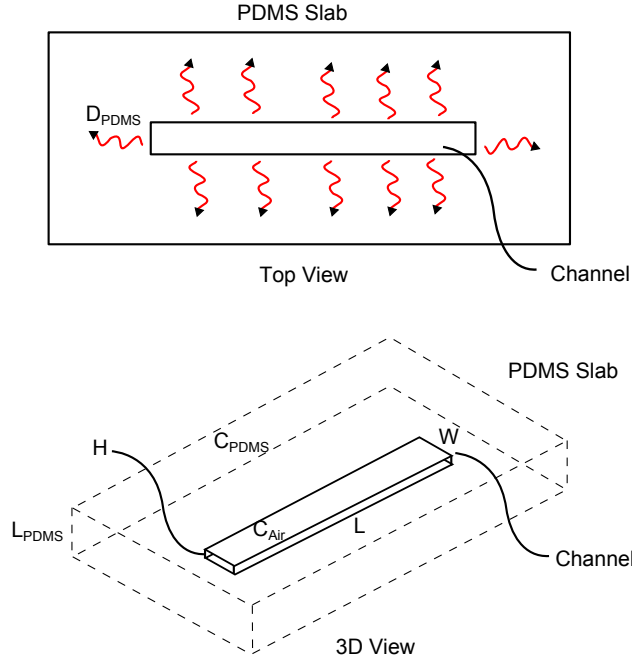


Figure 2.4: Permeability of PDMS slab. Two views of a channel inside a PDMS slab are shown to demonstrate the diffusion of air into the material. The important values used to calculate the flux are also labelled.

$$Flux_{air} = K_2 2D_{PDMS} \left(\frac{C_{atm} - C_{PDMS}}{L_{PDMS}} \right) \exp \left(\frac{-\pi^2 D_{PDMS} (t + t_{idle})}{4L_{PDMS}^2} \right) \quad (2.4)$$

The model assumes Poiseuille flow within a square channel where L , W and H describe the length, width and height, respectively. When calculating the fluidic resistance ($R_{fluidic}$) a scaling factor was required to account for complex factors such as surface tension and the hydrophobicity of PDMS. The fluidic resistance is described in Eq. 2.5, where μ is the fluid viscosity and can be used to determine the volumetric flow rate Q (Eq. 2.6).

$$R_{fluidic} = \frac{12\mu L(W + H)^2}{(WH)^3 \left(1 + \frac{5H}{6W}\right)} \quad (2.5)$$

$$Q = \frac{dP}{R_{fluidic}} \quad (2.6)$$

Assuming the air acts as an ideal gas, the pressure difference can be equated to P_{atm} , the amount of air inside the channel ($n_{channel}$) and the fluid-free, gas-filled volume (V_{free}). The ideal gas law is shown in Eq. 2.7 where P is pressure, R is gas constant, T is temperature, mass (m) and the molar mass (M) (in grams per mole):

Ideal gas law:

$$n = \frac{m}{M} \quad PV = nRT \quad (2.7)$$

Therefore, the pressure difference for the modelled channel can be derived as:

$$dP = P_{atm} - \frac{n_{channel}RT}{V_{free}} \quad (2.8)$$

Where P_{atm} is atmospheric pressure.

$n_{channel}$ can be related to the flux of air using the relationship:

$$n_{channel} = n_{initial} - \int_0^t Flex_{air} A_{free} dt \quad (2.9)$$

Where $n_{initial}$ is the total air inside the channel at $t = 0$ and A_{free} is the available surface area exposed to air. Therefore, the free volume V_{free} and free area A_{free} can be given by:

By substituting Eq. (2.5) and (2.8) into Eq. (2.6) Q can be expressed in terms of:

$$Q = K_1 \frac{(WH)^3(1 + \frac{5H}{6W})}{12\eta L(W + H)^2} \left(P_{atm} - \frac{n_{channel}RT}{V_{free}} \right) \quad (2.10)$$

By substituting Eq. (2.4) into Eq. (2.9) $n_{channel}$ can now be expressed in terms of:

$$n_{channel} = \frac{P_{atm}WHL}{RT} - K_2 2D_{PDMS} \left(\frac{C_{atm} - C_{PDMS}}{L_{PDMS}} \right) \exp \left(\frac{-\pi^2 D_{PDMS}(t + t_{idle})}{4L_{PDMS}^2} \right) A_{free} dt \quad (2.11)$$

Applying the boundary conditions for $t = 0$;

$$\frac{DA_{free}}{dt} = -\frac{2(W + H)}{WH}Q \quad (2.12)$$

$$\frac{dV_{free0}}{dt} = Q \quad (2.13)$$

$$\frac{n_{channel}}{dt} = -K_2 2D_{PDMS} \left(\frac{C_{atm} - C_{PDMS}}{L_{PDMS}} \right) \exp \left(\frac{-\pi^2 D_{PDMS}(t + t_{idle})}{4L_{PDMS}^2} \right) A_{free} \quad (2.14)$$

Therefore, the free area and volume at $t = 0$ is

$$A_{free0} = 2L(W + H) + A_{end} \quad (2.15)$$

$$V_{free0} = WHL \quad (2.16)$$

$$n_{channel} = \frac{P_{atm}WHL}{RT} \quad (2.17)$$

Resulting in the following:

$$\frac{dQ}{dt} = -K_1 \left(\frac{(WH)^3(1 + \frac{5H}{6W})}{12\eta L(W + H)^2} \right) RT \left[\left(\frac{1}{V_{free}} \right) \frac{dn_{channel}}{dt} - \left(\frac{n}{V_{free}^2} \right) \frac{dv_{free}}{dt} \right] \quad (2.18)$$

$$\frac{dQ}{dt} = -K_1 \left(\frac{(WH)^3 (1 + \frac{5H}{6W})}{12\eta L (W + H)^2} \right) RT \left[\left(\frac{n}{V_{free}^2} \right) Q - \left(\frac{1}{V_{free}} \right) \left(K_2 2D_{PDMS} \left(\frac{C_{atm} - C_{PDMS}}{L_{PDMS}} \right) \exp \left(\frac{-\pi^2 D_{PDMS} (t + t_{idle})}{4L_{PDMS}^2} \right) A_{free} \right) \right] \quad (2.19)$$

While Liang *et. al.* (2011) reported a good correlation between experimental and modelled volumetric flow rates (Q) the values used for K_1 and K_2 need to be determined experimentally and may not take into account complex channel geometries like those detailed in Chapter 4. As such, this model is of limited value and in many cases an experimental approach should be taken when designing such devices.

2.1.3 Rocking Table

The iPA assay uses a rocking table to allow the blood to flow across the protein spots. The height of the blood changes as the rocker moves from side to side. This section details two methods for calculating this height. Software was also developed to help characterise the moving of the rocking table as is detailed in Appendix E.

Software

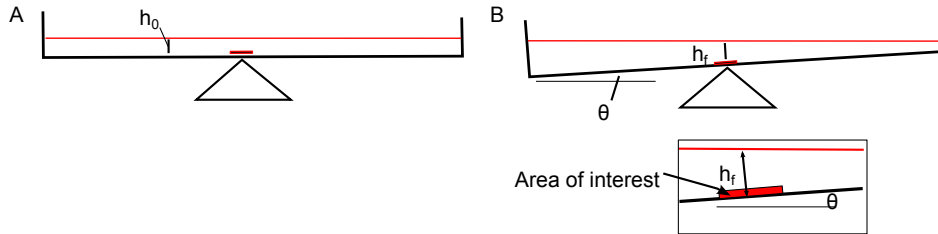


Figure 2.5: A) Channel at zero degrees ($h = h_0$). B) Channel at θ therefore $h = h_f$

Software allows for the changes in angle of the rocking table to be recorded over time. As the slow moving rocking table oscillates the height h will change across the area of interest, located half way along the channels length. Figure 2.5 shows the rocking table at 0° and inclined at an angle θ . The interface between the fluid and air remains horizontal despite the angle of tilt causing the fluid height to change as the table moves. The following equations used to calculate the fluid height assume the table movement is sinusoidal and at a constant speed.

$$\theta = \theta_{max} \sin \frac{2\pi t}{T} \quad (2.20)$$

$$h_f = h_0 + (L/2 - x) \tan \theta \quad \theta \leq \theta_0 \quad (2.21)$$

$$h_f = \sqrt{2h_0 L \tan \theta} - x \tan \theta \quad \theta \geq \theta_0 \quad (2.22)$$

For a rocking angle θ , assuming a sinusoidal function, at time t with a maximum table angle of θ_{max} for a time period of T , h_f should be used in Eq. 2.27 when calculating the flow rate.

Flow Down an Inclined Plane

In many microfluidic devices the fluid is transported through a channel completely bound by both the upper and lower boundary, as detailed in Section 2.1.1. Flow within a rocking table can be approximated as flow down an inclined plain when calculating the height of the fluid. The equation that governs such flow can be derived from the Navier-Stokes equations by making the same simplifications used for flow between parallel plates, thereby yielding.

$$\frac{\partial^2 u}{\partial z^2} = \frac{1}{\mu} \frac{\partial p}{\partial x} \quad (2.23)$$

where x and z are coordinates along and normal to the plate, u is the velocity components in z , p is pressure and μ is the viscosity of the fluid.

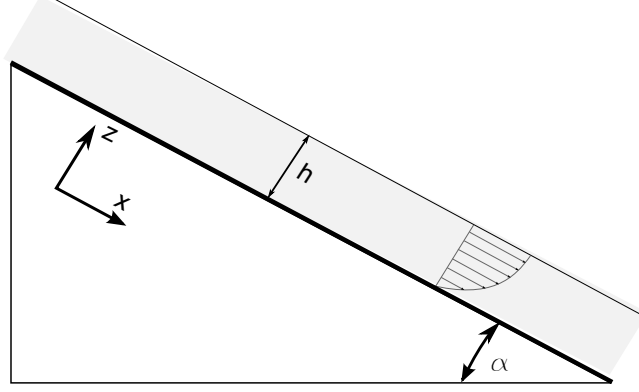


Figure 2.6: Viscous flow down an inclined plane.

Figure 2.6 shows fluid flowing down a inclined plane at an angle α where x distance along the plane where z is the transverse coordinate so the surface of the plane corresponds to $z = 0$ and the fluid forms a uniform layer of depth h over the surface. g is the acceleration due to gravity. In this case, there is no gradient in the actual pressure in the x -direction, and the flow down the plane is driven entirely by gravity.

Therefore, for fluid flowing down a inclined plane we can write.

$$\frac{\partial^2 u}{\partial z^2} = -\frac{\rho g \sin \alpha}{\mu} \quad (2.24)$$

Where, ρ is the density of the fluid.

The application of the no slip condition at the surface of the plane, $z = 0$, yields the boundary condition $u = 0$. A second boundary condition can be determined by assuming that the finite inertia and viscosity of air are both negligible at the fluid/air interface, $z = h$. The normal viscous stress σ_{xz} can be let equal zero ($\sigma_{xz}|_{z=h} = 0$) by assuming there is nothing above this interface that can exchange momentum with the fluid. This allows the following boundary conditions to be applied.

$$\begin{aligned} u &= 0 \quad @ \quad z = 0 \\ \frac{du}{dz} &= 0 \quad @ \quad z = h \end{aligned} \tag{2.25}$$

applying these boundary conditions yields

$$u = \frac{\rho g \sin \alpha}{2 \mu} z (2 h - z). \tag{2.26}$$

The profile remains parabolic and is the same as the lower half of the profile obtained when fluid flows between parallel plates at a distance $2 h$ apart (Figure 2.6).

The flow rate Q through a section of with a width w , where b is the unit width, and height h can be approximated by [13, 14]

$$Q = \int_0^h u dz = \frac{\rho g \sin \alpha h^3}{3 \mu} \tag{2.27}$$

For a given flow rate (Q) the depth of the layer covering the plane becomes.

$$h = \left(\frac{3 \mu Q}{\rho g \sin \alpha} \right)^{1/3}. \tag{2.28}$$

Bibliography

- [1] F M White. *Fluid Mechanics*. McGraw-Hill, 2003.
- [2] John Marshall, Alistair Adcroft, Chris Hill, Lev Perelman, and Curt Heisey. A finite-volume, incompressible Navier Stokes model for studies of the ocean on parallel computers. *Journal of Geophysical Research*, 102(C3):5753, 1997.
- [3] Charles S Peskin. Numerical analysis of blood flow in the heart. *Journal of Computational Physics*, 25(3):220–252, November 1977.
- [4] F. Bassi and S. Rebay. A High-Order Accurate Discontinuous Finite Element Method for the Numerical Solution of the Compressible Navier-Stokes Equations. *Journal of Computational Physics*, 131(2):267–279, March 1997.
- [5] Alan D Michelson. *Platelets Second Ed*. Elsevier Academic Press, 2007.
- [6] T Somer and H J Meiselman. Disorders of blood viscosity. *Annals of Medicine*, 25(1):31–9, February 1993.
- [7] Hong Zhao and Eric S. G. Shaqfeh. Shear-induced platelet margination in a microchannel. *Physical Review E*, 83(6):061924, June 2011.
- [8] M H Kroll, J D Hellums, L V McIntire, A I Schafer, and J L Moake. Platelets and shear stress. *Blood*, 88(5):1525–1541, September 1996.

- [9] Y Cengel and J Cimbala. *Fluid Mechanics Fundamentals and Applications*. McGraw-Hill Education, 3rd edition, 2013.
- [10] Henrik Bruus. *Theoretical microfluidics*, volume 18. OUP Oxford, 2007.
- [11] David Y Liang, Augusto M Tentori, Ivan K Dimov, and Luke P Lee. Systematic characterization of degas-driven flow for poly(dimethylsiloxane) microfluidic devices. *Biomicrofluidics*, 5(2):024108, June 2011.
- [12] Kazuo Hosokawa, Kae Sato, Naoki Ichikawa, and Mizuo Maeda. Power-free poly(dimethylsiloxane) microfluidic devices for gold nanoparticle-based DNA analysis. *Lab Chip*, 4(3):181–5, June 2004.
- [13] Gabriella Bogнар, Krisztian Hriczo, and Imre Gombkoto. Non-Newtonian fluid flow down an inclined plane. ...*International Conference on Fluid ...*, 2(1):129–134, 2011.
- [14] Constantine Pozrikidis. *Fluid Dynamics: Theory, Computation, and Numerical Simulation*. Springer Science & Business Media, 2009.

Chapter 3

Characterisation Of Degas-Driven Flow

Advances in microfluidic technologies have allowed for the development of new, low-cost point-of-care devices (POC). These devices offer a number of advantages including automation of manual steps, improvements in assay accuracy, reduced reagent costs, minimising sample volumes and a decrease in the overall analysis time [1, 2]. Microfluidic platforms enable the study of single cells and cell populations by accurately controlling fluid dynamics (e.g. shear rate), effectively handling small fluid volumes, localised compound delivery and facilitating the imaging and analysis for both real time and stationery applications [3]. POC devices can allow for current complex laboratory assays to be simplified, thereby giving access to testing in areas of the world where traveling to a clinic or the storage and delivery of a sample may be impossible [4, 5]. Current shear-dependent platelet function tests, such as the Analyzer-100 (PFA-100), Impact-R cone & plate(let), and VerifyNow, require mL sample volumes and/or complex cartridges or electronics [6, 7]. When designing a flow-based device, where shear rate is required or may have a detrimental effect on assay performance, it is critical

to control and understand both the shear rate and flow rate achieved within the device.

Self-pumped devices do not rely on large equipment such as syringe pumps. These pumps are traditionally used in research or clinical laboratories and render many microfluidic techniques ill-suited for use as POC devices. Self-powered microfluidic devices were previously reported using technologies such as gravity-driven [8], evaporation [9] and droplet based passive flow [10]. The requirement for gravity-driven devices to be primed before use and the associated difficulty in achieving reproducible flow (under normal clinic conditions) for both evaporation and droplet based passive flow, show these technologies still have a number of disadvantages, which may render them unsuitable for use as low-cost POC devices. Degas-Driven Flow (DDF) is a power-free method of flow propulsion more suited to point-of-care devices, proposed by Hosokawa *et al.* DDF allows for power-free pumping of fluid within a dead-end channel [11]. The characterisation of a $50\ \mu\text{m} \times 50\ \mu\text{m}$ degas-driven device was demonstrated by Liang *et al.* The device showed reproducible flow after being placed under vacuum (degassed) for 45min. The device was still capable of stable flow after being left idle for 7min [12]. The device was able to obtain a maximum flow velocity ranging from 0.2 to 3 nL/s and the area of exposed polydimethylsiloxane (PDMS) was found to have negligible effects on the fluid flow [12]. Self-pumped integrated DDF devices have also been demonstrated with both an on-chip sequential injection immunoassay [13] and an integrated microfluidic blood analysis system [14]. These devices do not require any external connections, tethers, or tubing and work with serum and whole-blood, respectively. However, for shear dependent assays, such as platelet function testing, a flow rate within microliters per second ($\mu\text{L/s}$) range is required for a channel geometry with an aspect ratio greater than 1/10, as shown in Section 2.1.1. The channel is also required to store the sample once it

has passed over the test area, unlike flow chambers where a syringe can be used to store the sample. Many shear dependent assays require the shear rate to stay within a defined maximum and minimum range. This creates a unique set of challenges when designing DDF devices, where the flow rate, and therefore the shear rate, will decline as the fluid fills the channel.

This chapter introduces a new low cost manufacturing method for the rapid development of DDF devices and a novel software package that allows the calculation of flow rate within complex channel geometries. This manufacturing method was used to develop and characterise a self-powered disposable microfluidic DDF chip. The chips were designed to better understand how the flow rate, and thus the shear rate, could be controlled over time. To better understand the capabilities of DDF flow and how channel geometry could be utilized, a number of different channel geometries of varying widths and lengths were characterised.

3.1 Principles Of Degas Driven Flow

Degas-driven flow utilises both the gas solubility and permeability properties of PDMS to transport a fluid along a channel length. The channel is moulded within the PDMS slab and has only one inlet, created by punching a hole into one end of the channel. Polydimethylsiloxane (PDMS) is an excellent material for the fabrication and rapid prototyping of microfluidic devices which incorporate biological samples. It is nontoxic, has a low curing temperature and allows a reversible seal to be formed between the PDMS and substrate. When PDMS is placed under a vacuum any gas within the bulk is evacuated. Once returned to atmosphere gas is slowly reabsorbed into the PDMS. Figure 3.1-A shows how the reabsorption of air can be used to create fluid flow within a dead end channel. This technique is referred to as degas-driven flow (DDF). The PDMS and substrate are

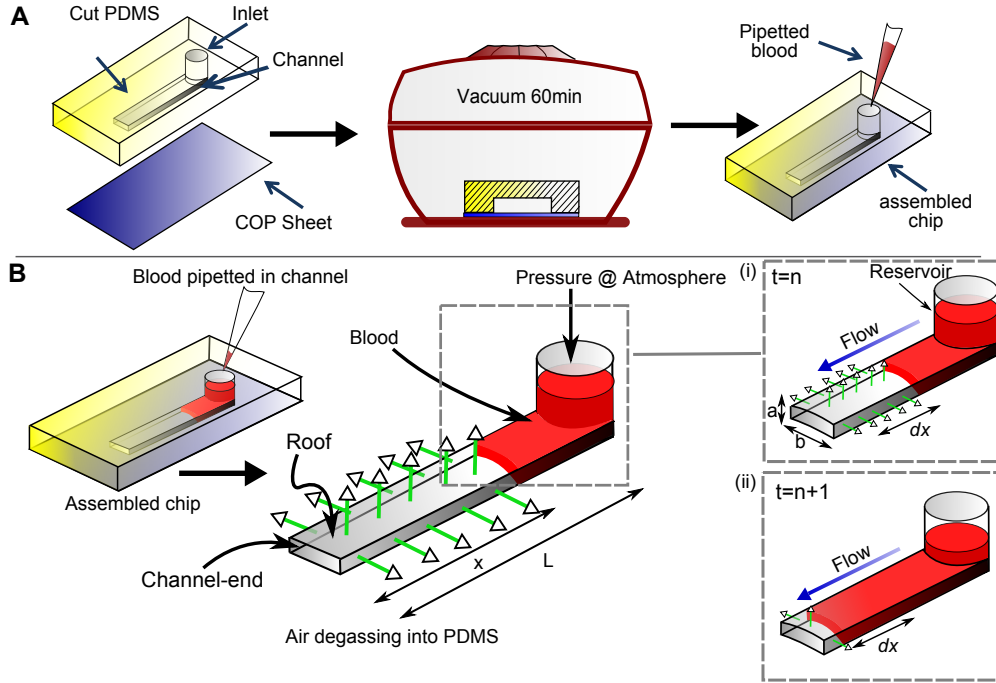


Figure 3.1: Principle and of degas-driven flow device. A) Assembly of DDF device using PDMS slab and poly(cycloolefin) (COP) sheet. B) Principle of DDF flow shown in a single length channel. i) Diagram of a section of the channel with a total length (L) as the fluid enters and the air starts to degas at $t = 0$. ii) Diagram of a section of the channel after the flow has moved a length dx along the total length (L) thereby reducing the available channel by $x - dx$.

assembled before the DDF device is placed into a vacuum and degassed for a predefined time; this allows any air (and water vapour) molecules within the PDMS bulk to be evacuated. As soon as the device is removed from the vacuum, the open channel will refill immediately while the PDMS bulk will slowly start to reabsorb air back through both its external faces and the channel walls (Figure 3.1-B). A difference between atmospheric pressure and the pressure within the channel is created once the sample is loaded into the inlet, thereby closing off the channel, allowing no new air to enter the channel and replace that absorbed through the channel walls. It is this pressure difference that causes the fluid to flow along the channel and will only stop when the PDMS becomes saturated with air or the pressure difference can no longer overcome the surface energy. Figure 3.1-B shows

a simple channel within the assembled chip. The sample has been loaded and the fluid is moving along the channels length (L). Two sections of the channel have been magnified to show the fluid at time $t = n$ and $t = n + 1$. The fluid moves a length dx between these time points. The flow rate decreases over time as the available pumping area (area of exposed PDMS) decreases by a length $x - dx$, where x is the length of the unfilled channel. The available pumping area for time t within the dead-end DDF channel is calculated from the channel height a , width b and length x , and only includes the two side-walls, roof and channel-end.

3.2 Manufacture of PDMS Chip

Photolithography is the traditional method used for microchannel fabrication. Photolithography typically requires relatively expensive equipment, a mask to be manufactured, photoresist and in some cases a cleanroom. In contrast the cost and ease of creating or modifying a design using a pressure sensitive adhesive (PSA) allows for rapid prototyping from the lab bench using a PSA cutter. Pressure sensitive adhesive is used in applications from automotive interior trim assembly to transdermal drug patches, with the former designed for permanent adhesion and the latter when reversible adhesion is required.

To manufacture the device channel, designs were created using the Autodesk AutoCAD 2012 software and saved in the AutoCAD DXF (Drawing Exchange Format) CAD data file format which enables data interoperability between AutoCAD and other programs. The channels were cut into a single-sided PSA sheet of 50 μm or 80 μm thickness. Figure 3.2-A shows the PSA being first placed onto a reusable backing sheet before the start point of the cutter is selected. A number of test cuts are made to allow the operator to set the depth of the blade; once cut, the design is removed from

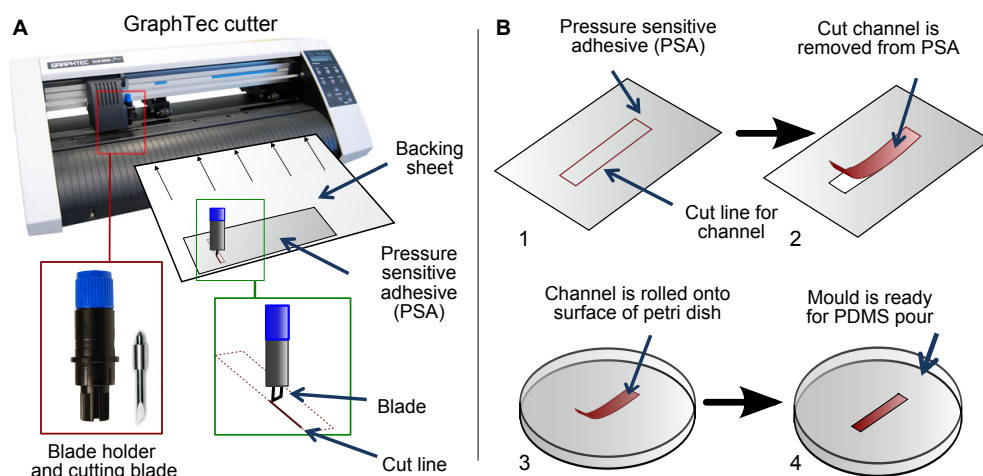


Figure 3.2: Preparation of PSA mould for manufacture of PDMS Chip. A) The location of the GraphTec cutter blade and housing are shown along with the backing sheet. B) Shows the four steps required to remove the channel from the waste PSA and roll it onto the surface of a petri dish.

the backing sheet. Figure 3.2-B illustrates how the channel is rolled onto the surface of a clean petro dish. The dish can be placed in the oven at 70° for 30 minutes to remove any air trapped beneath the adhesive.

A 10:1 mix of PDMS and curing agent is mixed and poured into the mould covering the channels completely. The channel designs are placed at the centre of each dish to ensure an even depth of PDMS and to reduce any possible damage to the channels when the PDMS is removed with the aid of a scalpel. The bubbles that were introduced into the PDMS as it was mixed are removed by placing the dish under vacuum for 1 hour 30 minutes or until no bubbles are visible, before curing for 60 minutes at 70° . The now cured block of PDMS must be allowed to cool before it is ready to be removed from the dish. As the mould is reusable care is taken to ensure the surface of the dish is not scratched upon lift-off of the PDMS slab. Each channel within the block is cut into individual chips and an inlet punched at the start of the channel, taking care to remove any PDMS flakes that may affect how the chip bonds to the substrate. When the chip is placed

onto the substrate, a reversible bond creates the sealed channel with a single inlet required for degas-driven flow.

Finish of Channel Edge

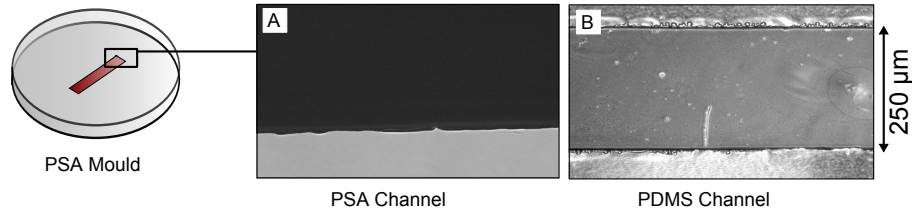


Figure 3.3: Microscope Images (20x magnification) of (A) PSA the mould alongside an image of (B) the channel in PDMS chip created from the mould.

Figure 3.3 shows the finish achieved at the edge of the PSA channel and the edge of the channel when cast in PDMS. The PSA image shows small inconsistencies along the channel edge as the blade cuts the PSA. When this is compared to the channel cast in PDMS, these inconsistencies are still visible alongside a number of bubbles which were not removed when the mix was placed under vacuum. Although a better defined channel edge can be achieved when using photolithography, the finish achieved using a PSA mould should be acceptable. Given that the channels have a low aspect ratio and only the centre will act as an assay area, the overall finish will be suitable for prototype channel development. However, as this manufacturing technique had not yet been characterised, software was developed to detect flow rates. By comparing flow rates across different moulds and channel geometries, it was possible to determine if the flow was reproducible.

3.3 Flow Rate Detection Software

Within this thesis two distinct image processing techniques were developed for the analysis of fluid flow. The first allows for the analysis of simple

channel geometries, while the second can analyse complex channel geometries with multiple directions of fluid flow. The software was developed to replace a manual system that required the user to record the time at which the fluid passed from one square of a grid to the next; with the area of each square known the flow rate could be calculated. This technique was time-consuming, required the user to observe the flow for the full run time and limited the number of data points to the density of the grid. By automating this process inter-user variability for flow rate calculations could be removed along with the need to observe the flow, freeing the operator to complete other tasks. Both techniques used a webcam positioned above the chip, and were available within a single software package developed in C++ as part of this thesis.

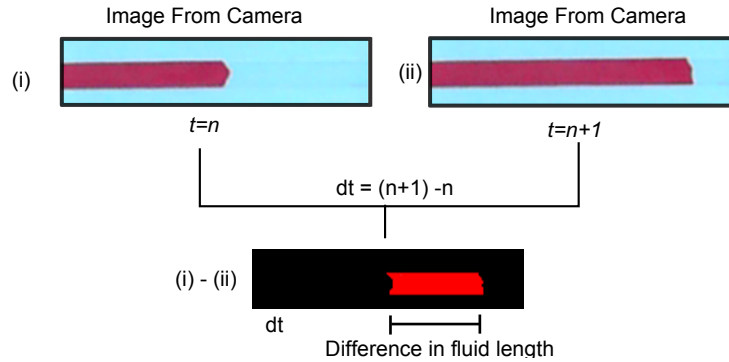


Figure 3.4: Calculation of flow rate using acquired images

Figure 3.4 show two images at $t = n$ and $t = n + 1$. These images were acquired from the camera, before being processed to determine the length the fluid had travelled between $t = n$ and $t = n + 1$. This length can be used to calculate the velocity of the fluid during the time dt . Given that the channel is of known width and height the velocity can in turn be used to calculate the volumetric flow rate (Q). The processing steps and calculations required are detailed in Appendix D

3.3.1 Analyses of Complex Channel Geometries

The simple allowed for the analyses of simple rectangular channels. Degas devices can also contain channels that can vary in width along their length, contain bifurcations, corners, curves or other complex features. Non-rectangular channels therefore required a new flow rate detection technique to be developed. As multiple channel designs required characterisation it was important that the new technique was robust, flexible, automated and easy to use. A novel flow detection method was developed to calculate the flow rate in complex channels. Complex channel flow detection (CCFD) reads in the DXF file that stores all the point data needed to build an outline of the drawing it contains. A channel design was drawn using AutoCAD, this DXF file was readily available.

Figure 3.5-1 shows the image as it is acquired from the camera. The image is processed (Figure 3.5-2), before a stencil is applied to create a series of images used to calculate the flow rate. The channel DXF file is used to create a stencil which is placed over the channel within the image. Figure 3.5-4 shows a stencil applied at a number of different time point $t=n$ to $t=n+4$. The regions extracted from the input images are of the same size as the stencil, with any non-zero value considered fluid as only areas inside the polygon (channel) are included. This makes it possible to calculate the area (m^2) of the filled channel, for each of the regions extracted, and by multiplying the area by the channel height ($50 \mu m$) the total volume of fluid within the channel can be determine for all time points.

Each image is time stamped allowing for both the time and difference in volume between n and $n+1$ to easily be determined, in turn allowing for the volumetric flow rate (Q) for each time point to be recorded. The methods used to create the stencil and filters used to detect the flow rate for complex channels are detailed in Appendix D.

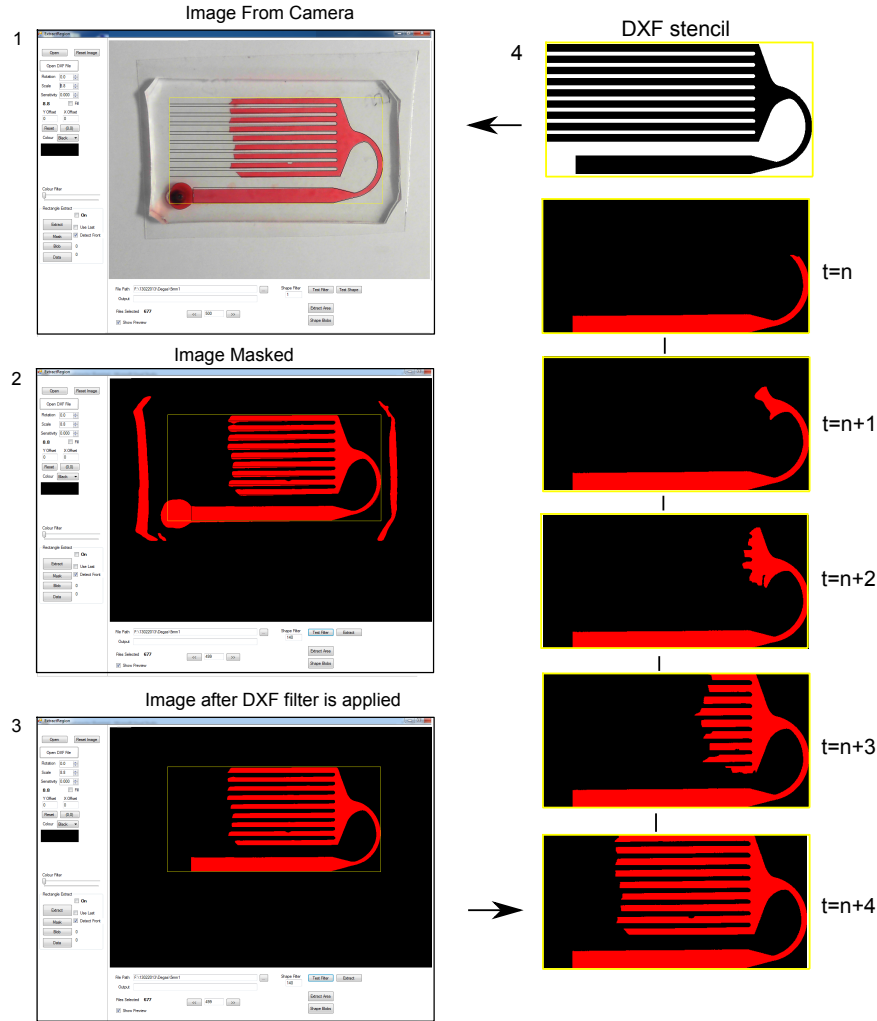


Figure 3.5: Screen shot of software used to calculate flow rates for a complex channel using a DXF file. 1-2) The imported DXF file is shown in a yellow box, the box is placed over the image before a threshold is applied. 3) The DXF stencil is applied to the threshold image which sets any pixel outside of the channel to 0 (black) and at the same time crops the image to the stencil size. 4) Image of the stencil and a series of cropped images showing how only the area within the channel is extracted from each image.

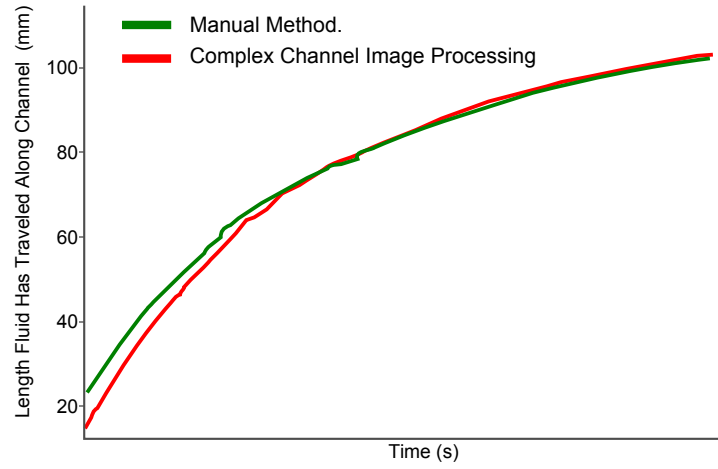


Figure 3.6: Simple and complex flow rate detection methods compared.

Figure 3.6 shows the complex method compared well to the manual method when a channel of 120 *mm* in length was used to make the comparison. As the user records the distance the fluid has travelled along a channel, this value was plotted within the graph for both methods. The manual method is quicker to set-up, as no stencil is required, but is limited to only straight channels. While the complex method can process both straight and complex channels it required more set-up before any result can be calculated. Both methods required the user to know the width and height of the channel before a flow rate can be calculated.

3.3.2 Summary

This section introduced both a new manufacturing and flow detection method, for use with degas-driven flow devices. By using these techniques together, prototype DDF chip(s) could be designed and characterised at a low cost and in a short time frame. However, the chips manufactured using this new method had not yet been characterised. Therefore, a series of channels of varying width and length were tested with water.

3.4 Characterisation of DDF Flow

The characterised channel designs were cut into a pressure sensitive adhesive before being rolled onto the surface of a petri dish. Depending on the channel geometry a different size petri dish is required and should allow for a suitable area of Polydimethylsiloxane (PDMS) surrounding the channel, thereby allowing the PDMS to create an air tight seal with the substrate. Figure 3.7 illustrates how the dish is filled with a mixture of PDMS and curing agent, before being heated and allowed to cure. Once cured, the slab can be removed from the dish and cut to size before the inlet is punched into one end of the channel. For each channel characterised, the volume of PDMS used results in a slab of the same height.

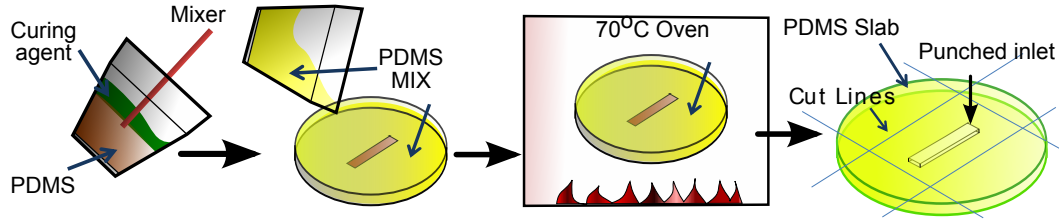


Figure 3.7: PDMS Mixing. The PDMS is first mixed (10:1) before it can be poured into the mould and heated at 70°C for 60 min. Once cured, the slab can now be removed and cut to size.

In order to determine the flow rate of fluid through the channel, software was developed to acquire images from a camera and carry out the required post processing. The software outputs the fluid velocity, flow rate and shear rate and was used to acquire all data within this chapter.

$$\tau = Q \left(\frac{6\mu}{a^2b} \right) \quad (3.1)$$

Eq. 3.1 shows that shear rate (τ) can be calculated from the channel height (a), width (b), viscosity (μ) and volumetric flow rate (Q). Only changes in Q will affect the shear rate as a , b , and μ are constant for a given channel. However, the flow rate within DDF channels is affected by the area

of exposed PDMS which will change if channel geometry is altered. The height (a) of the pressure sensitive adhesive (PSA) used to create the DDF channel is fixed at $50\ \mu\text{m}$, allowing only the width (b) and channel length to be modified. If the width is changed when calculating the shear rate using Eq. 3.1, both the volumetric flow rate (Q) and channel width (b) will have an effect on the resulting shear rate. Therefore, to control the shear rate, the effect channel geometry has on the volumetric flow rate (Q) must first be understood. This was achieved by comparing channels of increasing width, with channels of constant width but with an increased length.

Table 3.1 shows the 13 channels used to characterise the flow rate, divided into two sets of 6 with 1 channel common to each set. For example, as the width of channel 1 was increased the length of channel 8 (of fixed width) was also increased, so the area of exposed PDMS would approximately match. For each channel, the average area of exposed PDMS was calculated by multiplying the length (L) by the width (b) by height (a) and the total footprint for each device was calculated by multiplying the length (L) by width (b). The analysis was simplified by assuming that the footprint area was equal to the area of exposed PDMS as the difference between the average area and total footprint was less than 6% (Table 3.1).

Flow Characteristics

Unlike many flow chamber devices, degas-driven chips do not have a syringe to store the fluid once it has passed over the assay area. This makes the ability to store the blood an important design consideration. It is also advantageous to ensure the test area is clear of blood, while allowing the required volume to pass through the channel for the assay to work. A clear assay area also allows efficient imaging of the surface of the chip. As can be seen in Figure 3.8-A, approximately 70% of the channel volume was














	Set 1 Channel 1-4 mm In Width 1-4 mm In Width		Set 2 Channel 20-80 mm In Length 20-80 mm In Length	Average Area Of Exposed PDMS (mm^2)	Foot Print (mm^2)
1		8		53.5	50
2		9		79	75
3		10		104.5	100
4				130	125
5		11		155.5	150
6		12		181	175
7		13		206.5	200

Table 3.1: List of 13 different geometries characterised. Split into two sets of corresponding footprint areas Set 1 contains channels changing in width from 1 to 4 mm in increments of 0.5 mm while Set 2 contains channels changing in length from 20 to 80 mm in increments of 10 mm. Channel 4 is included in both Sets 1 and 2. The average area of exposed PDMS (AAEP) is also listed alongside the foot print area (FPA) for each set of corresponding channels. AAEP includes all surfaces within the channel, while FPA only includes the top surface and not the side walls of the channel.

filled with fluid after 7min for all the channels listed in Table 3.1 with no significant difference across all geometries tested.

A typical flow rate profile for a 2.5 by 50 mm channel is shown in Figure 3.8-B, where a rapid increase in flow rate was observed for the first 100 seconds after the fluid was introduced into the channel (stage 1). After approximately 100 s or 10 % of the total time recorded the flow rate then progressively decreases from its maximum (stage 2), before gradually decreasing to a stop (stage 3). This result shows that flow rate within DDF channels is non-linear over time and therefore there is no average flow rate for a given channel. As shear rate plays an important role in platelet dependent assays, controlling the maximum and minimum flow rate, and thus the shear rate, is a key goal when designing new devices. For many shear dependent assays there is typically a range over which the sample can flow.

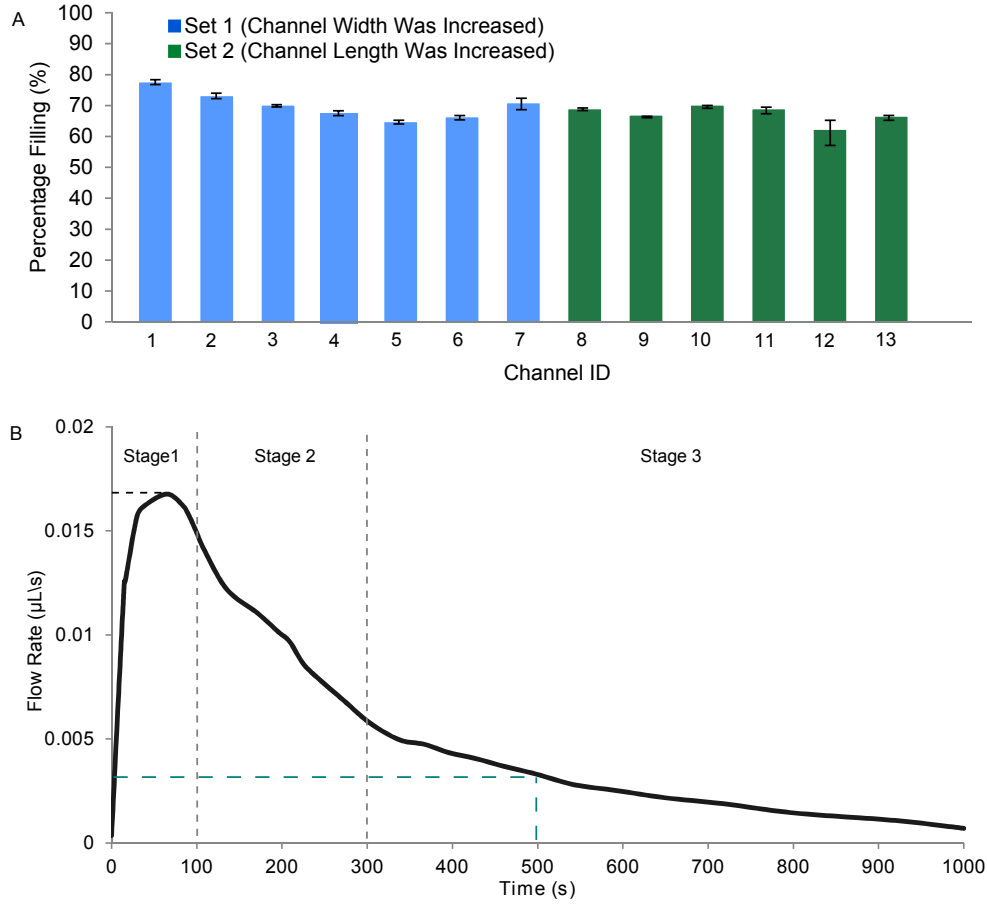


Figure 3.8: A) Percentage of channel filled after 1000s for both sets 1 and 2. B) Example of the flow rate profile for the first 1000s of flow in a DDF device split into three stages.

Effects of Channel Geometry on Flow Rate

The effects of geometry on flow rate were investigated for the channels set out in Table 3.1. The channels are split into two sets set 1 (variation in width) and set 2 (change in length). Channel IDs 1, 2, 3, 4, 5, 6 and 7 make up set 1 while channels with the ids 8, 9, 10, 4, 11, 12 and 13 make up set 2. To determine if reproducible flow could be achieved and the shear rate controlled between an upper and lower limit seven chips were tested for each channel design. Figure 3.9 shows the results of these tests. Figure 3.9-A details the maximum flow rate (maximum range) recorded for

each channel. The columns had been grouped by footprint area in order to highlight the effect channel geometry has on flow rate, when compared to a channel of equivalent footprint area. Figure 3.9-B shows the flow rate after 500 seconds, thereby representing the minimum range for an assay time of 500 seconds. This time point was selected as it matched the maximum time many flow based platelet assays are run.

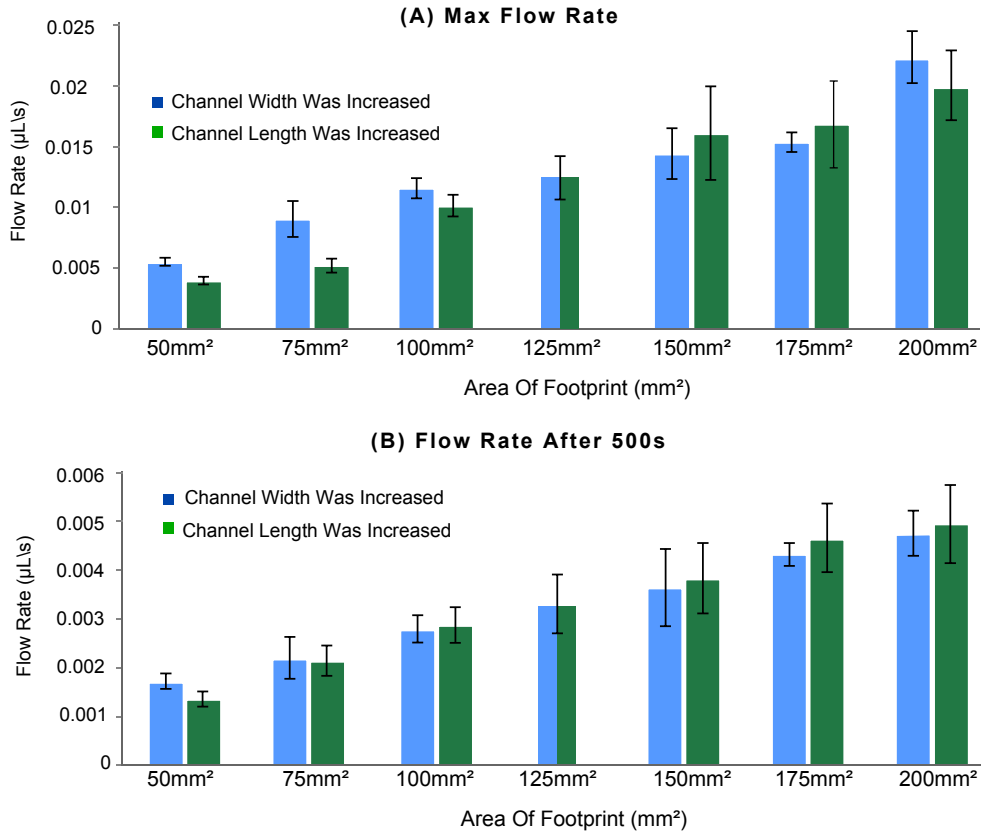


Figure 3.9: Comparison between devices with equivalent footprint areas. The maximum flow rate across different footprints (A), the flow rate after 500 seconds (B) were plotted. Set 1 includes channels of widths 1 mm to 4 mm while Set 2 includes channels 20 mm to 80 mm. As a channel id 4 is included in both sets of data only one column is shown. Each figure has an n=7.

As expected, increasing the area of exposed PDMS (pumping area) results in a corresponding increase in flow rate. This can be explained by equating the pressure difference created by DDF with that of a pump. In-

creasing the available pumping area affects how fast air can be removed from the channel resulting in a greater pressure difference, thereby increasing the flow rate within the DDF channel. This principle is shown in Figure 3.9 where a larger footprint area gave the greater flow rate, with the flow rate increasing as the area of exposed PDMS was increased across the 13 channel designs. The figure shows (A) the maximum recorded flow rate for each channel and (B) the flow rate after 500 seconds. No statistical difference in the flow rate across footprint areas of 75 mm^2 or greater, within both graphs. In contrast, variances were observed in areas 75 mm^2 and less, possibly as a result of the time taken to achieve gradual flow in shorter channel lengths. The data indicates that changes to the channel width do not affect the flow rate for equivalent footprint areas and a reproducible flow rate can be achieved. The results indicate the new manufacturing technique is suitable for use when designing prototype degas-driven chips.

Effects of Channel Geometry on Shear Rate

Shear rate (τ) plays a key role in how platelets function, platelets respond differently over a range of shear rates. It is therefore important to control shear rate within the channel of any prototype device, τ was calculated using Eq. 3.1. When calculating the τ for two channels, with fluid passing through them at an equivalent flow rate (Q), the cross sectional area of a channel has direct effect on the value of the shear rate calculated. As the height of the channels tested is fixed at $50 \text{ }\mu\text{m}$, only the width (b) will result in a change to the shear rate. Figure 3.9-A showed no significant effect on the maximum flow rate for channels with an equivalent footprint area. However, the channel width (b) was increased from 1 to 4 mm for those channels within Set 1. This change in width will therefore have an effect on the resulting shear rate, when compared to the channels of equivalent

footprint area within Set 2. This difference has been plotted in Figure 3.10 and shows how the maximum shear rate can be controlled by changing the geometry of the channel.

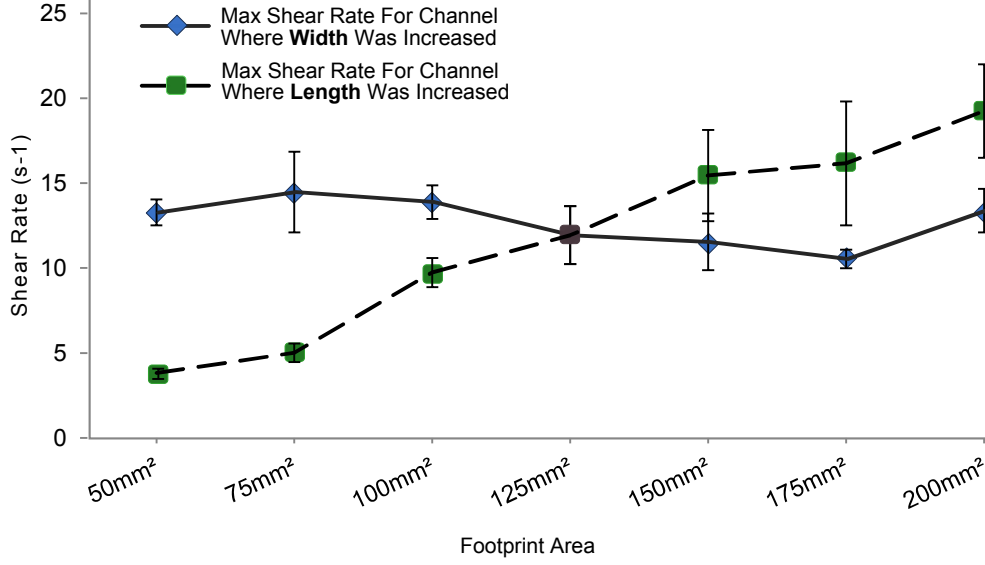


Figure 3.10: The maximum shear rate for the two sets is shown. The max shear rates increase with the increase in length while the shear rate remains constant when the width is increased from 1 to 4 mm.

As the length of the channel was increased the shear rate appreciably increases from $3.8s^{-1}$ to $19.2s^{-1}$. In contrast the shear rate for channels of increasing width alters marginally from $10.5s^{-1}$ to $14.4s^{-1}$. As expected when the channel geometry remains constant the shear rate increased and as the channels width is incremented the shear rate is affected. These results indicate the importance of channel geometry in shear dependent DDF device design and the adaptability of DDF devices for controlling shear rate. For a device requiring a high flow rate and low shear rate an increase in channel width would give the best result, while an increase in the channel length would result in both a high flow and shear rate.

3.4.1 Discussion and Conclusion

When designing devices for shear dependent assays the required shear rate can be maintained through a powered pumping system. While these systems have been in use for some time and are well characterised, size, cost and requirement for tubing make them unsuitable for some point-of-care devices. This chapter introduced a low cost manufacturing technique allowing for the rapid prototyping of degas-driven (self-powered) devices. The experimental results show reproducible flow conditions can be achieved using degas-driven devices, manufactured from pressure sensitive adhesive moulds, allowing for a prototype device to be designed and manufactured at lower cost than traditional methods such as photolithography.

In order to make comparisons the channels listed in Table 3.1 were grouped by footprint area, 6 groups of 2 channels were created. The results clearly showed, a corresponding rise in flow rate through the channel as the area of exposed PDMS was increased. No significant difference in flow rate was observed between channel designs within each of the 6 groups. This finding allows for the design of devices with the ability to control both the flow and shear rate for a defined assay time. Shear is an important design consideration for the development of devices where its control directly affects assay results, such as anti-platelet therapies. The characterisation of flow detailed within this chapter indicates that DDF prototype devices offer great potential for further development and integration of assays where controlling shear rate is a requirement.

Bibliography

- [1] Rosamund Daw and Joshua Finkelstein. Lab on a chip. *Nature*, 442(7101):367–367, July 2006.
- [2] Jose L. Garcia-Cordero and Antonio J. Ricco. *Encyclopedia of Microfluidics and Nanofluidics*. Springer US, Boston, MA, 2008.
- [3] Jamil El-Ali, Peter K Sorger, and Klavs F Jensen. Cells on chips. *Nature*, 442(7101):403–11, July 2006.
- [4] CD Chin, Tassaneewan Laksanasopin, and YK Cheung. Microfluidics-based diagnostics of infectious diseases in the developing world. *Nature Medicine*, 17(8):1015–1019, 2011.
- [5] Paul Yager, Thayne Edwards, Elain Fu, Kristen Helton, Kjell Nelson, Milton R Tam, and Bernhard H Weigl. Microfluidic diagnostic technologies for global public health. *Nature*, 442(7101):412–8, July 2006.
- [6] Alan D Michelson, Verifynow Accumetrics, San Diego, and Plateletworks Helena Laboratories. Methods for the Measurement of Platelet Function. *The American Journal of Cardiology*, 103(3):20A–26A, 2009.
- [7] P Harrison. Platelet function analysis. *Blood Reviews*, 19(2):111–123, March 2005.
- [8] Dongeun Huh, Joong Hwan Bahng, Yibo Ling, Hsien-hung Wei, Oliver D Kripfgans, J Brian Fowlkes, James B Grotberg, and Shuichi

- Takayama. Gravity-driven microfluidic particle sorting device with hydrodynamic separation amplification. *Anal Chem*, 79(4):1369–1376, 2007.
- [9] Nils Goedecke, Jan Eijkel, and Andreas Manz. Evaporation driven pumping for chromatography application. *Lab Chip*, 2(4):219–23, November 2002.
- [10] Glenn M Walker and David J Beebe. A passive pumping method for microfluidic devices. *Lab Chip*, 2(3):131–4, August 2002.
- [11] Kazuo Hosokawa, Masaki Omata, Kae Sato, and Mizuo Maeda. Power-free sequential injection for microchip immunoassay toward point-of-care testing. *Lab Chip*, pages 236–241, 2006.
- [12] David Y Liang, Augusto M Tentori, Ivan K Dimov, and Luke P Lee. Systematic characterization of degas-driven flow for poly(dimethylsiloxane) microfluidic devices. *Biomicrofluidics*, 5(2):024108, June 2011.
- [13] Daniel Irimia, Su-Yang Liu, William G Tharp, Azadeh Samadani, Mehmet Toner, and Mark C Poznansky. Microfluidic system for measuring neutrophil migratory responses to fast switches of chemical gradients. *Lab Chip*, 6(2):191–8, February 2006.
- [14] Ivan K Dimov, Lourdes Basabe-Desmonts, Jose L Garcia-Cordero, Benjamin M Ross, Younggeun Park, Antonio J Ricco, and Luke P Lee. Stand-alone self-powered integrated microfluidic blood analysis system (SIMBAS). *Lab Chip*, 11(5):845–850, 2011.

Chapter 4

Degas-Driven Device Design

The control of shear stress is both a challenge and key goal when developing a new point-of-care platelet function test, as the actuation of fluid flow in a chip with reliable shear rate must be achieved using inexpensive and compact instrumentation [1]. DDF devices are inexpensive and self-powered and do not require an external pump or tubing, making them ideal for use as a point-of-care device. Such a device is presented in this chapter and integrates the Individual Platelet Adhesion (iPA) assay onto a self-actuating microfluidic chip for monitoring platelet adhesion on 6 μm diameter fibrinogen spots. Alterations to geometry of the device to achieve shear rates in the range of 20 – 120 s^{-1} are also documented. Finally the capacity of the device to quantify the effects on the $P2Y_{12}$ platelet receptor when clopidogrel is added *in-vitro* to blood, showing device potential as a point-of-care device for monitoring the effect of anti-platelet therapy in whole blood.

4.1 DDF Shear Results in Whole Blood

An important consideration when designing degas-driven chips is whether the flow rate will fall below the required minimum within the assay time for

a given shear rate. The results from Figure 3.10 shows a maximum shear rate of 20 s^{-1} can be achieved, with the channels listed in Table 3.1 . When considering assays that require fluid volumes in the μL range and a shear rate in excess of 20 s^{-1} a single channel becomes impractical, as the required channel length would be difficult to manufacture and degas.

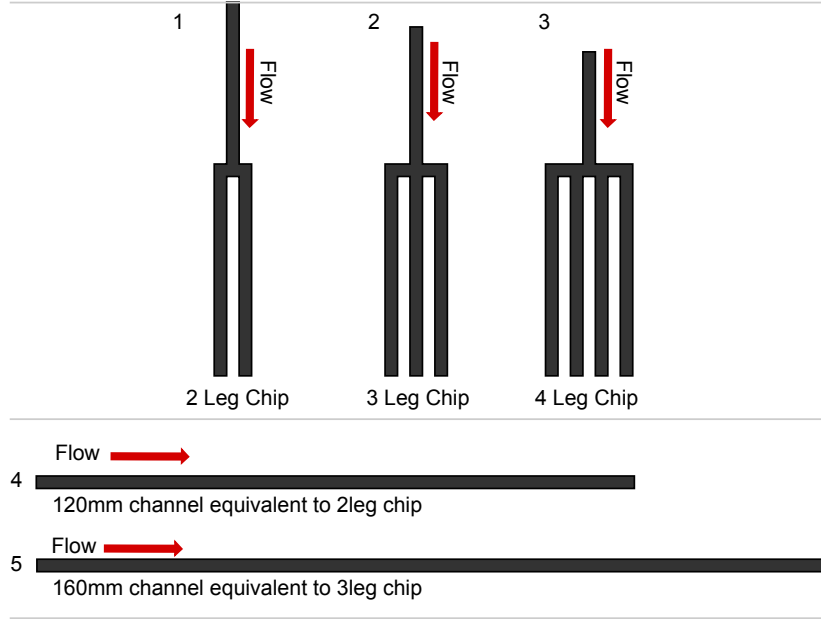


Figure 4.1: A semantic of three devices device designed to compare the shear rate in both water and blood. $n = 4$

Due to the limited size of the desiccator it was not possible to manufacture channels greater than 160 mm in length. This limitation was overcome by splitting the channel and placing these interconnected channels side by side. Figure 4.1 shows channels of 120 mm and 160 mm in length, alongside an equivalent length channel containing the interconnected channels referred to in the figure as legs. Three designs were created with 2, 3 and 4 legs, respectively. The shear rate in water for the 2 leg design ($36 \pm 2.1 \text{ s}^{-1}$) was equivalent to that of the 120 mm single length channel ($38 \pm 1.21 \text{ s}^{-1}$). When the 3 leg channel ($47 \pm 1.8 \text{ s}^{-1}$) was compared to the 160 mm single channel ($46 \pm 1.81 \text{ s}^{-1}$) the same trend was observed. This result indicates

the legs had no effect on the shear rate obtained.

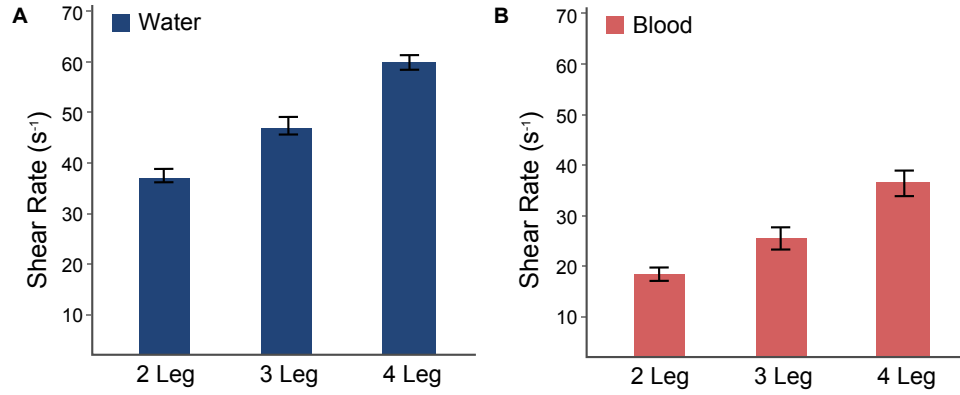


Figure 4.2: A) Shear rate observed in devices containing 2,3 and 4 legs after 7min amount of flow of water. B) Shear rate observed in devices containing 2,3 and 4 legs after 7min amount of flow of blood. $n = 5$ for both water and blood.

As the characterisation of flow within DDF chips was carried out using water, it was important to understand how the transition to blood would affect the flow rate and therefore the shear rate. Figure 4.2 shows the maximum shear rate of the 2 , 3 and 4 leg designs, in both water and blood.

As the characterisation of flow within DDF chips was carried out using water, it was important to understand how the transition to blood would affect the flow rate and therefore the shear rate. While blood plasma is mostly water it is also formed from elements including red cells, white cells and platelets, and proteins such as fibrinogen and albumin. Red cells have the greatest effect on viscosity under normal conditions with blood being about 1.8-times more viscous than water at the same temperature. An Increase in red cell haematocrit leads to a non-linear increase in relative viscosity, with a doubling in haematocrit levels more than doubling relative viscosity [2, 3].

To measure the effect of changing the fluid used from water to blood the maximum obtainable shear rate for the 2 , 3 and 4 leg designs in both water and blood are shown in Figure 4.2 . The viscosity (μ) is not constant

for blood within the channel of the 2, 3 and 4 leg channel as the maximum recorded shear rate was less than 50s^{-1} , given that μ is not constant for blood at shear rates less than 50s^{-1} (detailed in Chapter 2). The 4 leg channel gave the highest shear rate in both water and blood. When the shear rate in water was compared to that of blood for all channels, the observed rate was lower in blood. The results indicate that while the shear rate is lower in blood the addition of legs to any new chip design can make up for the difference in the μ and increase the shear rate so that the μ can be considered constant. The decrease in flow rate (from a maximum) as the channel fills was similar for both blood and water with the maximum shear being obtained for 5 – 10 s. As the length of the channel was increased this slope was more gradual, thereby increasing the bandwidth at which the shear rate is at or near to its maximum.

The addition of legs also has the advantage of reducing the size of any prototype chip. With an understanding of how blood will affect the shear rate, the multi-leg degas chip is ready for integration with an assay that requires a controlled shear rate.

4.2 Design of DDF Devices to Integrate iPA

iPA is detailed in Section 1.3 and uses the adhesion of platelets to $6\text{ }\mu\text{m}$ fibrinogen dots, to detect the adhesion of individual platelets and therefore the percentage platelet adhesion. While iPA has been successfully demonstrated for the monitoring of patients undergoing anti-platelet therapy it has not yet been integrated into a chip [4]

Parallel Plate Flow

In order to rapidly establish if the iPA assay could be adapted for integration into a DDF device a series of parallel plate flow (PPF) experiments were

undertaken over a range of shear rates. The governing principles behind PPF are detailed in Section 2.1.1. To create the required shear rate within the channel a syringe pump was calibrated to insure the flow rate indicated by the pump equalled that of the blood within the PPF chip.

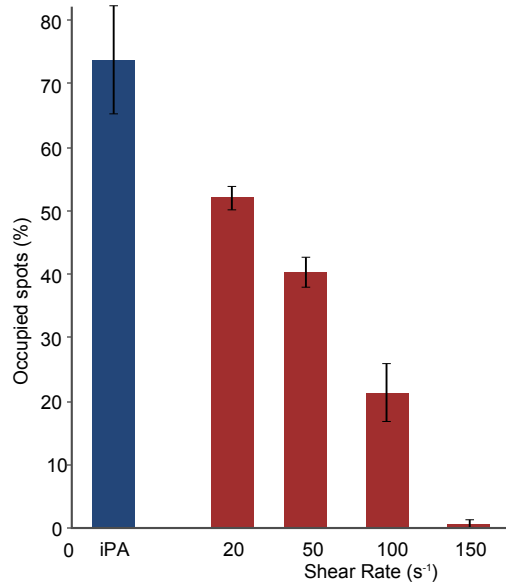


Figure 4.3: The % of occupied spots for 5 mm PPF channel at 20, 50, 100, 150 s^{-1} alongside the results for the iPA assay. $n = 5$

Figure 4.3 shows the resulting % of occupied spots within a 5 mm PPF channel for 10 min where blood was flowed to create a shear rate of 20 s^{-1} , 50 s^{-1} and 100 s^{-1} , results for the iPA assay are also shown. As the shear rate was increased the resulting adhesion decreased from 53 % to 26 % for shear rates between 20 s^{-1} and 100 s^{-1} with 3 % adhesion for a rate of 150 s^{-1} . These results indicate that the DDF device should maintain a shear rate between 20 s^{-1} and 100 s^{-1} for 10 min in order to detect the adhesion of platelets. As the lower shear rate gave a marginally higher % of occupied spots, it was selected when making further comparisons within the PPF channels tested.

The PPF chip utilises a channel length of 42 mm with the 6 μm spots

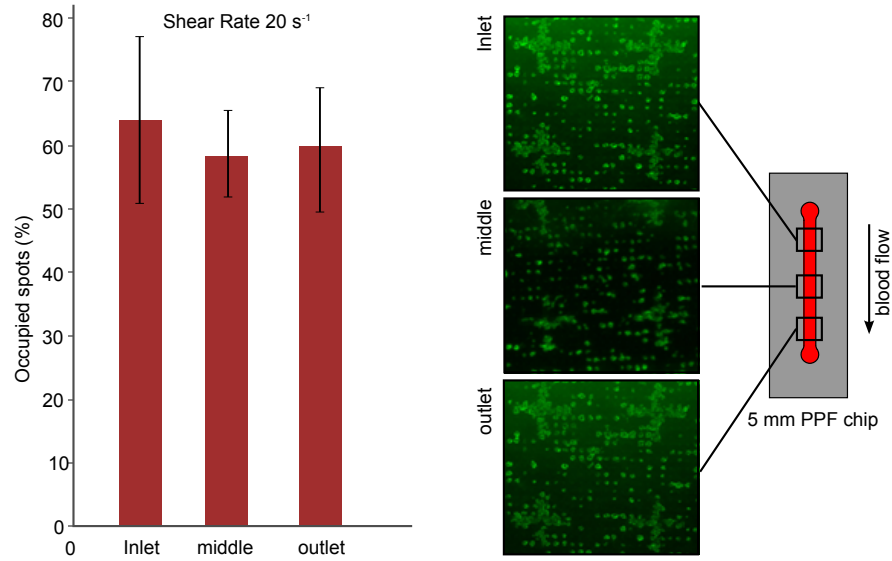


Figure 4.4: The % of occupied spots for 5 mm PPF channel when the array was printed at the inlet, centre and outlet. $n = 7$

printed half way along this channel with a 6 mm inlet and outlet. To determine if the channel inlet or outlet have an effect on platelet adhesion the array was printed at the inlet, middle and outlet. Figure 4.4 shows the resulting % of occupied spots alongside the diagram of the channel and placement of the array. The results show no significant difference across the channel and indicate the full length of the channel can be used to detect the adhesion of platelets.

The effect of changes in channel width on the adhesion of platelets in 6 μm spots are detailed within Figure 4.5-A, for channels of 4, 5, and 6 mm. The results show little difference between % of occupied spots for the 5 or 6 mm channels and low adhesion in channel widths below 4 mm, indicating that platelet adhesion can be affected by channel width. This difference could be as a result of the lower flow rate required to achieve the same shear rate as the width is decreased, thereby resulting in red blood cells settling on the surface of the channel. Figure 4.5-B shows the resulting % for a 5 mm wide PPF channel after 3, 6, 9, 12 and 15 minutes, these results

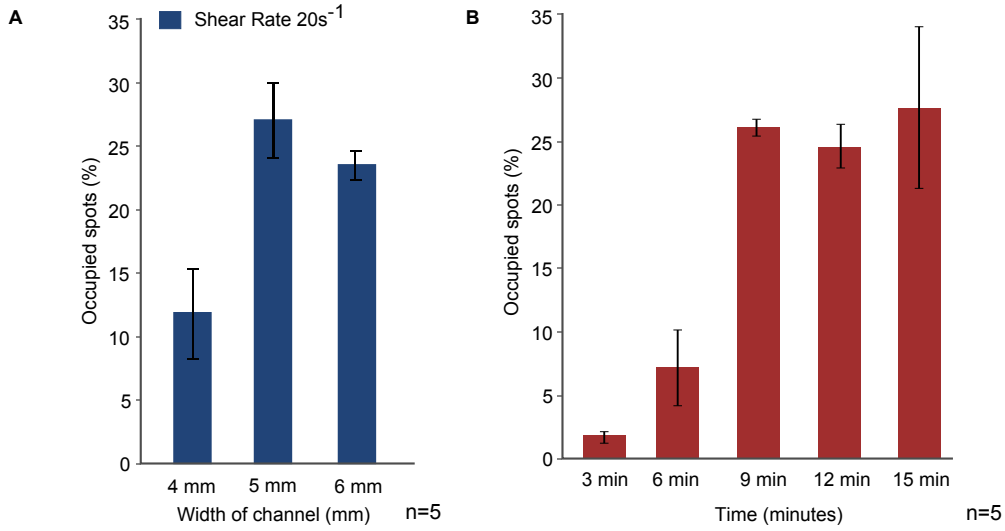


Figure 4.5: Optimisation of conditions in the parallel plate flow devices for platelet adhesion to surface coated $6\ \mu m$ spots of fibrinogen. (A) Adhesion of platelets (% occupied dots) to $6\ \mu m$ dots of fibrinogen measured after 9 mins of blood flow in parallel plate flow device containing channel widths of 4, 5, 6 and 7 mm at a shear rate of $20\ s^{-1}$ ($n = 5$). (B) Time-dependent adhesion of platelets (% occupied dots) to $6\ \mu m$ dots of fibrinogen using 6 mm wide channel at a shear rate of $20\ s^{-1}$ ($n = 5$).

show a plateau in the % platelet adhesion occurred after 9 minutes. Five PPF chips for each of the three widths were tested ($n = 5$) at $20s^{-1}$ and five chips at each of the different time intervals ($n = 5$).

PPF has successfully shown a single platelet can adhere to the $6\ \mu m$ spot used within the iPA assay. Using the result obtained when testing PPF a starting point for the design of a DDF channel should include a shear rate between $20\ s^{-1}$ and $100\ s^{-1}$, a channel width no less than 5 mm and a flow time greater than 6 minutes.

Chip Design

Figure 4.1 demonstrated how the shear rate within a DDF device could be increased with the addition of legs to a straight channel. With this in mind, a series of multi-leg DDF devices were designed to investigate if the parameters established during the testing of the straight channel PPF device

could be matched. The DDF chip designs were divided into two areas, a test area and pumping area. The test area contains the assay region and starts at the inlet, before connecting with the pumping area. By adding more legs within the pumping area the available area of exposed PDMS is increased, resulting in an increased shear rate across the assay region. The assay region contains the array of $6\ \mu\text{m}$ spots. Figure 4.6 shows the final prototype devices tested, consisting of a 6 mm wide test region with 1, 2, 3, 6, 7 and 9 legs to make up the pumping area.

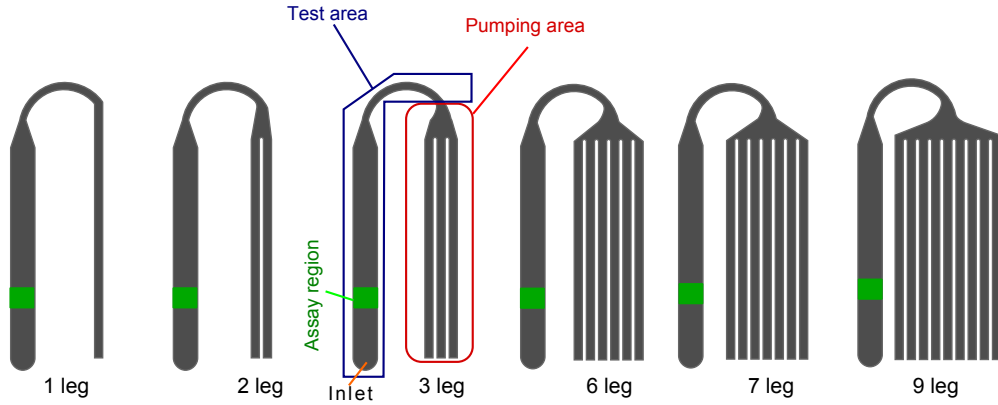


Figure 4.6: 2-D representation of the six channel designs created with 1, 2, 3, 6, 7 and 9 legs each of 2 mm width. The green square shows the location of the $6\ \mu\text{m}$ spot array, along the 6 mm width test area. The array contains 24336 spots made up of 144 blocks of 13×13 spots.

The test area was placed at the side of the chip to reduce chip size and better match the channel length used in parallel plate flow. The length of the channel also reduced any impact upstream changes in flow, caused by the curved section, may have on the resulting platelet adhesion. Each leg was increased from 1 mm to 2 mm in width to ease manufacture and simplify the design. When whole blood was added to the 1, 2 and 3 leg chips the blood flow was slow, resulting in separation of the blood into red blood cells and plasma. The DDF chip consisting of 9 legs was found to allow the blood to flow without separating. The volume of blood loaded onto the

chip was increased from $100\ \mu\text{l}$ to $200\ \mu\text{l}$ to ensure that a sufficient volume of blood passed over the μ -contact printed fibrinogen surface, during the 9 minute assay time.

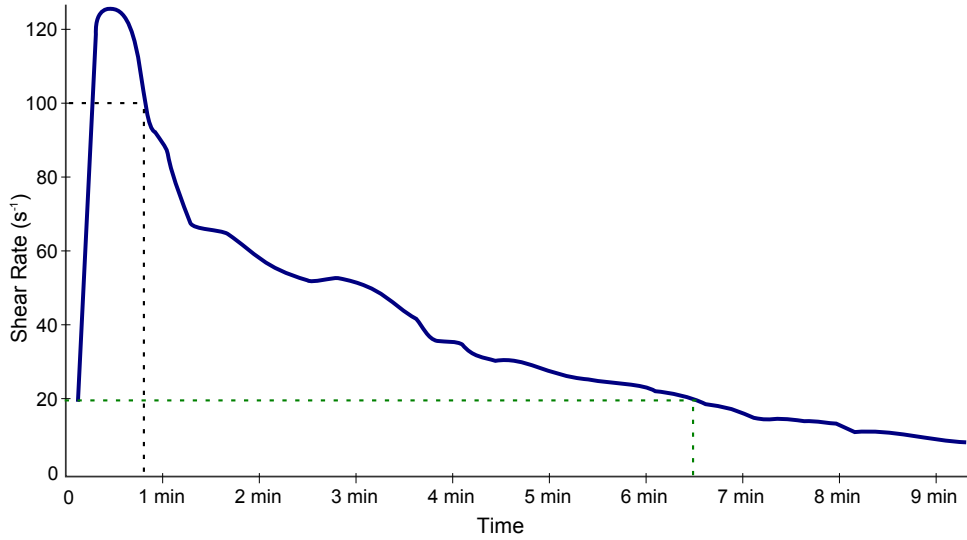


Figure 4.7: Shear rate profile for 9 leg device. The shear rate decreases from a high of approximately $120\ \text{s}^{-1}$ to $10\ \text{s}^{-1}$ after 8 minutes. The shear rate stays between $100\ \text{s}^{-1}$ and $20\ \text{s}^{-1}$ for 5 minutes which is between the range of shear rates determined with the use of parallel plate flow for adhesion of platelets to $6\ \mu\text{m}$ spots. $n = 7$

After evaluation of the PPF designs the % platelet adhesion (60%) for the 6mm by 9 leg was equivalent to the maximum achieved within parallel plate flow (65%). The flow characteristics differ between the PPF and DDF devices, with the shear rate of the DDF device decreasing (from a maximum) over time while the shear rate remains constant within a parallel plate flow device (controlled by a syringe pump). Figure 4.7 shows the DDF shear rate profile for the 9 leg channel recorded over 9 minutes, shear rates ranging from approximately $20\ \text{s}^{-1}$ to $100\ \text{s}^{-1}$ are highlighted. The PPF chip required a flow time greater than 6 minutes for the same range of shear rates, while the PPF maintained this rate for approximately 5 minutes, and $10\ \text{s}^{-1}$ to $100\ \text{s}^{-1}$ for 8 minutes. The difference in the time required for an equivalent result in platelet adhesion could be as a result of the different

flow characteristics between PPF and DDF flow. The maximum shear rate of 120 s^{-1} is achieved during the first 60 seconds of flow and closely match those obtained from PPF devices. When the channel width (test area) was decreased from 6 mm to 2 mm no platelet adhesion was observed, given that the shear rate is the same for both channels this result indicates that the channel width (at the test region) for both PPF and DDF devices affect how platelets adhere to 10 μm fibrinogen dots.

4.2.1 Effect of Anti-platelet Drugs Use of iPA

The 9 leg second generation device has successfully been used to measure platelet adhesion in whole blood from healthy donors but to-date the use of DDF for the determination of platelet adhesion in patient samples remains unproven. To determine if this design is suitable for use as a prototype device for the testing of anti-platelet therapies, platelet reactivity was tested in both the presence and absence of Cangrelor (added *in-vitro* to whole blood). Adenosine diphosphate (ADP) was used as an agonist in this assay as it induces aggregation in whole blood through the activation of $P2Y_1$ and $P2Y_{12}$ receptors. Cangrelor inhibits the $P2Y_{12}$ pathway of activation and therefore hinders ADP induced aggregation of platelets. Figure 4.8 shows results for untreated and treated blood allowed to flow in the DDF device for 9 minutes, after which the % adhesion was calculated. As expected, the percentage of platelet adhesion was significantly decreased when the blood was treated with ADP resulting in a 7% occupancy when compared to the untreated whole blood at 59%. This effect was almost completely negated after the addition of Cangrelor to the ADP treated blood resulting in a 50% adhesion. Aggregates do not stick to the 6 μm fibrinogen dots patterned within the test region (when the blood is ADP treated) but instead out compete the fibrinogen spots on the surface for any single platelets remain-

ing within the blood, resulting in a decrease in % platelet adhesion. This effect is reversed if aggregation is hindered by the anti-platelet drug in this case Cangrelor. This DDF design is therefore ideal as a prototype rapid self-powered device, with enormous potential for use in the point-of-care assessment of platelet reactivity during anti-platelet therapy.

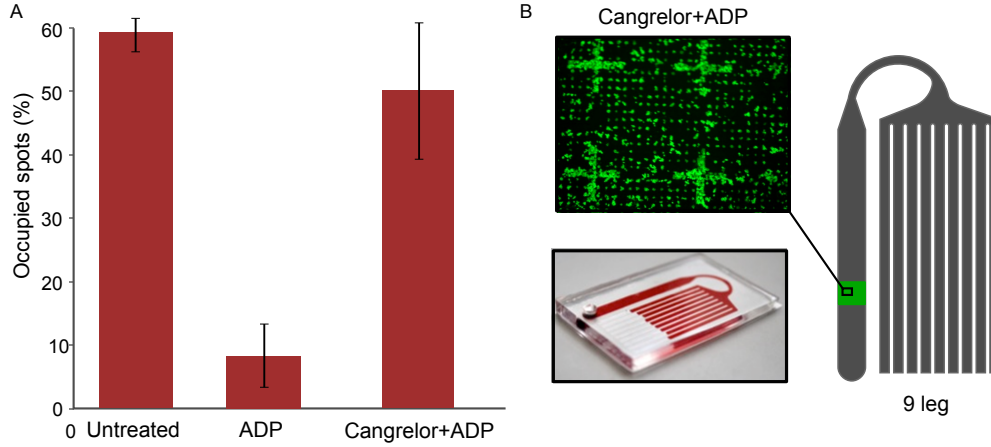


Figure 4.8: (A) Detection of *in-vitro* $P2Y_{12}$ inhibition using DDF device. Platelet adhesion to fibrinogen dots (% occupied spots) in 3 separate blood draws on separate days for a single healthy donor with no agonists with $20 \mu M$ ADP, and with $20 \mu M$ ADP in the presence of $10 \mu M$ cangrelor, which effectively abrogates the ADP effect, demonstrating detection of $P2Y_{12}$ inhibition. Error bars represent standard deviations for the 3 separate blood draws. (B) Photos of the chip during flow and a picture of platelets adhered to the spots used to calculate the % adhesion are shown in Figure 4.8-B.

4.2.2 Discussion of Results

The ability to control flow rate, and therefore shear rate, within a single channel, was well documented within Chapter 3. Although this flow is non-linear over time the self-powered and low cost nature of DDF devices render them ideal for use in a limited resource environment. By successfully demonstrating the iPA assay the device design offers a prototype with enormous potential for use as a point-of-care assessment device in 9 minutes. The operation and cost of the 9-leg prototype device compares well when matched

against light-transmission platelet aggregometry, which requires the blood to be centrifuged to produce the platelet poor plasma (PPP) and platelet rich plasma (PRP) required. While the VerifyNow works in whole blood it has not yet been proven an effective test for use with anti-platelet therapies, with two large scale studies reporting no significant improvement in clinical outcomes [5, 6]. The increased complexity of the channels required a different approach when removing the PSA channel from the backing sheet and as a result many of the first attempts failed to seal with the substrate or blood leaked around the inlet.

As a means of rapidly determining if single platelets would adhere to $6\ \mu m$ spots a number of different flow rates and shear rates were tested with the use of a parallel plate flow (PPF) channel. The flow rate, shear rate and volume of blood can be controlled through changes in channel geometry and PPF also removed any effects of the decreasing flow rate, and thus shear rate, seen in DDF devices. The PPF results indicated a $6mm$ channel at a shear rate of between $20\ s^{-1}$ and $100\ s^{-1}$ would give the best results. This result differs with data published by Hansen *et al.* in which it is stated that a spot size of greater than $20\ \mu m$ was necessary to support stable platelet adhesion at a wall shear rate of $300\ s^{-1}$ [7]. This difference may be accounted for by the channel size used within the study of only $250\ \mu m$ or the assay time of 5 minutes.

The device was used to successfully detect the inhibition of platelets in blood treated with Cangrelor in the presence of ADP and correlates well with the results published by Lopez-Alonso [4], these results were obtained using the iPA assay and also expressed in terms of % of occupied spots. The DDF result also shows the enormous potential of the device to be developed as part of a point-of-care system for the assessment of platelet reactivity during anti-platelet therapy. At present no other self-powered device has been shown to detect the inhibition of platelets. While the device was

demonstrated with anti-platelet therapies it could be readily adapted for use with other platelet assays that require a simple way to count platelets, in remote locations or limited resource environments, such as the developing world. By changing channel geometry it is possible to create a device with a defined upper and lower shear rate range. These devices may have a use within a shear dependent assay outside an area concerned with platelets.

4.2.3 Conclusions

A novel micro-fluidic device was developed for the assessment of platelet reactivity during anti-platelet therapy. This device has many desirable attributes required in a point-of-care device including portability, ease of use, speed, low cost, self-powered and low blood volume requirements. DDF devices do not require an external pump to drive blood flow through the micro-fluidic channel, resulting in a hand held compact device which could be used in a clinical setting. A simpler system design is possible as DDF does not require an external power supply. The use of poly(cycloolefin) sheets enabled leakage-free blood flow and a smooth blood flow was observed even at low shear rates, such as 20 s^{-1} for 10 minutes, which is challenging using a syringe pump. Although, adhesion of platelets to $6\text{ }\mu\text{m}$ fibrinogen spots is dependent on the shear rate of the blood flow in DDF chips, test channel width also had a crucial impact on platelet adhesion. The challenge of controlling the shear rate in DDF was successfully surmounted by changing the cross-sectional area of the pumping region and high platelet adhesion was achieved for the chips with large pumping areas. This DDF device for whole blood assays points the way toward a new approach for lab-on-a-chip research as well as point-of-care and high-throughput screening systems for platelet adhesion studies. This device has the potential to facilitate the personalisation of antiplatelet therapy particularly for patients with cardio-

vascular diseases and thus reduce the risk of thrombosis or bleeding in these patients. However, like the VerifyNow cartridge the prototype DDF chip is limited to a single agonist. With many individuals on dual anti-platelet therapy the prototype can only test the effect of one of these anti-platelet drugs. With this in mind an alternative chip was developed, based on the rocking table currently used within the iPA assay. This chip allows for multi agonists to be tested at the same time and is detailed in the next chapter.

Bibliography

- [1] Curtis D Chin, Vincent Linder, and Samuel K Sia. Lab-on-a-chip devices for global health: past studies and future opportunities. *Lab Chip*, 7(1):41–57, 2007.
- [2] Oguz K. Baskurt. *Handbook of Hemorheology and Hemodynamics*. IOS Press, 2007.
- [3] Richard Klabunde. *Cardiovascular Physiology Concepts*, volume 3. Lippincott Williams & Wilkins, 2011.
- [4] Dermot Kenny Ana Lopez-Alonso, Bincy Jose, Martin Sommers, Karl Egan, David P. Foley, Antonio J. Ricco, Sofia Ramstrom, Lourdes Basabe-Desmonts. Individual Platelet Adhesion (iPA) Assay: Measuring Platelet Function and Anti-Platelet Therapies in Whole Blood via Digital Quantification of Cell Adhesion. *Analytical Chemistry*, 85(13):6497–6504, 2013.
- [5] Matthew J Price, Dominick J Angiolillo, Christopher P Cannon, and Eric J Topol. Platelet reactivity and cardiovascular outcomes after percutaneous coronary intervention: a time-dependent analysis of the Gauging Responsiveness with a VerifyNow P2Y12 assay: Impact on Thrombosis and Safety (GRAVITAS) trial. *Circulation*, 124(10):1132–7, September 2011.

- [6] Christophe Pouillot, Patrick Henry, D Ph, Pascal Motreff, Eric Van Belle, Hélène Rousseau, Pierre Aubry, Jacques Monségu, Pierre Sabouret, Stephen A O Connor, B Ch, Jérémie Abtan, Mathieu Kerneis, Christophe Saint-etienne, Olivier Barthélémy, Farzin Beygui, Johanne Silvain, Jean-Philippe Collet, Thomas Cuisset, Eric Vicaud, and Gilles Montalescot. Bedside monitoring to adjust antiplatelet therapy for coronary stenting. *The New England Journal of Medicine*, 367(22):2100–9, November 2012.

- [7] Ryan R Hansen, Adam R Wufsus, Steven T Barton, Abimbola a Onasoga, Rebecca M Johnson-Paben, and Keith B Neeves. High content evaluation of shear dependent platelet function in a microfluidic flow assay. *Annals of Biomedical Engineering*, 41(2):250–62, February 2013.

Chapter 5

Integration of an iPA assay into a Prototype Device for Point-of-Care

5.1 Introduction

In the previous chapter, the iPA assay (described in Section 1.3) was successfully combined with a degas-driven flow (DDF) prototype to create a self-powered, low-cost and easy-to-manufacture chip. The iPA assay has been shown by Lopez-Alonso *et. al.* to correlate well with both Light Transmission Aggregometry (LTA) and the VerifyNow system [1]. LTA is detailed in 1.2 and requires a whole blood sample to be processed to create platelet rich plasma (PRP) and platelet poor plasma (PPP). Both the iPA and DDF chip are unsuited for use as part of an integrated point-of-care (POC) device as they require a number of manual blood handling and washing steps. The iPA assay requires the slide to be placed into a petri-dish before 1 *ml* of blood is added and the dish is rocked for 30 minutes. The slide must be removed from the dish and the platelets washed and stained

before imaging. For the iPA assay to be part of any prototype device, these manual steps will need to be automated or removed in order to reduce the risk to the operator when working with blood.

This chapter details the development of two new chip designs and introduces a chip optimised version of the current iPA assay (COiPA). The first design is intended for research use and still requires the blood to be manually pipetted into each well, while the second design integrates a standard blood handling system and can be used as part of a prototype point-of-care device. These new designs allow for multiple anti-platelet drugs to be investigated on a single chip, giving the new design an advantage over the DDF prototype, VerifyNow system and LTA.

5.2 Optimisation of the iPA Assay

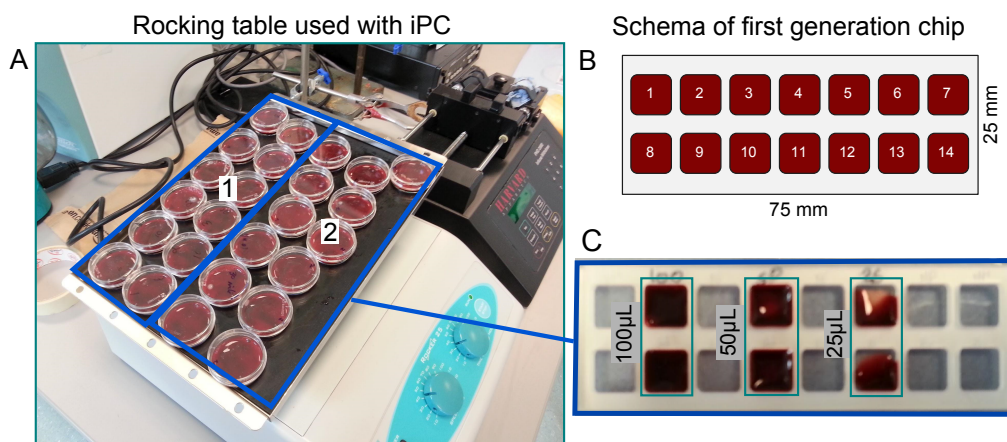


Figure 5.1: Open square well chip compared with current assay. (A) The seesaw rocking table used in the current iPA assay can hold 25 samples, the equivalent to only two square-well chips. (B) The chip fits on a standard glass slide chip and contains 14 or 16 wells in two rows of 7 and 8, respectively. (C) A 16 well chip filled with 25, 50 and 100 μl of blood shows how 25 μl fails to cover the surface of the well and 100 μl fills the well completely, thereby preventing the blood from moving over the surface.

The chip was developed to fit a standard microscope slide measuring $75\text{ mm} \times 25\text{ mm}$, thereby replacing the $20 \times 20\text{ mm}$ cover slip used within the iPA assay. This change allowed 14 samples to be assayed on a single chip with 2×7 wells measuring $9 \times 9\text{ mm}$. This well size was chosen to fit the stamp used to μ -contact print the array of $6\text{ }\mu\text{m}$ spots onto the slide and left some free space around the edge to allow for any alignment error during printing. The wells were cut into a transparent thermoplastic sheet of 2.5 mm Poly(methyl methacrylate) (PMMA) with the use of a laser cutter. A pressure sensitive adhesive (PSA) gasket was then adhered to one side of the PMMA before final assembly of the well layer and the glass substrate. Figure 5.1-A shows the rocking table with 24 petri-dish, each dish contained a single cover slide submerged in 1 ml of blood. A single test can be carried out with each cover slide and is equivalent to a single well within the chip.

Optimisation of Blood Volume and Rocking Speed

When the results for both the 14 well chip and petri dish were compared a lower % adhesion to the spots of fibrinogen was observed for the chip. Given that the blood volume and rocking speed for the iPA assay has already been optimised (for a petri dish) it was necessary to determine if these values were optimal for use with the 14 well chip. A range of volumes from 25 to $100\text{ }\mu\text{l}$ were selected with the results shown in Figure 5.2-A, each well holds a maximum of $100\text{ }\mu\text{l}$. Once the blood volume was determined the chip was rocked at a series of different rocking speeds with the results shown in Figure 5.2-B.

Out of the five different volumes of blood tested the highest % platelet occupancy was recorded for $50\text{ }\mu\text{l}$ at 78%. For volumes of 60, 80 and $100\text{ }\mu\text{l}$ the value decreased from 68 to 30%, while the % platelet occupancy for $25\text{ }\mu\text{l}$

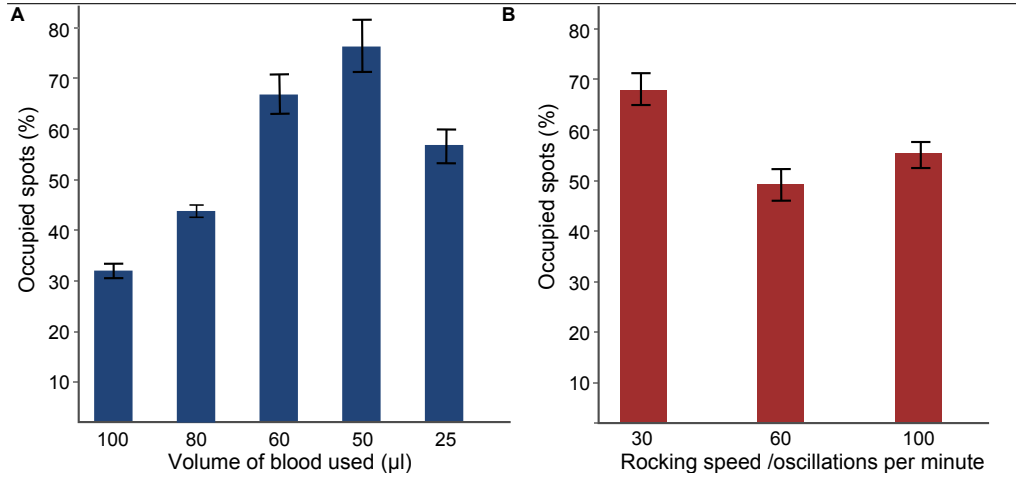


Figure 5.2: Optimisation of chip. (A) Five different volumes of blood were tested from 100 to 25 μl within the well of the chip and the % platelet adhesion recorded for each volume, with the highest achieved at 50 μl . (B) With the volume optimised the effect of rocking speed on platelet adhesion was tested at 30, 60 and 100 oscillations per minute with 50 μl of blood.

was 57%. The bottom well surface was not fully covered with blood when rocked with volumes less than 50 μl . The reduction in % platelet occupancy for volumes greater than 50 μl could be a result of how the blood flowed within the well as the table rocked. The difference in area of the square well and the area for the petri dish used in iPA (962 mm^2) could affect how blood flows over the surface. Figure 5.2-A indicates that the volume of blood plays a role in adhesion. The speed of rocking was optimised with each well filled with 50 μl of blood. Figure 5.2-B shows the results after the chip was rocked for 30 minutes at 30, 60, and 100 oscillations per minute. The results indicate the optimum speed is 30 oscillations per minute. This result compares well with the results published by Lopez-Alonso et al. who found an optimum speed of 35 oscillations per minute over 30 minutes.

To differentiate the now optimised assay from Individual Platelet Adhesion (iPA) it was given the acronym COiPA (Chip Optimised Individual Platelet Adhesion). The COiPA assay was combined with a cyclo olefin polymer (COP) substrate and tested to determine if this grouping was suit-

able for use as a prototype device for testing antiplatelet therapies. A comparison between COP and glass is detailed in Appendix E and shows a comparable level of platelet adhesion. The COP substrate was selected as it has a number of advantages over the glass substrate currently used, its low cost, availability in any size, ability to be cut to shape and optical properties make it ideal for use in a point-of-care chip.

COiPA Tested With $P2Y_{12}$ Inhibitor

The COiPA assay allows for the capture of single platelets onto an array of fibrinogen spots and is derived from the iPA assay detailed in Section 1.3. To demonstrate an *in-vitro* drug effect using COiPA the agonist, adenosine diphosphate (ADP) was used; this receptor acts on the $P2Y_{12}$ platelet receptor, (a list of platelet receptors is listed within Appendix A). The antiplatelet drug Cangrelor can reverse the effect of the agonist by inhibiting the $P2Y_{12}$ pathway and therefore hinders ADP-induced aggregation of platelets. The addition of ADP will result in a decrease in % platelet occupancy, when compared to untreated blood, as aggregates do not stick to the fibrinogen array with only a single platelet captured by each $6\mu m$ spot [1]. Figure 5.3 shows the resulting % platelet occupancy for an untreated sample of whole blood, whole blood treated with ADP and whole blood treated with ADP + Cangrelor.

As expected the percentage of platelet adhesion was significantly decreased for a ADP treated blood sample (15%) when compared to the untreated whole blood at 73%. This effect was almost completely negated after the addition of Cangrelor to the ADP treated blood, resulting in a 59% occupancy. COiPA shows the same trend when Cangrelor and ADP was tested within the DDF prototype device, detailed in Figure 4.8 . Both the COiPA and DDF devices require $50\mu l$ of whole blood. These results show

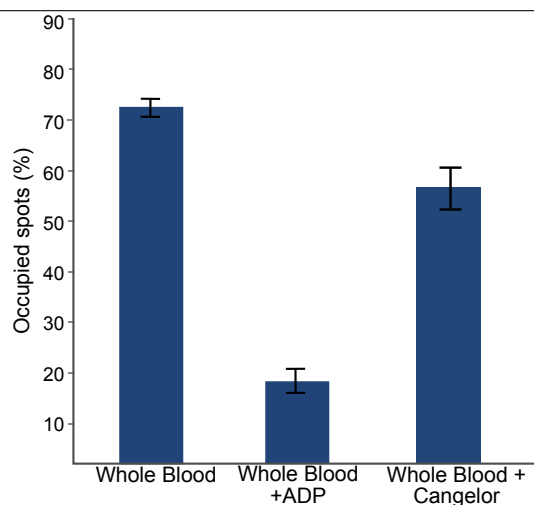


Figure 5.3: Detection of *in-vitro* $P2Y_{12}$ inhibition using square wells ($50 \mu\text{l}$ of whole blood per well). Platelet adhesion to fibrinogen dots (% occupied spots). The three columns show the result for untreated whole blood, blood treated with an agonist ($20 \mu\text{M}$ ADP), and ADP in the presence of $10 \mu\text{M}$ Cangrelor (which effectively abrogates the ADP effect). This is the same agonist and drug shown in Figure 4.8.

that the multi-well chip can detect $P2Y_{12}$ inhibition, with a smaller blood volume on a single chip when compared to iPA which requires 1 ml per assay.

Effect of Flow Length on % of Occupied Spots

During the testing of the multi-well chip a lower % adhesion was observed when compared to the petri dish used within the iPA assay. This result indicated that flow length or well shape may play a role in platelet adhesion and would need to be optimised. The flow length is defined as the distance the blood can move from one boundary to the next which in the case of a petri dish (as a cylinder) remains fixed, despite its rotation when placed on a seesaw rocking table. The flow length of the well (square in shape) is dependent on the rotation of the multi-well chip, relative to the axis of movement of the rocking table. To evaluate if flow length had any effect on platelet adhesion, chips were placed at both the centre and edge of the

rocker at an angle of 0° and 45° .

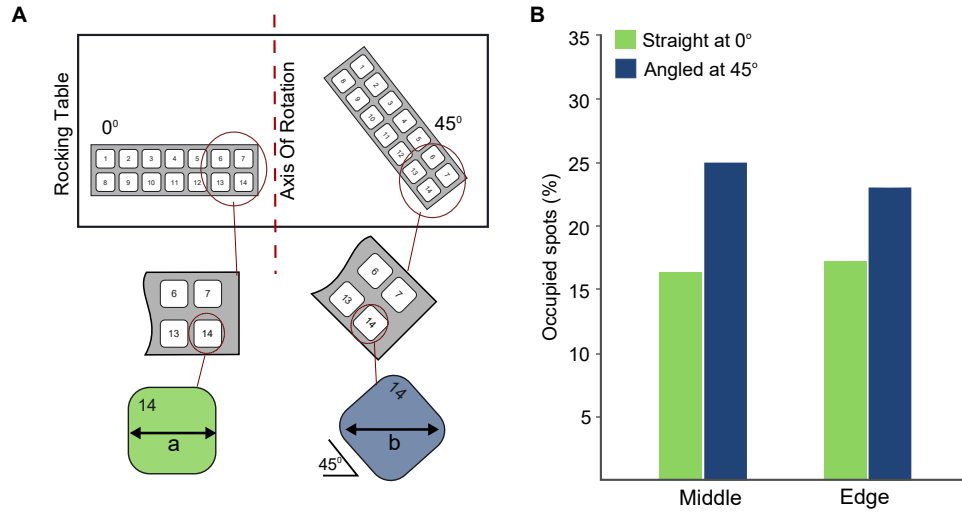


Figure 5.4: Effects on % platelet adhesion as a result of changes to flow length. (A) The square well at both 0° and 45° and the difference in flow length. (B) Effects on % platelet adhesion for a square well placed at both the middle and edge of the table, at an angle of 0° and 45° .

Figure 5.4-A illustrates how the rotation of the square well affects the length the blood can flow. When the chip is rotated by 0° the flow length (a) is at a minimum and at 45° the flow length (b) is at its maximum. The rocking table moves about a single axis of rotation from its centre and as a result the blood only moves perpendicular to this axis within the bounds of the assay well or petri dish.

Figure 5.4-B shows the % adhesion for wells at an angle of 45° and 0° , placed at both the centre and edge of the rocking table. The results show no significant difference in the % adhesion between placing the chip at the edge or centre of the rocking table, indicating the placement of the chip has no effect and as expected is in line with the iPA assay where the whole table is used. There is an increase in the % on occupied spots recorded between the chips placed at 45° and those placed at 0° . The flow length for a straight well (0°) is 7.3 mm and 9.6 mm for the well at 45° , a maximum difference of

only 2.3 mm, indicating that flow length is an important design component and required optimisation.

COiPA Within A Closed Well

For the chip to be used in a clinical environment, it must be safe to use. The current iPA assay uses an open petri dish, requiring manual blood handling. COiPA reduced the blood volume need but still requires the same number of manual blood handling steps, when used with an open well configuration. For COiPA to be used within a point-of-care device the chip must be sealed to reduce any possible contact between the operator and the blood. To address this challenge both an open and closed chip were tested with the same volumes of blood.

Unlike the open chip, the blood is closed within the well and cannot move from side to side with the same ease. To test the effect blood volume has within a closed chip a cover plate was placed over the chip and a hole was positioned above each well, allowing a different volume to be added to each well.

Figure 5.5 shows the resulting % occupancy when two different volumes of blood are added to both an open and closed well. For a volume of 50 μl there is no significant difference between the two well configurations. However, when 110 μl (completely full) of blood was pipetted into each well type and rocked a decreased adhesion of 45% and 0% were recorded for the open and closed wells, respectively. These results indicate the volume has an effect on the resulting adhesion and the assay requires the upper surface of the blood to be able to move freely. Therefore, any closed chip will require a method to deliver a controlled volume to each well.

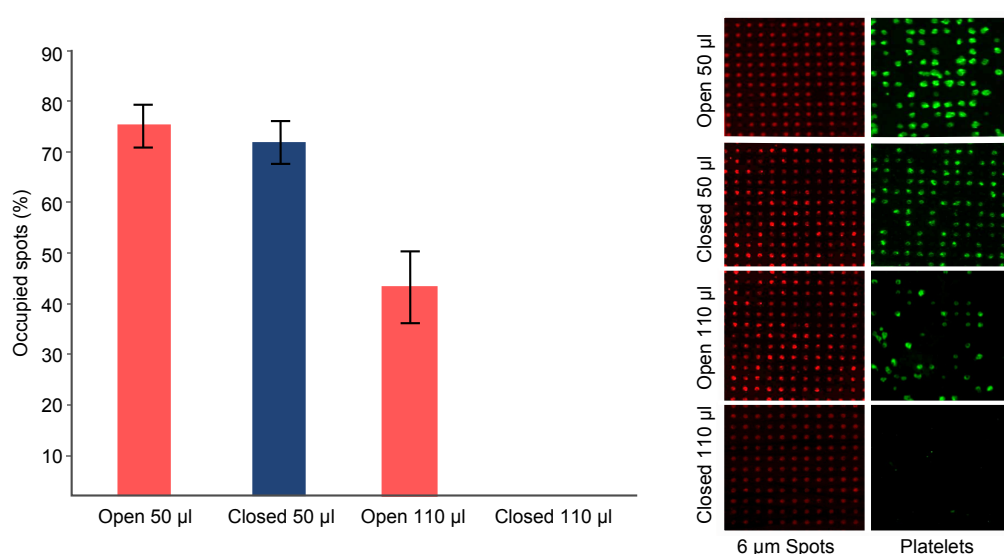


Figure 5.5: Comparison between open and closed chips. The assay wells of both the open and closed versions of the chip were loaded with 50 μ l and 110 μ l of blood and the % of occupied spots recorded. The corresponding images of the protein spots and the platelets adhered to these spots are also shown.

5.3 Prototype Design

The results obtained for the multi-well chip highlighted a number of key design components that would need to be optimised for any new prototype point-of-care device. Different well shapes were tested to increase the % platelet adhesion of COiPA, to better match the iPA assay. Different systems were also tested to allow a fixed volume of blood to be delivered to each well (detailed in Appendix E).

Optimisation of Well Shape

A series of well designs were evaluated to determine the best shape required to maximise platelet adhesion when using COiPA. The effect of the height of blood within the well, as the table rocked, was also investigated and is detailed in Appendix E.

In total five different well shapes were evaluated, four of the same ca-

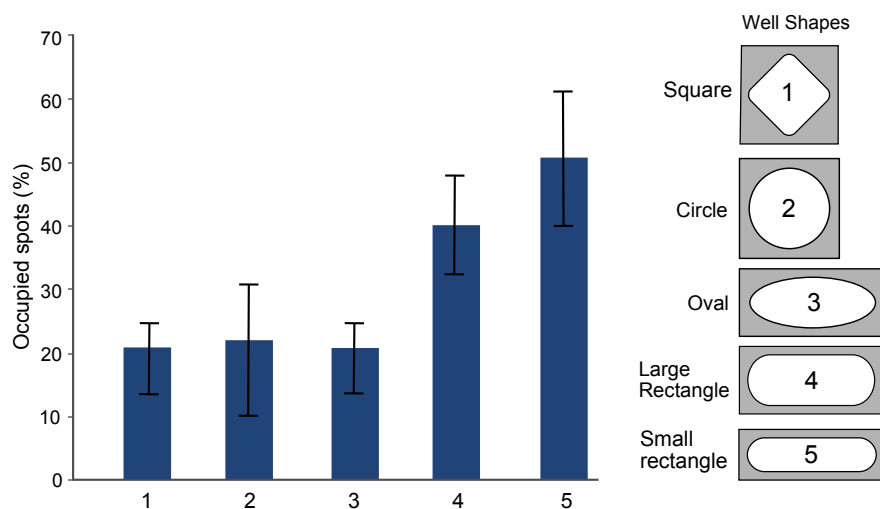


Figure 5.6: Effects of channel shape on platelet adhesion. Five different shaped wells were tested each with different flow lengths, results shown are for wells at their maximum flow length. The maximum % platelet adhesion was recorded for the small rectangle. One of each well type (numbered 1-5) was tested using the same whole blood sample, this was repeated five times ($n=5$) with a total of 25 chips tested

capacity and one larger capacity rectangle. Figure 5.6 shows results and illustrations for each well type starting with the square used with the multi well chip alongside a circle, oval and small rectangle. The larger capacity well has the same flow length and maximum width and was included as a well shape to make a comparison between wells of equal flow length and a well with the maximum width equal to that of the oval. A 60% occupancy of the $6\ \mu m$ spots was recorded for the small rounded rectangle, over twice that recorded with the square well. The results also show no difference between the oval, circle and square wells with both the rectangular wells performing significantly better, with the lower capacity well giving the best outcome. Well shape 5 (shown in Figure 5.6) gave the highest resulting adhesion of the five shapes tested and was therefore selected for further optimisation..

Rectangular Well Optimisation

To determine the effect on the % of occupied spots when the well (well type 5) is closed, a lid was added to the chip. A range of blood volumes from $50\ \mu\text{l}$ to $100\ \mu\text{l}$ was tested in both the presence and absence of the lid.

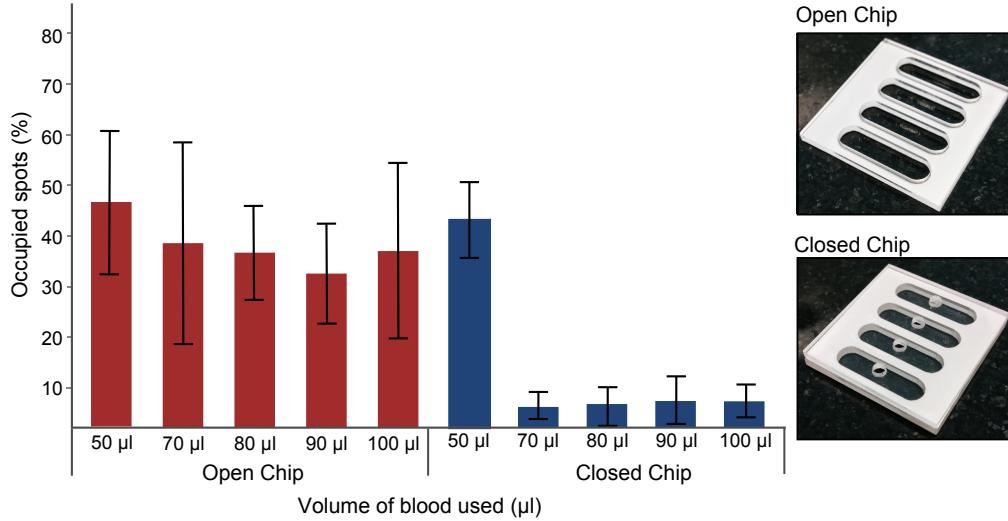


Figure 5.7: Optimisation of blood volume within rectangular well. Four different volumes of blood were tested from $70\ \mu\text{l}$ to $100\ \mu\text{l}$ in increments of $10\ \mu\text{l}$ for both an open and closed well. No statistical difference in the % of occupied spots was recorded for the open well.

Figure 5.7 shows no statistical difference between volumes from $50\ \mu\text{l}$ to $100\ \mu\text{l}$ for the open well. When the closed well is considered the % of occupied spots is approximately 10 % for volumes greater than $70\ \mu\text{l}$ within the closed chip. This result shows that blood volume is of greater importance when designing a chip with a closed well configuration.

When the % of occupied spots between well type 5 and the iPA assay was compared a reduction in adhesion of platelets within the well was observed. To address this difference the flow length of the well was increased to match that of the petri dish. Figure 5.8 shows the two well types used alongside a comparison of the % of occupied spots between the iPA assay and COiPA, well type 6 has double the flow length of well type 5. The results show a

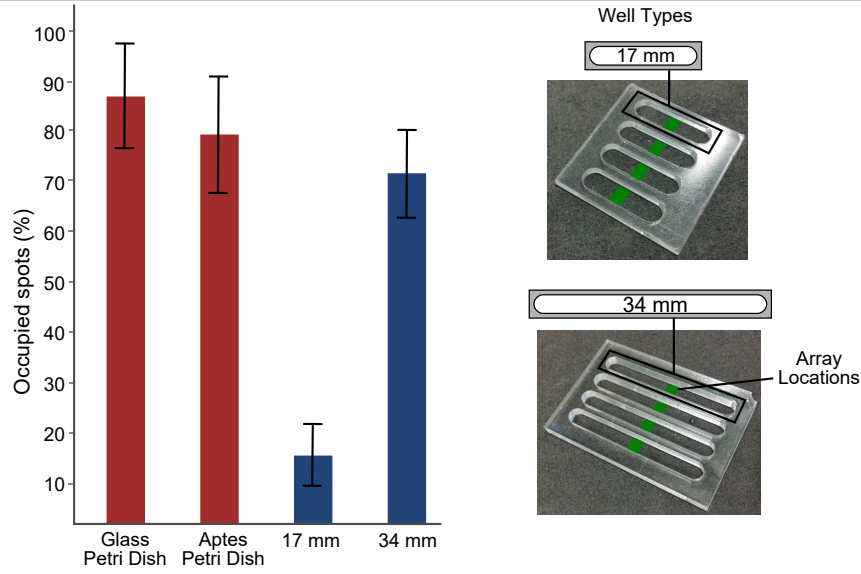


Figure 5.8: Optimisation of flow length. A channel with the same flow length as the petri dish (38 mm) is compared alongside a glass slide and APTES treated Zeonor (shown in red). The 17 mm (Well 5) long channel is the same as that shown in Figure 5.8.

comparable % of occupied spots between well type 6 (75%), and the iPA assay using a glass substrate (88%) and APTES treated Zeonor substrate (79%). The results show that by matching the flow length COiPA with that of the iPA assay that well type 6 offered a comparable assay with a reduced blood volume within a smaller form factor, making it ideal for use within the two prototype chips described below. The ability to use the COiPA assay in the closed well configuration allows for an integrated blood handling system to be included in the chip design.

5.3.1 Research Chip

Blood handling is an important consideration when designing a new prototype device and requires all wells within the chip to be closed. For this reason both prototype chips are only available in the closed well configuration and utilise the optimised well design. The first prototype, known as

the research variant, allows for *in-vitro* testing of multiple drugs within a single chip and is available with 4, 8 and 12 wells. The second prototype integrates a blood handling system and allows for a fixed volume of blood to be delivered from a staging well to each assay well at the same time

Optimisation of Blood Volume in Research Chip

The difference between the open and closed well designs was overcome by increasing the well height from 2.5 mm to 6.0 mm; this allows the blood to flow freely from one end of the channel to the other. When smaller volumes of blood ($< 50 \mu\text{l}$) were rocked within well type 6 the blood did not cover the printed area completely, requiring the volume of blood to be again optimised. Figure 5.9-A shows the result of the three different volumes of blood tested, when compared to the iPA assay and increasing in increments of $50 \mu\text{l}$ from $100 \mu\text{l}$ to $200 \mu\text{l}$.

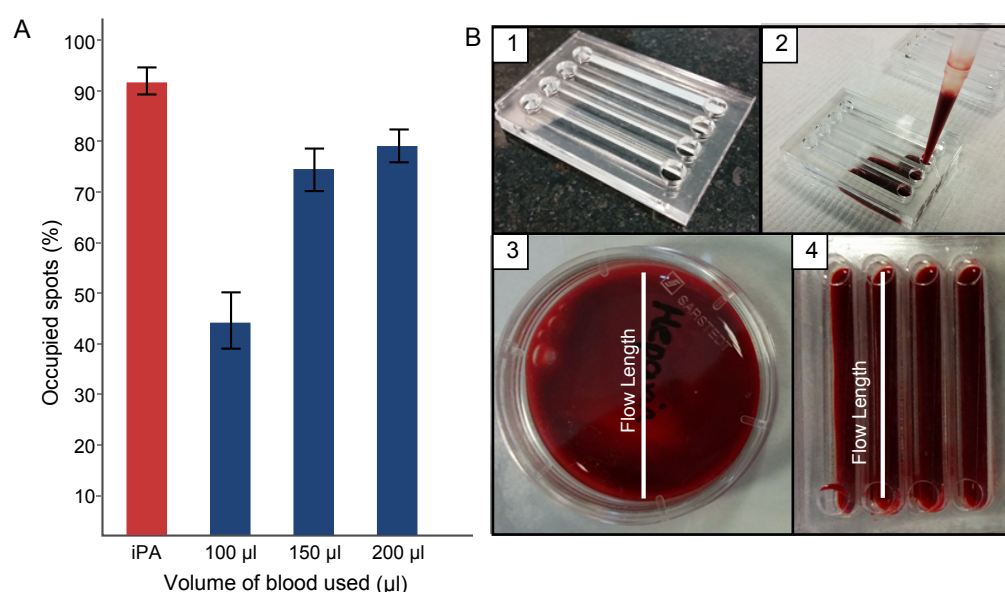


Figure 5.9: A) iPA assay compared to research chip filled with $100 \mu\text{l}$, $150 \mu\text{l}$ and $200 \mu\text{l}$ of blood. B) Pictures illustrating how the chip is filled and the flow length of the iPA assay and chip can be compared.

A difference of 3% was recorded for volumes of $150 \mu\text{l}$ (78%) and $200 \mu\text{l}$

(81%). Therefore, a volume of 200 μl was selected for use with both the research and integrated chip. This decision also allowed for the simplification of the blood delivery system used within the integrated chip, giving a possible range between 150 μl and 200 μl before the results are significantly affected. Figure 5.9-B illustrates how the research chip is filled, a picture of the petri dish used in the iPA assay is also shown alongside the full chip. It is clear from this picture how the flow length for the chip matches that of the dish and how the space used by four wells is equivalent to a single petri dish.

Research Chip Tested With $P2Y_{12}$ Inhibitor

Figure 5.10-A shows the comparison between the iPA assay (88%) and the research chip (81%) for 3 donors (12 wells per donor). This result shows that the combination of well type 6 and 200 μl volume of blood can give a comparable % platelet adhesion to that of iPA. Figure 5.10-B shows the resulting % platelet occupancy for an untreated sample of whole blood, whole blood treated with ADP and whole blood treated with ADP + Cangrelor.

The percentage of platelet adhesion was significantly decreased when the blood was treated with ADP resulting in a 5% occupancy when compared to the untreated blood at 78%. This effect was almost completely negated after the addition of Cangrelor to the ADP treated blood, resulting in a 74% occupancy, showing the research chip can detect $P2Y_{12}$ inhibition. This result follows that observed when testing drug effect using the iPA assay, showing the research chip's low blood volume, closed well, low form factor and multi well design can be used as an alternative iPA assay.

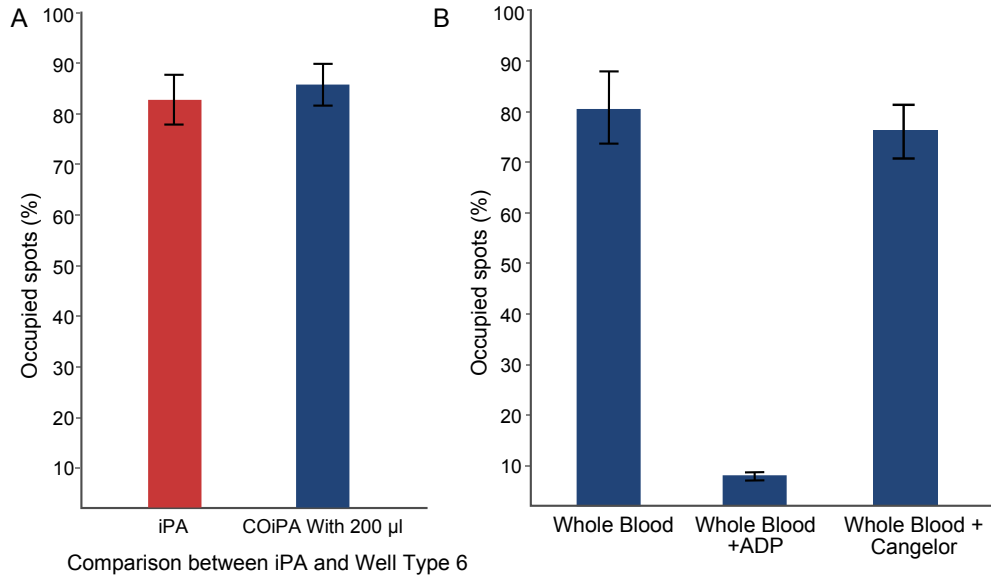


Figure 5.10: A) Comparison between iPA and COiPA. B) The detection of *in-vitro* P2Y₁₂ inhibition using the research chip. B) Platelet adhesion to fibrinogen dots (% occupied spots) in 4 healthy donors in whole blood, whole blood + 20 μ M ADP, and with ADP in the presence of 10 μ M Cangrelor. ($n = 5$)

5.4 Design of Integrated Chip

The research chip was further developed to allow for an integrated blood handling system to be used; the new design has the same well type as the research chip and includes two new layers. The introduction of a staging well allowed for a fixed volume of blood to be delivered to each assay well, while an existing blood handling technology manufactured by Sarstedt AG & Co was added to the chip. The blood can be collected from a patient using a disposable needle into a syringe containing an anti-coagulate; with the use of a connector fitted to the chip, the blood is transferred from the syringe to four staging wells.

Figure 5.11 shows the syringe which has been designed to be compatible with a number of different connectors. The connections allow for both a needle to be connected enabling blood draws from patients, and blood to flow into the prototype device. A large number of iterations of each design

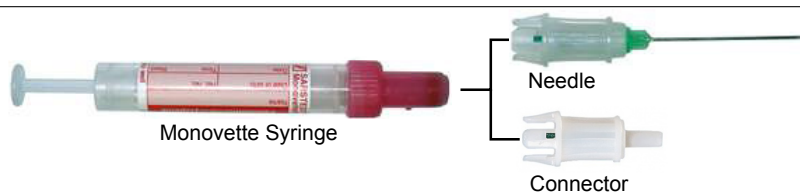


Figure 5.11: Monovette System used with device.

were required to address the issues with the previous version, with a total of six major versions of the chip detailed in Appendix E.

Flow Path Of Blood Within Integrated Chip

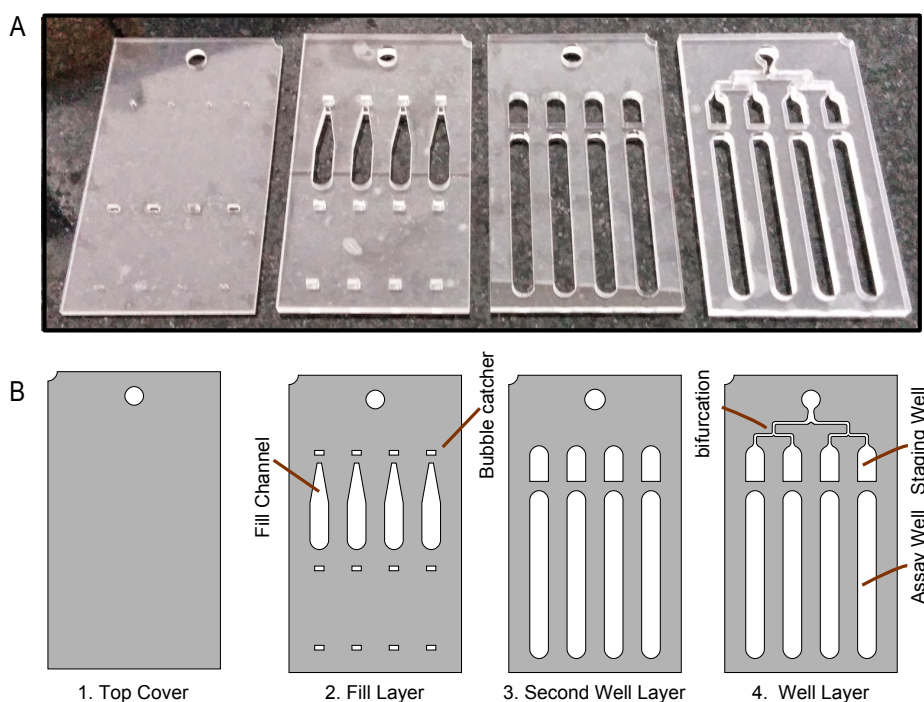


Figure 5.12: The final version of the chip. (A) The four layers that make up the chip excluding the Zeonor substrate and PSA gaskets. (B) A detailed view of each layer with the important features indicated.

Figure 5.12 shows the four layers of the integrated chip alongside the drawing of each layer detailing the key geometric features. The staging and assay wells are present within both layer 3 and 4, giving a total well height of 6 mm, which matches that of the research chip. The blood enters the

staging well within layer 4. Once all wells are full the blood passes through the fill channel within layer 2 and enters into the top of the assay channel. The shape of the fill channel was optimised to encourage the blood to spread as the channel is filled. This flow path reproduces how the research chip is filled, making it possible to compare results across the two chip types.

Staging Wells

Figure 5.13 shows how the blood passes from the syringe through the connector into a series of bifurcations, each delivering a single source of blood to each of the staging wells. The variability in the viscosity of blood and surface tension of blood was one of the biggest challenges when trying to deliver a fixed volume to the assay well. Surface tension γ is the magnitude F of the force exerted parallel to the surface of a liquid divided by the length L of the line over which the force acts, with units of N/m [2].

$$\gamma = \frac{F}{L} \tag{5.1}$$

The staging wells address both of these challenges with the use of geometric features and surface tension, stopping blood from leaving the staging well until each well is completely full. While the blood enters the well from the side it exits through the outlet at the top of the well. The outlet was designed to create a resistance to flow greater than the total resistance at the inlet of all four staging wells. The surface tension of the chip allows the blood to spread across the well as it enters, while the resistance at the outlet compensates for any small difference between how the blood spreads across each well. This simple solution has the effect of ensuring that no blood will leave the staging well before all wells are completely full and allows any one of the staging wells to start filling before another, removing the need for any valves within the chip.



Figure 5.13: The finish chip and how blood is loaded using the syringe to fill the staging wells.

Not all the blood from the staging well is moved to the assay well with a small amount left behind, leaving a volume greater than $5\ \mu\text{l}$ and less than $20\ \mu\text{l}$ remaining within the well. The well was designed to hold $185\ \mu\text{l}$ and the bifurcation $< 20\ \mu\text{l}$, giving a minimum of $185\ \mu\text{l}$ and a maximum of $200\ \mu\text{l}$ within the assay well. With both the research chip and integrated chip using the same well type these values fit well with the results from Figure 5.9-A, where no significant difference between $< 150\ \mu\text{l}$ and $< 200\ \mu\text{l}$ was recorded. Once all the staging wells are full the syringe is removed and replaced with a syringe full of air, used to push the blood from the staging wells into the assay wells. At this point both the research chip and integrated chip are treated the same for the remainder of the assay.

Fill Channels And Bubble Catcher

The fill channels were tapered from the staging well outlet to the assay well inlet. This change removed any corners where bubbles may form and also allowed any bubbles that did form to be pushed to the side where they would not affect flow. A small bubble catcher has also been added to remove any bubbles at both the staging and assay well. The catcher traps the bubble as it moves across the top surface of the chip by blocking its path to movement. Within the assay well the surface of the bubble in contact with the blood continues to move with the blood as it is rocked. The movement causes the bubble to become elongated and burst or splits into two or more easily to

manage bubbles. Once bubbles do not block the protein surface or restrict flow within the channel they do not adversely affect the results.

Integrated Chip Tested With $P2Y_{12}$ Inhibitor

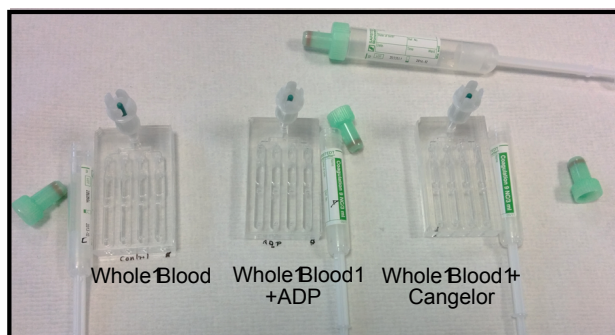
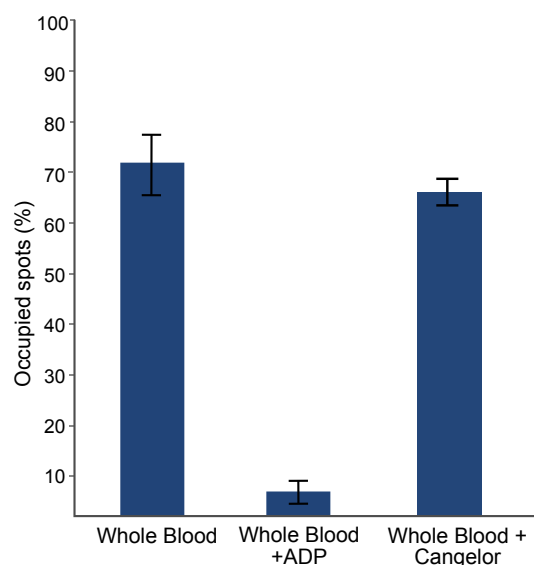


Figure 5.14: Detection of *in-vitro* $P2Y_{12}$ inhibition using the integrated chip. Three chips used with four wells per chip.

To determine if drug effect could be detected using the integrated chip an agonist was added to the blood to decrease platelet adhesion to the spots, an anti-platelet drug was then used to reverse this effect. Figure 5.14 shows the results closely matching those of the research chip (Figure 5.3), this is not surprising given that the only difference between the two chips was the inclusion of a blood handling system to deliver $200\ \mu\text{l}$ of blood to each well.

As the same blood sample is delivered to each well, the results from Figure 5.14 required the use of three chips (4 wells per chip) with untreated whole blood, whole blood and ADP and Whole blood + ADP + Cangelor. The ADP and Cangelor were added to blood before being placed into syringes. The integrated blood handling system, size, small blood volume and ability to easily scale the chip with more wells make the prototype chip ideal for use as part of a point-of-care system.

5.5 Summary

A number of different well shapes along with their location on the rocking table were tested to determine an optimal well shape for adhesion of platelets to 6 μm spots. The results showed a comparable % adhesion between iPA and COiPA when a rectangular well with rounded ends was used in place of the petri dish. For each iPA assay performed, over five COiPA assays could be completed with only 200 μl of blood in each well, allowing for unused blood to be left in the staging well of the integrated chips. The results from the early chip designs showed a difference between how blood flows and behave within a closed environment when compared to water, complicating the delivery of a sufficient volume of blood to the assay well. Different iterations of this design aimed to solve these issues, with the final prototype chip introducing a number of features including; a staging well, bubble catcher at the inlet and a tapered filling channel. The chip was successfully shown to detect drug effect and is well suited for use as part of a point-of-care system.

5.6 Discussion And Conclusions

This chapter described the different steps required to optimise the iPA assay for use within a low blood volume chip and introduced the concept of COiPA, used to successfully detect the inhibition of platelets in blood treated with Cangrelor in the presence of ADP. COiPA was also shown to correlate very well with results published by Lopez-Alonso *et. al.* [1]. The prototype device is the first to use a matrix of spots for the testing of anti-platelet therapies and offers a number of advantages when compared to the VerifyNow, LTA and PFA-100 systems. With further development lyophilised agonists could be added to each well, allowing for multiple anti-platelet therapies to be tested at the same time using only $200\mu\text{l}$ of blood per well; currently available tests can only test a single therapy at a time. The VerifyNow is the only other device to integrate a standard blood handling system onto a cartridge, with a separate cartridge and blood draw required for each VerifyNow test. The integrated chip would require a single blood draw to complete multiple tests.

The integrated chip introduced a number of novel features for dealing with bubble formation and allowing a controlled volume of blood to be delivered to each well. At the same time, the chip allows for blood to be loaded using a sharps-safe, integrated connector within a fully sealed disposable chip. As an early prototype, the chip performance was excellent. However, there is a need for further development to improve assembly time and reduce delamination and leaking as a result of dust or debris adhering to the PSA during assembly. The current chip design has four assay wells for the testing of dual anti-platelet therapies, new therapies or different concentrations of an antagonist could be added to the assay with the easy addition of wells to the chip. Results show the optimised COiPA assay is comparable to the current iPA assay. The prototype has enormous potential as part

of a point-of-care system for the assessment of platelet reactivity during anti-platelet therapy. The requirement to label the platelets to obtain a result for the iPA assay, has the potential to make any point-of-care system complicated, time consuming and costly. For this reason, a new image technique was developed to allow platelets to be imaged without the need to first label them. Introduced in the next chapter, this technique reduces system complication, assay cost and will reduce the assay time.

Bibliography

- [1] Dermot Kenny Ana Lopez-Alonso, Bincy Jose, Martin Sommers, Karl Egan, David P. Foley, Antonio J. Ricco, Sofia Ramstrom, Lourdes Basabe-Desmonts. Individual Platelet Adhesion (iPA) Assay: Measuring Platelet Function and Anti-Platelet Therapies in Whole Blood via Digital Quantification of Cell Adhesion. *Analytical Chemistry*, 85(13):6497–6504, 2013.
- [2] Douglas C. Giancoli. *Physics for Scientists and Engineers with Modern Physics, Volume 2*. Pearson Prentice Hall, 2008.

Chapter 6

System Automation

6.1 Introduction

Both the Individual Platelet Adhesion (iPA) and Chip Optimised Individual Platelet Adhesion (COiPA) assays require a number of manual steps to obtain the resulting % of occupied spots. The need to fluorescently label the platelets after the blood has been rocked and the requirement to count each platelet adhered in order to calculate the % of occupied spots, all added to the overall assay time. For each printed area of fibrinogen spots a number of different regions were imaged, using a fluorescent microscope. By calculating the % of fibrinogen spots occupied for each image set, an average value across the full printed area can be calculated. An image set contains an image of the 6 μm spots and a corresponding image of adhered platelets to the same area. This chapter introduces a custom built software package that includes a new automated image processing technique to calculate % of spots occupied from both the image of fibrinogen spots (red) and the platelet image (green). The software also performed a number of quality control checks on the μ -contacted printed protein array.

The prototype device (detailed in Chapter 5) was designed as a closed

system, making it more suited as part of a point-of-care device. This closed system created a complexity when trying to introduce the platelet specific antibodies, required to image the platelets. To overcome the need for labelling, a novel imaging technique was developed. This technique removed the need to label the platelets and only requires images to be taken of the surface, simplifying the acquisition of results from the assay, reducing complexity, cost and the overall time by 1.5 hours. The label-free detection method does not require the blood to be treated in any way, or the blood to be removed from the chip. This technique has practical applications outside of this project and could be used to detect adhesion of any cell type to a protein array, potentially allowing for the simplification of existing or the development of new device assays.

6.1.1 MATLAB Software

While a MATLAB script was available to automate the calculation of results, it required a number of manual steps, was slow to run, was limited to a single set of images and required a colour camera. The software was also unreliable resulting in false positives; these errors occurred as a result of the approach used and the absence of any quality control of the acquired images. The user interface was also overly complicated with an ability to change settings and required the user to manual input each file location. As the MATLAB script also lacked any version control, when a bug was fixed there was no way of knowing if the change would affect older results, requiring the image sets to be rerun through an already time-consuming process.

6.2 Matched Feature Methods

The newly developed software includes a number of different methods used to calculate the resulting % of spots occupied, with each technique tailored for a different need. Each method incorporates blob analysis, used to determine the location of each platelet and protein spot within the image set being processed. By searching the array image for suitable features it is possible to check the platelet image for a corresponding feature and thereby detect when a platelet has adhered to a spot. Two Matched Feature Methods (MFM) are included in the software. The first offers the operator a semi-automated interface and allows the % of occupied spots to be manually calculated. The second is fully automated and only requires the operator to select the image location on the PC.

Manual Method

Figure 6.1 shows two images side by side after the user has selected the image set they wish to manually calculate, the % of occupied spots from. The right hand side of the window shows the image of the platelets and the left hand side shows the image of the fibrinogen spots. Images were acquired using a monochrome camera. Feedback colour was added by the software to make it easier for the user to find both the fibrinogen spots and platelets. The software uses a Cartesian coordinate system; an object is highlighted within the figure at location $x = 30$ and location $x = 34$. The software calculates the coordinate for a platelet (from the platelet image) as the user uses the mouse to select the location by clicking the mouse. As the mouse is moved across the image, a corresponding cursor moves to the same coordinate within the spot image. This allows the user to visually determine if a platelet has adhered to a spot. By right-clicking the mouse the user is indicating that the platelet has adhered to a spot. The click indicates

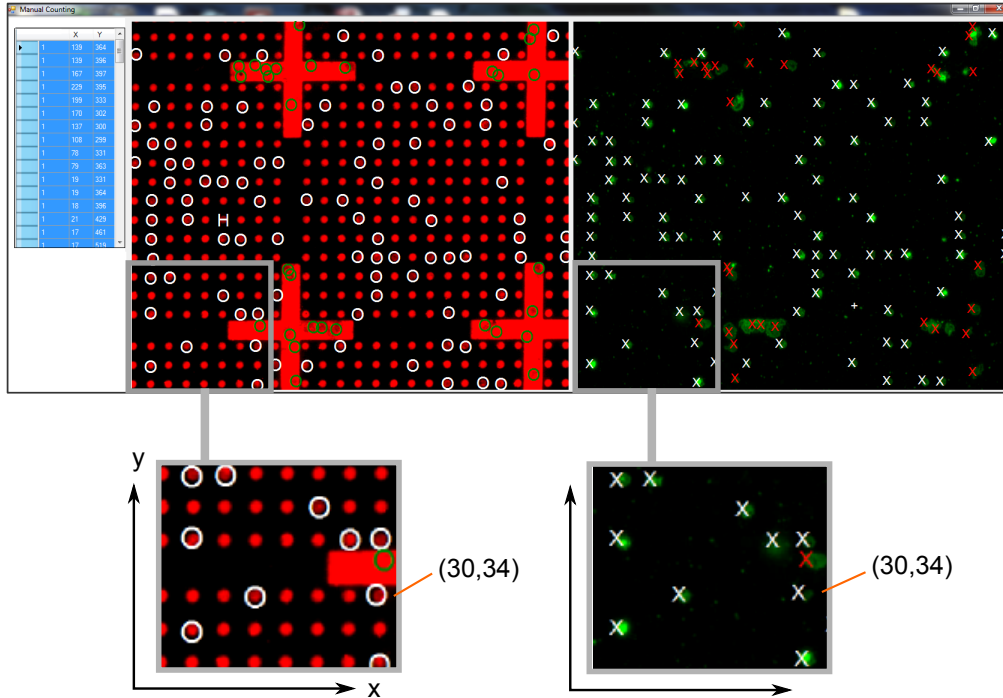


Figure 6.1: Snapshot of window used to manually count adhered platelets to $6\ \mu\text{m}$ spots. The image was captured from within the iPlatelet software, with the image of arrayed fibrinogen displayed on the left and the platelet image to the right of the window.

the platelet is not adhered to the spot and therefore should not be counted. Four crosses encapsulate a 13×13 array of spots and were originally included to allow the user to easily select a fixed number of spots from the image, used to calculate the % of occupied spots. When the user left clicks on the platelet a white X is added to mark the location within the platelet image and a white circle within the matrix image. The location and click selection is also added to a list box (left hand side of Figure 6.1), allowing the user to copy the data into an Excel spreadsheet for later analysis.

Automated Method

The automated matched feature method takes advantage of an image processing technique called blob analysis [1]. This method converts each feature

within the image into a matrix called a blob, the blob itself is a binary representation of the feature and allows for metadata about the feature to be calculated. This metadata includes attributes of the feature such as the centre of gravity (CoG), smallest rectangle to bind the feature, feature shape and the feature size. A detailed explanation of image processing techniques is included in Appendix F.

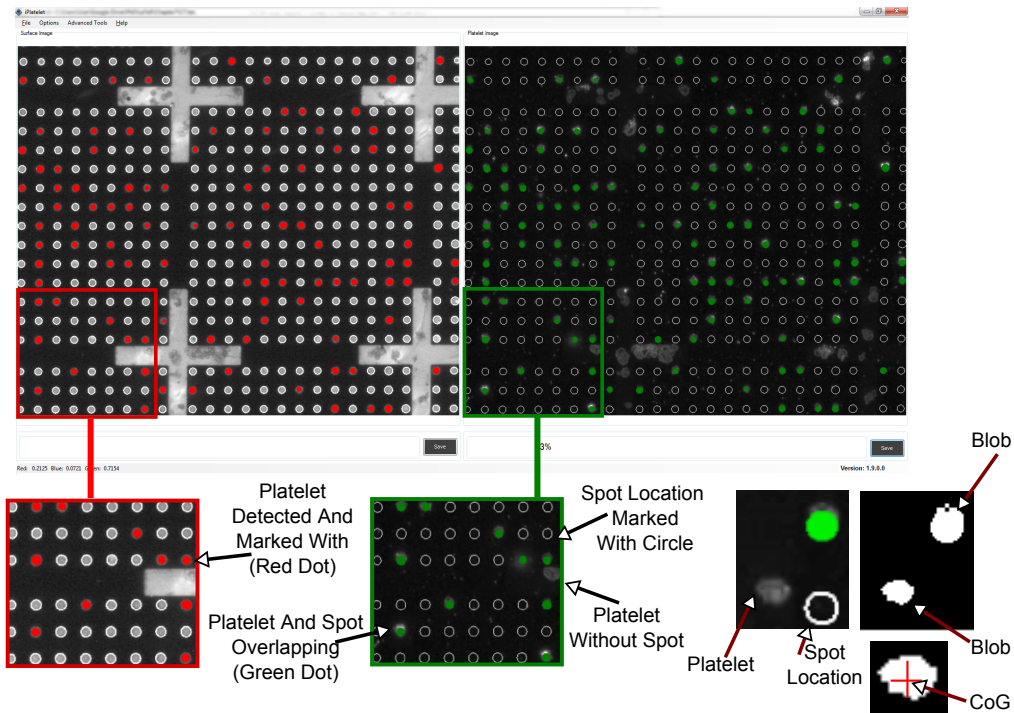


Figure 6.2: Snapshot of window used to calculate the % occupancy for a single image set using the automated matched feature method (AMFM). The image was captured from within the iPlatelet software. The image of arrayed fibrinogen is displayed on the left and the platelet image to the right of the window. The platelets are marked with a green dot while the corresponding $6 \mu m$ spot is marked with a red dot.

Figure 6.2 shows a section of the platelet image containing two platelets, alongside the blobs representing each platelet. Each spot within the image of fibrinogen spots was first converted into a blob creating a blob array, before calculating the CoG for each blob within the array. This process was then repeated for the platelet image and the CoG of each spot within

the blob array was checked to determine if it lies within any blob contained within the platelet blob array, allowing for the % of occupied spots to be automatically calculated. A graphic representation for a sample image set with the CoG of each spot superimposed onto the platelet image is included in Figure 6.2. It is clear from the platelet image that none of the platelets that have adhered to the crosses (visible within the matrix image) have been used when calculating the % of occupied spots. The removal of the need to use colour images, automated file selection, performance improvements and version control give this automated method a number of advantages over the MATLAB script. The removal of the need for a colour microscope may allow the assay to be imaged using a less expensive microscope, making the assay easier to use in a non-laboratory setting

Each image set contains both the matrix image and platelet image and are processed simultaneously with each image set requiring less than a second. If the software is not required to render the output image the software can return a faster result. With at least 4 image sets per well and multiples of each experiment required, there can be a large number of image sets to be processed at a single time. The software was written with managed and unmanaged code; when managed code is used the computer memory is managed by a framework. While managed code has a number of advantages when programming applications with a user interface, it is unsuited for image processing, requiring the software to use a mixture of the two. If the image is not rendered the software uses only unmanaged code and can return results for 50 image sets in about 45 seconds, whereas the MATLAB script would take about 1 hour in total. This technique also includes a quality control step. All calculations were carried out using a HP elitebook 8730w with 4GB of DDR2-800 RAM and an Intel Core 2 Extreme QX9300 (2.53GHz) 12MB cache. An NVIDIA Quadro FX 2700M with 512 MB of dedicated video memory was also available. Computational time is depen-

dent on computer resources available at the time the program is run, the hard disk can limit the performance when rendering the image. It takes approximately 102 s to render and get results for the same 50 image sets that take 45 s without rendering.

Quality Control Of Spots

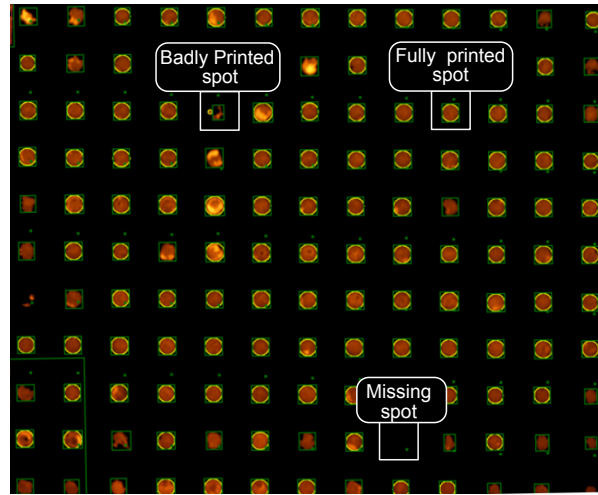


Figure 6.3: Image of an array of spots showing the output of the quality control test applied to each spot, a missing, misprinted and fully printed spot are each highlighted. Missing and misprinted spots are removed from the calculation even if a platelet has adhered at that location.

By checking the shape of each spot any badly printed spots can be ignored when calculating the % of occupied spots. Even if a platelet has adhered to a badly printed spot the software will ignore it. When no spot is detected any platelet within that area is also ignored. Figure 6.1 shows the software automation also excluded any platelets adhered to the crosses found within the image, thereby resulting in the inclusion of only platelets which have adhered to fully printed spots when calculating the % occupancy

6.3 Label-Free Detection

Label-Free Detection (LFD) takes advantage of the optical properties of the Zeonor (Cyclo Olefin Polymer) substrate, allowing for the automated calculation of the % occupancy from a single image. Developed during this project, LFD removes the need to handle the blood in order to calculate the % of occupied spots, which is not possible when one of the feature methods was used. With no need to label the blood the assay time is reduced by 1 hour and 30 minutes, and the need to design and integrate a system to label the blood within the prototype device is also removed. While the technique still required the labelling of the fibrinogen spots, this can be done when the fibrinogen is μ -contact printed. This method introduced a new set of challenges, requiring the software to detect the location, despite the orientation when printed, of each spot within the array. The development of new post-processing filters was required in order to determine if a platelet had adhered to a given spot. The method used to detect the orientation of the array, including the filters used, is detailed in Appendix F

6.3.1 Characterisation of Spot for LFD

An interesting phenomenon causing a decrease in the intensity of the spots to which a platelet has adhered was observed (within the array image). It is this phenomenon that makes label-free detection possible. Figure 6.4 shows a comparison between the same region for a sample image set. A spot of low intensity and high intensity are labelled to demonstrate this difference, with the light being absorbed by the adhered platelet accounting for the difference. However, it is also possible that the low intensity spot could be a result of a badly printed, missing spot, an inconsistency in dye absorbed by the fibrinogen, or the Alexa-488 dye used with the platelets. To determine if this was the case the assay was tested without the platelets

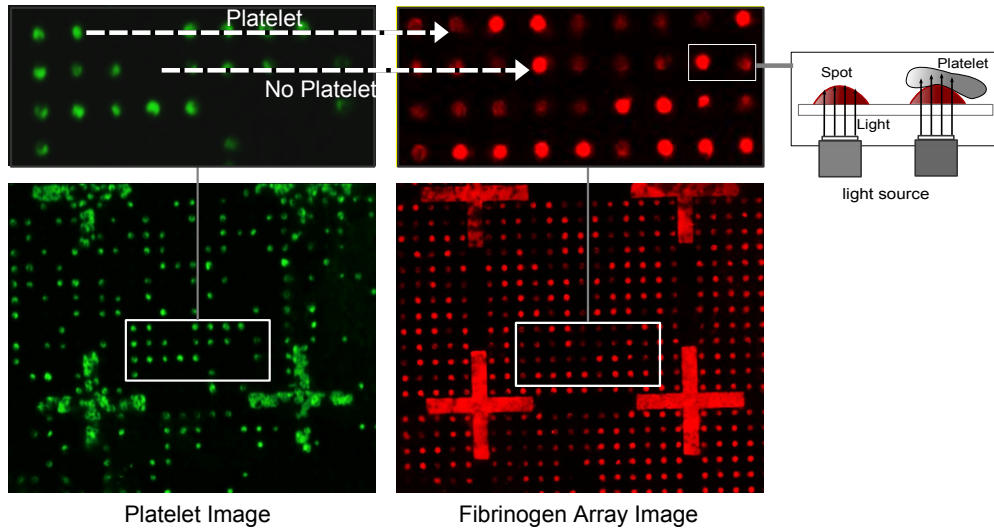


Figure 6.4: Images of both labelled fibrinogen and labelled platelets with two spots highlighted, with and without a platelet adhered. The difference in intensity makes it possible to determine the of a platelet.

labelled.

Using bright field images taken of the unlabelled platelets along with images of the labelled fibrinogen, a comparison could be made between the two. Figure 6.5 shows a section of a sample image set with the platelets circled within both images. The results show the same difference in intensity is clearly visible and correlates with the presence of an adhered platelet within the bright field image, indicating that the labelling of platelets has no effect on the results calculated using LFD. With the knowledge that labelling platelets has no effect on the intensity of a spot a method to automatically test each spot for the presence of a platelet was developed. Using the technique described in Section F.1.1 a mesh was build and the region that enclosed each spot location was extracted. With the use of a newly developed filter the presence of an outer ring, similar to a coffee ring, was observed within some regions. This coffee ring effect was only present when no platelet had adhered.

Figure 6.6 shows a selected area of a sample image and the results for

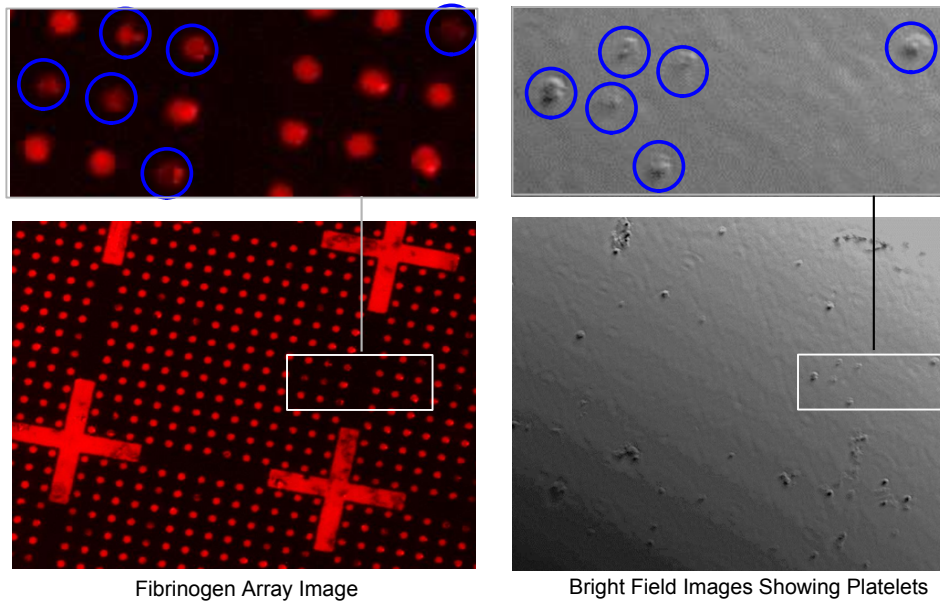


Figure 6.5: Two images of a corresponding area using both a cy3 filter and brightfield. The brightfield image shows platelets are clearly visible and match spot locations, indicating platelet labelling is not required for LFD.

the LFD method. By applying a custom combined scaling and high-pass filter (HPF) to each region extracted from the image. The scaling filter uses the mean intensity for all extracted regions as the scale factor, while the HPF removes the lower values to reduce noise created as a result of the scale filter. Any values greater than 255 are set to zero, thereby creating a black hole at the centre of each unoccupied spot (coffee ring effect). A blob is extracted from each region and a histogram in both x and y is created. From the two sample histograms shown in Figure 6.6, the difference between occupied and unoccupied spots can be clearly defined. Using the resulting histograms the software divides the spots into two groupings, occupied and unoccupied.

Second Pass Characterisation

An average curve is created for each group using the unfiltered region; these average curves allow for an upper and lower band to be calculated. The

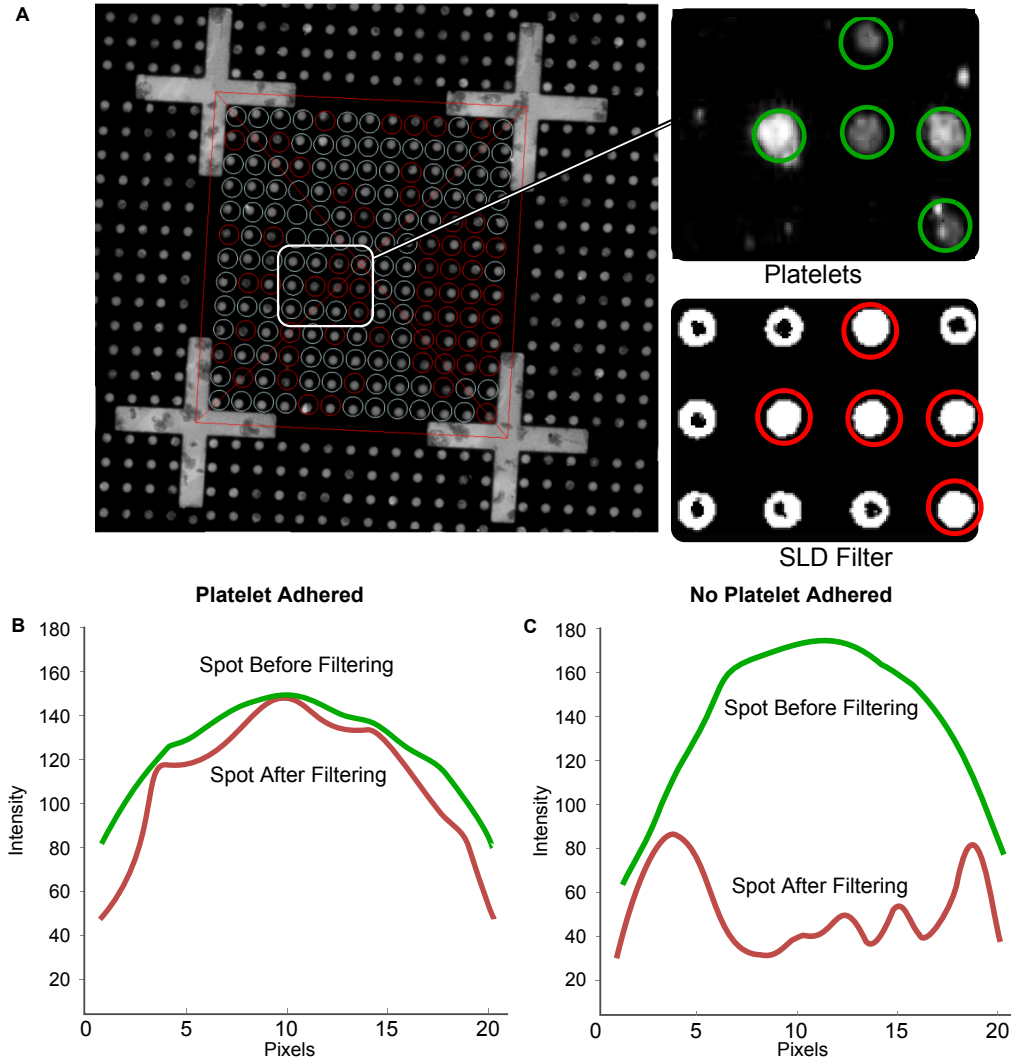


Figure 6.6: Graphical demonstration that combines a mesh alongside the LFD filter. A) Sample image with mesh applied alongside a region highlighting the output of the LFD Filter. B and C) histograms for a single spot detailed the change in output used to classify a spot. The green line shows the curve before the filter is applied and the red line shows the output curve.

upper band is defined as the intensity value half way between the maximum intensity values taken from the occupied and unoccupied curves, while the lower is half way between the upper band and the maximum intensity value of the unoccupied curve. Any curves that fall inside of the upper and lower band are removed from the unoccupied group and not included when the % occupancy is calculated. This step removes those spots that were not

removed during the quality control of the image and which the filter is unable to clearly define as unoccupied.

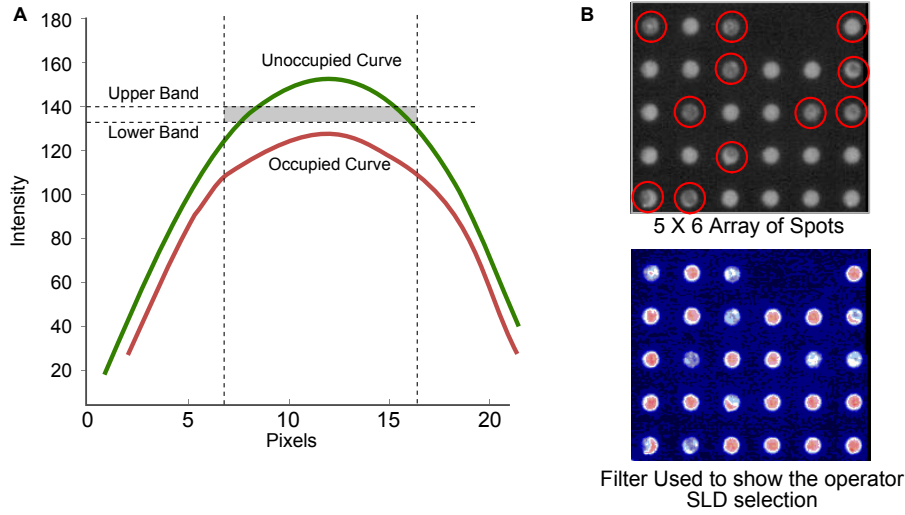


Figure 6.7: Plot of the average curves used during the second pass characterisation. A) Shows the curves for a 5×6 sample array used to calculate the upper and lower bands. The green curve represents no platelets detected, while the red curve (lower average intensity) represents adhered platelets. B) An image of the area averaged with the spots containing platelets circled, alongside a colour image of a filter used to show the operator which spot LFD may select.

Figure 6.7-A illustrates the average curves for a 5×6 sample area of spots, the results show a significant difference between the curves for the occupied and non-occupied groups. The area enclosed within the upper and lower bands is also illustrated to demonstrate the region in which spots will be rejected. A single image may contain 430 spots and the number of unclassified spots may be between 4 and 15, giving a maximum error of approximately 3.5%. An image of the array is included in Figure 6.7-B alongside a colourised version used to help the operator to identify spots with and without platelets adhered if they wish to do so.

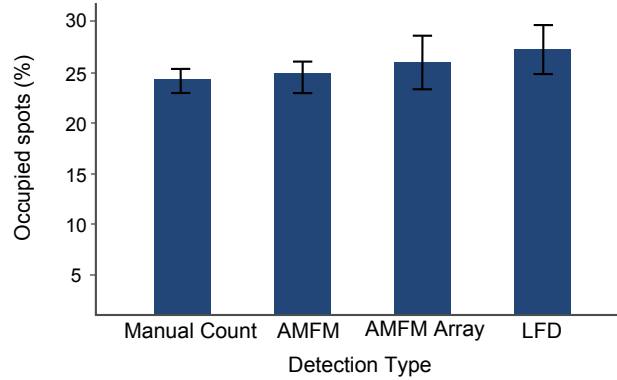


Figure 6.8: The resulting % of occupied spots using different detection methods. Image sets were taken from a single donor and the resulting % of occupied spots calculated using the available methods.

6.3.2 Results

Figure 6.8 shows results for 6 image sets taken from a single donor with ADP added to the sample. The % platelet occupancy was calculated using the four available methods, manual counting, automated matched feature method (AMFM), AMFM for a 13×13 array, and label-free (LFD). It can be assumed that all adhered platelets were counted manually, allowing this result to be used as a reference value. The correlation between the first two methods is excellent with a difference of 0.3%, showing the automated software can be used to make a reliable comparison. A difference of 1.5% (standard deviation of ± 2.6) was noted between AMFM and AMFM Array (13×13 array). There is also no statistical difference between these results and manual counting, indicating counting of just those spots within the array is sufficient to calculate the % occupancy. When LFD was applied a value of 27.6 ± 2.8 was calculated. This result compared well with the three matched feature methods with a maximum difference of 3.5% recorded, between LFD and manual counting. This difference could be explained by the spots excluded during the quality control checks carried out during label-free detection. The detection methods detailed in this chapter are designed

to allow automated results to be calculated for the iPA assay. Given that the object is to integrate a point-of-care chip with a suitable imaging system, the advantages offered by LFD make it an ideal candidate, as it allows for a much simpler system to be designed. The 5.9% difference between manual counting and LFD could be reduced with additional tuning of the filters. However, given that any simplified imaging system will require optimisation and that the result is still within the dynamic range of the assay (50%), there may be no need for further development of the LFD filters using the current microscope.

6.3.3 Conclusions

There are a number of commercial and open-source (free) software packages available for the processing of biological images. However, on investigation these software packages were not easily adapted to automation of the image processing required for this project. There are a number of advantages in using the iPlatelet software over other programs. These include, licence free use, fast response to feature requests and bug reports, the ability to control the complexity of the user interface, inclusion of custom hardware control elements (if required), and the seamless calculation of results in a format the user requires. The software can also be updated to include encryption, remote management, user control, and to import results into an existing database available at the Clinical Research Centre (CRC) which complies with statutory data protection.

The development of the matched feature method (integrated into the iPlatelet software) reduced the overall assay time and for the first time allowed the % occupancy to be calculated in a fully integrated, robust and reproducible environment.

The method correlates with manual counting and reduces the calcula-

tion time from 15 minutes to under a second, it was also found to have an advantage over the MATLAB script, described at the start of the chapter. With a significant decrease in assay time and the removal of the need for a colour camera to be used to acquire the image sets, the matched feature method introduces the possibility that the assay could be imaged using a low-cost microscope. LFD has been shown to correlate with the three different matched feature methods developed and does not require the platelets to be labelled, reducing the assay time by one and a half hours. The removal of the need to label platelets allows results to be calculated for the iPlatematrix(iPM) chip without the need to design a delivery system to first label the platelets. The integration of the iPlatematrix(iPM) alongside LFD has great possibility for the design of an automated low-cost prototype point-of-care device, as any imaging system only requires a single filter, thereby removing the need for complex moving parts and multiple light sources. LFD also works with the degas-driven flow chip and the iPA assay.

Bibliography

- [1] Thomas B. Moeslund. *Introduction to Video and Image Processing: Building Real Systems and Applications*. Springer Science & Business Media, 2012.

Chapter 7

Conclusions

Two unique BioMEMS systems have been developed and shown to successfully test the efficacy of anti-platelet therapies. The first system exploited the material properties of PDMS to facilitate power-free pumping, while the second allows for multiple tests to be carried out at the same time within a single chip. The systems use a new image analysis technique and software to objectively quantify single platelet binding events, without the need to label the sample blood. The objectives of this work as described in Chapter 1 were realised.

1. *To identify and develop new technologies that can be used to design and build a single-use prototype point-of-care device to test anti-platelet therapies.*

While the iPA assay had already been shown to detect the efficacy of anti-platelet therapies [1], it was still time-consuming, required a high degree of manual steps, and had only minimum assay optimisation completed. Degas-driven flow had the potential to meet these challenges as it removed the need for external pumping and allowed for a prototype single-use chip to be created. A new low cost manufacturing technique was developed and characterised. The technique was

used to rapidly create different iterations of the chip design, before a final degas-driven device was successfully used to test the efficacy of anti-platelet therapies. The device demonstrated how degas-driven flow allowed for a reproducible and controllable flow rate for a given assay time. This control gives the device potential to be used with flow based assays beyond platelet function.

2. *To develop new image processing techniques that will allow for the automated quality control of a printed protein surface.*

The iPlatematrix device was developed to minimise the iPA assay within a single-use prototype point-of-care device, dealing with any bubble formation, while at the same time allowing for blood to be loaded using a sharps-safe, integrated connector within a fully sealed disposable chip. The results show the optimised MiPA assay is comparable to the current iPA assay and has enormous potential as part of a point-of-care system for the assessment of platelet reactivity during anti-platelet therapy. The addition of wells to the integrated chip could allow for new therapies to be added to the assay or different concentrations of an antagonist to be tested giving the integrated chip potential advantages over the VerifyNow and LTA systems. The development of the matched feature method (integrated into the iPlatelet software) reduced the overall assay time and for the first time allowed the % occupancy to be calculated in a fully integrated, robust and reproducible environment. The method correlates with manual counting and reduces the calculation time from 15 minutes to under a second. With a significant decrease in assay time and the removal of the need for a colour camera to be used to acquire the image sets, the matched feature method introduces the possibility that the assay could be imaged using a low cost microscope.

3. *To develop a technique to automate acquisition of results from complex protein arrays used with the prototype device.*

Label-Free Detection (LFD) has been shown to correlate with the three different matched feature methods developed and does not require the platelets to be labelled, reducing the assay time by one and a half hours. The removal of the need to label platelets allows results to be calculated for the iPlatematrix(iPM) chip without the need to design a delivery system to first label the platelets. The integration of the iPlatematrix(iPM) alongside SLD has great possibility for the design of an automated low-cost prototype point-of-care device, as any imaging system only requires a single filter, thereby removing the need for complex moving parts and multiple light sources.

7.0.4 Future Work

Although both systems have had been shown to successfully test the efficacy of anti-platelet therapies there is still room for further developments, that could improve overall functionality of the systems.

Integrated chip

While the layers of the chip are currently laser cut in-house, if a large number of chips are required it may be necessary to have a commercial operator cut and assemble the parts. This change could require both aesthetic and functional design changes to the chip; these changes must be managed so as not to affect the flow conditions. It may also be advantageous to investigate different manufacturing options such as sonic welding to remove the need for PSA, injection, compression or transfer moulding of some parts.

Imaging

Replacing the current camera with a low-cost option may result in the requirement to introduce additional optics to improve signal quality, reduce the effect of background light where possible, optimisation of camera settings and reduction in external effects such as vibration that could reduce image quality. A low cost light source would also need to be tested in combination with the camera. Thereby, creating a complete imaging system that would work with the prototype device.

Software automation

In terms of software improvements, more in-depth image processing could potentially improve image quality allowing images acquired from the low-cost imaging system to be processed. The further improvement of an algorithm used to specifically identify platelet adhesion, could reduce the cost of any potential imaging system by enabling detection from images with a higher noise-to-signal ratio.

Diagnostic development

Although the devices were validated using whole blood response to fibrinogen spots and ADP, there is no limitation, in principle, to further investigations using alternative agonists of interest. The device and readout system would remain suited to imaging and recording platelet-spot interactions in whole blood in response to various agonists to study the efficacy of the multitude of anti-platelet therapies.

Bibliography

- [1] Dermot Kenny Ana Lopez-Alonso, Bincy Jose, Martin Sommers, Karl Egan, David P. Foley, Antonio J. Ricco, Sofia Ramstrom, Lourdes Basabe-Desmonts. Individual Platelet Adhesion (iPA) Assay: Measuring Platelet Function and Anti-Platelet Therapies in Whole Blood via Digital Quantification of Cell Adhesion. *Analytical Chemistry*, 85(13):6497–6504, 2013.

Appendices

Appendix A

Platelet Surface Receptors

$P2Y_{12}$ belongs to the G_i class of a group of G protein-coupled (GPCR) receptors, it is also a chemoreceptor for adenosine diphosphate (ADP). This receptor plays a central role in platelet activation and is the target of $P2Y_{12}$ receptor antagonists. Table A.1 list a range of receptors and their ligand.

Receptor	Ligand	Integrin	Action
GPIa/IIa	Collagen	$\alpha_2\beta_1$	Adhesion
GPIb/IX	vonWillebrand Factor	-	
GPIc/IIa	Fibronectin	$\alpha_5\beta_1$	Adhesion
GPIIb/IIIa	Collagen Aggregation		Aggregation
	Fibrinogen		(secondary role
	Fibronectin	$\alpha_{IIb}\beta_3$	in adhesion)
	Vitronectin		
GPIV	vonWillebrand factor		
GPVI	Thrombospondin, collagen	—	
GPVI	Collagen		Adhesion
Vitronectin	Vitronectin Thrombospondin	$A_v\beta_3$	Adhesion

Table A.1: List of surface membrane glycoprotein receptors in blood.

Name	Usage
Bleeding time	Widely used
Light transmission aggregometry (LTA)	-
PFA-100	-
Flow cytometry	-
VerifyNow [©]	Used in specialised labs
Impact-R [©] (cone and platelet analyser)	Only recently available
AspirinWorks [©]	Increasing use
Thromboelastography (TEG)	Surgery and anesthesiology
HemoStatus [©]	Surgery and cardiology

Table A.2: Platelet function Analysis Systems

Appendix B

Biological Background

B.0.5 Materials Used

All reagents were purchased from Sigma-Aldrich (St Louis, MO, USA) unless otherwise indicated. Device fabrication: Polydimethylsiloxane (PDMS), (DowCorning Sylgard 184) was purchased from Farnell (Farnell Ireland, Dublin, Ireland). Poly(cycloolefin) sheets were obtained from Ibbidi GmbH (Munich, Germany), 1.5mm thick polymethyl-methacrylate (PMMA) was purchased from Radionics (Ireland), 50 μm and 80 μm high double-sided pressure sensitive adhesive (PSA) laminate: Arcare 8890 were purchased from Adhesives Research (Limerick Ireland) human fibrinogen (95% clottable and plasminogen depleted) was purchased from Calbiochem (Merck, KGaA, Darmstadt, Germany) and Cy3 labelled Bovine serum albumin (BSA) was purchased from ChemQuest Limited (Wilmslow, UK). Platelet assays: anti-CD41 mouse monoclonal antibody (clone P2, was obtained from Immunotech, Marseilles, France), Alexa Fluor 488 labelled goat anti-mouse and goat anti-rabbit antibodies were obtained from Invitrogen, (Carlsbad, CA), 4.5ml Vacutainer containing 3.2% sodium citrate were purchased from Becton Dickinson UK Limited, (Oxford, UK), adenosine Diphosphate was obtained from BioData (Horsham, PA, USA), abciximab (ReoPro) was

purchased from Eli Lilly and company (Indianapolis, IN, USA) and canrelor was from The Medicines Company (Parsippany, NJ, USA).

B.0.6 Patterning on Poly(cycloolefin) Sheet

3-Aminopropyltriethoxysilane (APTES) functionalised poly(cycloolefin) sheets were cut into to size and a 200 $\mu\text{g}/\text{mL}$ fibrinogen solution made in 1X PBS containing Cy3 labelled bovine serum albumin (BSA, 25 $\mu\text{g}/\text{mL}$), to aid the visualization of the fibrinogen on the slide, was either drop coated or μ -contact printed onto the slide surface. 50 μL of the fibrinogen solution was drop-coated on a poly(cycloolefin) and the remaining solution was removed from the sheet after incubation at room temperature for an hour. The fibrinogen coated slide was then completely blocked with 1 % (w/v) BSA solution. The fibrinogen solution was patterned on the slide surface using μ -contact printing as described previously. Briefly, patterned PDMS stamps were fabricated by pouring a 10:1 (v/v) mixture of Sylgard 184 elastomer and curing agent over a patterned silicon master. After curing for 1 hr in an oven at 70°C the PDMS was removed from the master and the PDMS stamps were inked with 50 μL of the fibrinogen solution for 30 min. The excess fibrinogen solution was then removed from the PDMS stamp using a pipette and the stamp was dried with nitrogen. The stamp was then placed in contact with the APTES treated poly(cycloolefin) sheet for 5 min. After printing, the whole sheet is blocked with 1% (w/v) BSA solution in PBS.

B.0.7 Blood Collection and Sample Preparation

Venous blood was collected from healthy adult volunteers who had not ingested any drugs known to interfere with platelet function for at least 2 weeks prior to phlebotomy. Blood was collected by venipuncture through a 19-gauge needle into a 4.5ml Vacutainer containing 3.2% (v/v) sodium citrate (Becton, Dickinson U.K. Limited, Oxford, UK). The citrated whole blood was either loaded directly onto the device or incubated with anti-platelet drugs. To prevent the binding of platelets to fibrinogen various concentrations (0, 2, 2.5, 3, 4, 5, and 6 $\mu\text{g/mL}$) of abciximab (ReoPro) were incubated with the citrated blood for 15 min at 37°C before loading onto the device. In order to assess the effect of anti-platelet drugs, the citrated whole blood was incubated with a final concentration of 10 μM cangrelor for 15 min at 37°C . The agonist adenosine diphosphate (ADP), to a final concentration of 20 μM was added to the cangrelor treated and untreated whole blood prior to loading onto the device.

Appendix C

Equations of Motion

C.1 Conservation of Mass

Consider the volume in Figure C.1 showing an idealised fixed control volume of fluid. Since the flow through each side is considered approximately one dimensional the conservation of mass states the change in density of the volume over the surface plus mass flow in less the mass flow out sums to zero or:

$$\int_{\Omega} \frac{\partial \rho}{\partial t} dV + \sum_i (\rho_i A_i V_i)_{out} - \sum_i (\rho_i A_i V_i)_{in} = 0 \quad (C.1)$$

Since the volume element is so small the integral reduces to the differential term:

$$\int_{\Omega} \frac{\partial \rho}{\partial t} dV \approx \frac{\partial \rho}{\partial t} dxdydz \quad (C.2)$$

Since the mass flow acts on all six faces of the control and the the fluid is assumed to be a continuum we can list all six flows as shown in TableC.2

Substituting these values into eqn C.1 we get:

$$\frac{\partial \rho}{\partial t} dxdydz + \frac{\partial}{\partial x}(\rho u) dxdydz + \frac{\partial}{\partial y}(\rho v) dxdydz + \frac{\partial}{\partial z}(\rho w) dxdydz = 0 \quad (C.3)$$

Face	Inlet mass flow	Outlet mass flow
x	$\rho u \, dy \, dz$	$\left[\rho u + \frac{\partial}{\partial x} (\rho u) \, dx \right] dy \, dz$
y	$\rho v \, dx \, dz$	$\left[\rho v + \frac{\partial}{\partial y} (\rho v) \, dy \right] dx \, dz$
z	$\rho w \, dx \, dy$	$\left[\rho w + \frac{\partial}{\partial z} (\rho w) \, dz \right] dx \, dy$

Table C.1: Mass flow table

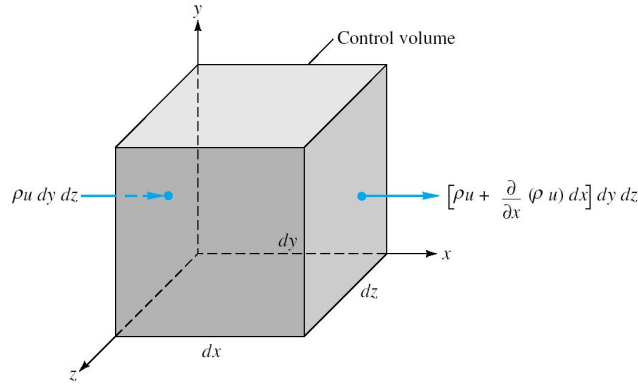


Figure C.1: Control volume showing mass flow in x direction

The element volume cancels to leave:

$$\frac{\partial \rho}{\partial t} + \frac{\partial}{\partial x}(\rho u) + \frac{\partial}{\partial y}(\rho v) + \frac{\partial}{\partial z}(\rho w) = 0 \quad (\text{C.4})$$

Using the nabla function:

$$\nabla = \mathbf{i} \frac{\partial}{\partial x} + \mathbf{j} \frac{\partial}{\partial y} + \mathbf{k} \frac{\partial}{\partial z} \quad (\text{C.5})$$

We can rewrite the continuity equation as:

$$\frac{\partial \rho}{\partial t} + \nabla \cdot (\rho \mathbf{V}) = 0 \quad (\text{C.6})$$

Which, for incompressible flow i.e. constant density, further reduces to

$$\nabla \cdot \mathbf{V} = 0 \quad (\text{C.7})$$

C.2 Equations of Linear Momentum

In a simliar manner to Appendix C.1 the linear momentum equation for Figure C.1 states:

$$\sum F = \frac{\partial}{\partial t} \left(\int_{\Omega} V \rho d\mathbb{V} \right) + \sum (\dot{m}_i V_i)_{out} - \sum (\dot{m}_i V_i)_{in} \quad (C.8)$$

Again the volume integral reduces to:

$$\frac{\partial}{\partial t} \left(\int_{\Omega} V \rho d\mathbb{V} \right) \approx \frac{\partial}{\partial t} (\rho V) dx dy dz \quad (C.9)$$

The table of momentum fluxes is also constructed in a similar vein to give

Face	Inlet momentum flux	Outlet momentum flux
x	$\rho u V \, dy \, dz$	$\left[\rho u V + \frac{\partial}{\partial x} (\rho u V) \, dx \right] dy \, dz$
y	$\rho v V \, dx \, dz$	$\left[\rho v V + \frac{\partial}{\partial y} (\rho v V) \, dy \right] dx \, dz$
z	$\rho w V \, dx \, dy$	$\left[\rho w V + \frac{\partial}{\partial z} (\rho w V) \, dz \right] dx \, dy$

Table C.2: Table of control fluxes

Introducing these terms into eqns C.8 and C.9 we get

$$\sum F = dx dy dz \left[\frac{\partial}{\partial t} (\rho V) + \frac{\partial}{\partial x} (\rho u V) + \frac{\partial}{\partial y} (\rho v V) + \frac{\partial}{\partial z} (\rho w V) \right] \quad (C.10)$$

taking the term in the square bracket we can write

$$\frac{\partial}{\partial t} (\rho V) + \frac{\partial}{\partial x} (\rho u V) + \frac{\partial}{\partial y} (\rho v V) + \frac{\partial}{\partial z} (\rho w V) = V \left[\frac{\partial \rho}{\partial t} + \nabla \cdot (\rho V) \right] + \rho \left(\frac{\partial V}{\partial t} + u \frac{\partial V}{\partial x} + v \frac{\partial V}{\partial y} + w \frac{\partial V}{\partial z} \right) \quad (C.11)$$

The term in square brackets can be seen to be the continuity equation and so vanishes. The longer term in the round brackets can be seen to be the acceleration of a particle in the control volume and can be written

$$\frac{\partial V}{\partial t} + u \frac{\partial V}{\partial x} + v \frac{\partial V}{\partial y} + w \frac{\partial V}{\partial z} = \frac{dV}{dt} \quad (\text{C.12})$$

and so eqn C.10 reduces to:

$$\sum F = \rho \frac{\partial V}{\partial t} dx dy dz \quad (\text{C.13})$$

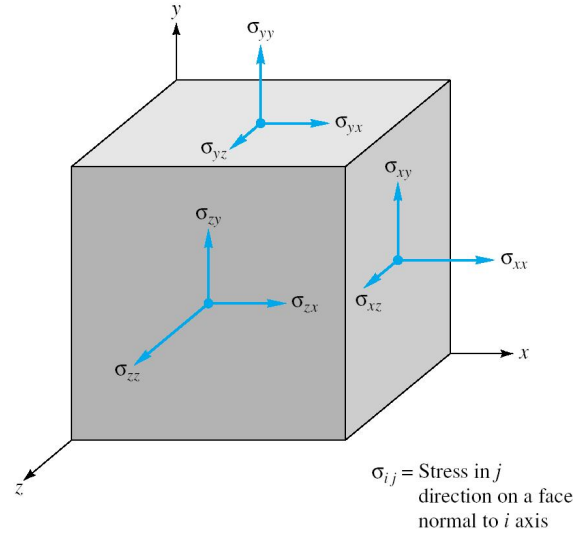


Figure C.2: Notation for stresses

Equation C.13 states the net force on the control volume must be of differential size and proportional to the element volume. These forces are of two types surface forces or body forces. Body forces are due to some external force such as gravity or electrical potential however surface forces are due to stresses on the surfaces of the control volume and are the sum of the hydrostatic stresses and the viscous stresses τ_{ij}

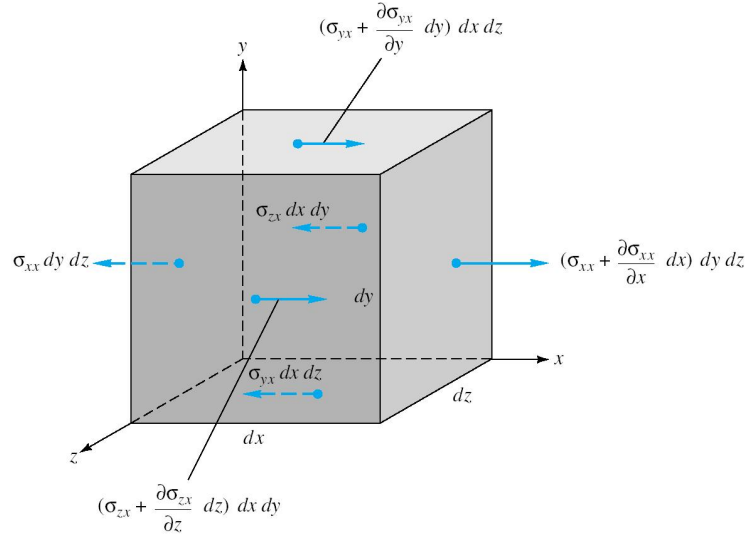


Figure C.3: Control volume showing surface forces in x direction

$$\sigma_{ij} = \begin{bmatrix} -p + \tau_{xx} & \tau_{yx} & \tau_{zx} \\ \tau_{xy} & -p + \tau_{yy} & \tau_{zy} \\ \tau_{xz} & \tau_{yz} & -p + \tau_{zz} \end{bmatrix} \quad (\text{C.14})$$

The notation for which can be seen in Figure C.2 It should be noted that it is not the stresses themselves but rather their gradients that cause the net force on the control volume. This can be seen from Figure C.3 the leftward force $\sigma_{xx} dy dz$ is balanced by the rightward force $\sigma_{xx} dy dz$ on the right face leaving only the net rightward force $(\partial \sigma_{xx} / \partial x) dx dy dz$. This can be repeated for the other two directions resulting in the net force in the x direction being given as

$$dF_{x,surf} = \left[\frac{\partial}{\partial x}(\sigma_{xx}) + \frac{\partial}{\partial y}(\sigma_{yx}) + \frac{\partial}{\partial z}(\sigma_{zx}) \right] dx dy dz \quad (\text{C.15})$$

Substituting in values from eqn C.15 we get

$$\frac{dF_x}{dV} = -\frac{\partial p}{\partial x} + \frac{\partial}{\partial x}(\tau_{xx}) + \frac{\partial}{\partial x}(\tau_{yx}) + \frac{\partial}{\partial x}(\tau_{zx}) \quad (\text{C.16})$$

This can be repeated to give forces in both y and z

$$\begin{aligned}\frac{dF_y}{dV} &= -\frac{\partial p}{\partial y} + \frac{\partial}{\partial y}(\tau_{xy}) + \frac{\partial}{\partial y}(\tau_{yy}) + \frac{\partial}{\partial y}(\tau_{zy}) \\ \frac{dF_z}{dV} &= -\frac{\partial p}{\partial z} + \frac{\partial}{\partial z}(\tau_{xz}) + \frac{\partial}{\partial z}(\tau_{yz}) + \frac{\partial}{\partial z}(\tau_{zz})\end{aligned}\quad (C.17)$$

Combining these equations we get

$$\left(\frac{dF}{dV}\right)_{surf} = -\nabla p + \left(\frac{dF}{dV}\right)_{viscous} \quad (C.18)$$

where

$$\left(\frac{dF}{dV}\right)_{viscous} = \mathbf{i}\left(\frac{\partial\tau_{xx}}{\partial x} + \frac{\partial\tau_{yx}}{\partial y} + \frac{\partial\tau_{zx}}{\partial z}\right) + \mathbf{j}\left(\frac{\partial\tau_{xy}}{\partial x} + \frac{\partial\tau_{yy}}{\partial y} + \frac{\partial\tau_{zy}}{\partial z}\right) + \mathbf{k}\left(\frac{\partial\tau_{xz}}{\partial x} + \frac{\partial\tau_{yz}}{\partial y} + \frac{\partial\tau_{zz}}{\partial z}\right) \quad (C.19)$$

or

$$\left(\frac{dF}{dV}\right)_{viscous} = \nabla \cdot \tau_{ij} \quad (C.20)$$

where

$$\tau_{ij} = \begin{bmatrix} \tau_{xx} & \tau_{xy} & \tau_{xz} \\ \tau_{yx} & \tau_{yy} & \tau_{yz} \\ \tau_{zx} & \tau_{zy} & \tau_{zz} \end{bmatrix} \quad (C.21)$$

Combining equations C.20 C.18 C.4 and by taking the gravity as the only body force acting on the volume i.e. $dF_{grav} = \rho g dx dy dz$ we get

$$\rho g - \nabla p + \nabla \cdot \tau_{ij} = \rho \frac{dV}{dt} \quad (C.22)$$

where

$$\frac{\partial V}{\partial t} + u \frac{\partial V}{\partial x} + v \frac{\partial V}{\partial y} + w \frac{\partial V}{\partial z} = \frac{dV}{dt} \quad (C.23)$$

While equation C.22 looks relatively simple but when expanded to illustrate the inherent complexity looks as follows

$$\begin{aligned}\rho g_x - \frac{\partial p}{\partial x} + \frac{\partial \tau_{xx}}{\partial x} + \frac{\partial \tau_{yx}}{\partial y} + \frac{\partial \tau_{zx}}{\partial z} &= \rho \left(\frac{\partial u}{\partial t} + u \frac{\partial u}{\partial x} + v \frac{\partial u}{\partial y} + w \frac{\partial u}{\partial z} \right) \\ \rho g_y - \frac{\partial p}{\partial y} + \frac{\partial \tau_{xy}}{\partial x} + \frac{\partial \tau_{yy}}{\partial y} + \frac{\partial \tau_{zy}}{\partial z} &= \rho \left(\frac{\partial v}{\partial t} + u \frac{\partial v}{\partial x} + v \frac{\partial v}{\partial y} + w \frac{\partial v}{\partial z} \right) \\ \rho g_z - \frac{\partial p}{\partial z} + \frac{\partial \tau_{xz}}{\partial x} + \frac{\partial \tau_{yz}}{\partial y} + \frac{\partial \tau_{zz}}{\partial z} &= \rho \left(\frac{\partial w}{\partial t} + u \frac{\partial w}{\partial x} + v \frac{\partial w}{\partial y} + w \frac{\partial w}{\partial z} \right) \quad (\text{C.24})\end{aligned}$$

If we assume incompressible flow we can use the following relationships

$$\begin{aligned}\tau_{xx} &= 2\mu \frac{\partial u}{\partial x} & \tau_{yy} &= 2\mu \frac{\partial v}{\partial y} & \tau_{zz} &= 2\mu \frac{\partial w}{\partial z} & (\text{C.25}) \\ \tau_{xy} = \tau_{yx} &= \mu \left(\frac{\partial u}{\partial y} + \frac{\partial v}{\partial x} \right) & \tau_{xz} = \tau_{zx} &= \mu \left(\frac{\partial w}{\partial x} + \frac{\partial u}{\partial z} \right) & \tau_{yz} = \tau_{zy} &= \mu \left(\frac{\partial v}{\partial z} + \frac{\partial w}{\partial y} \right)\end{aligned}$$

to give the differential momentum equation for a Newtonian fluid with constant density and viscosity

$$\begin{aligned}\rho g_x - \frac{\partial p}{\partial x} + \mu \left(\frac{\partial^2 u}{\partial x^2} + \frac{\partial^2 u}{\partial y^2} + \frac{\partial^2 u}{\partial z^2} \right) &= \rho \frac{du}{dt} \\ \rho g_y - \frac{\partial p}{\partial y} + \mu \left(\frac{\partial^2 v}{\partial x^2} + \frac{\partial^2 v}{\partial y^2} + \frac{\partial^2 v}{\partial z^2} \right) &= \rho \frac{dv}{dt} \\ \rho g_z - \frac{\partial p}{\partial z} + \mu \left(\frac{\partial^2 w}{\partial x^2} + \frac{\partial^2 w}{\partial y^2} + \frac{\partial^2 w}{\partial z^2} \right) &= \rho \frac{dw}{dt} \quad (\text{C.26})\end{aligned}$$

These equations are also known as the Navier-Stokes Equations

Appendix D

Flow Detection Software

D.1 Software Overview

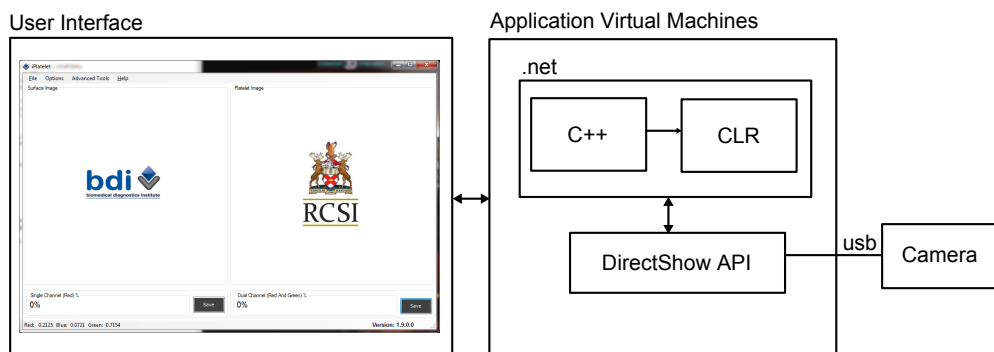


Figure D.1: Block diagram showing software components used to develop image processing software. The user interface talks with the .net framework, from inside a virtual machine, which in turn uses the DirectShow API to acquire images from the camera.

Figure D.1 shown how the difference software block fit together. DirectShow is a multimedia framework and application programming interface (API) produced by Microsoft and is only one part of the grater DirectX framework. The API allows access to perform various operations with media files or streams and can be accessed via native C++ code or through a managed framework such at .net. The DirectShow development tools

and documentation are distributed free of charge as part of the Windows software development kit (SDK) and is compatible with most multimedia hardware . The .NET framework executes in a software environment, known as the Common Language Runtime (CLR) and creates application virtual machines that provide services such as security, memory management, and exception handling. DirectShow allows the programmer to control every aspect of the multimedia hardware through an instance that locks all other software or hardware from accessing the resource.

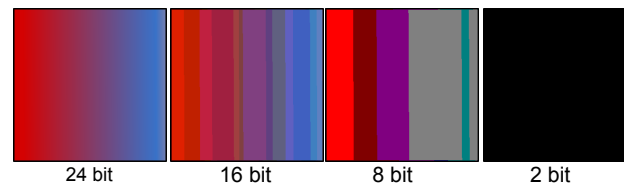


Figure D.2: Demonstration of the effect of changing the resolution has on the same image.

The image output is a bitmap stream of 2, 8, 16 and 24 bit pixels. A 2 bit pixel can represent only 2 colours (binary image) while a 24 bit image in contrast has a colour depth of 16,777,216 colours for each of the three channels red, green and blue (RGB). Figure D.2 demonstrates how detail can be lost when the image is captured using a lower resolution, with a clear loss in detail between 24, 16, 8 and 2 bit pixels. When the colour depth is multiplied by the dimensions of the image the resolution and overall file size can be calculated. The quality of any outputted image and the time it takes to process can require a trade-off between performance and quality and needs to be considered when designing any system, with image resolution, processing power, memory and software all contributing to the overall performance.

Masking Of Image

The software uses a DirectShow compatible high definition camera to record 1 frames/s for a total on 1000s as dye was pipetted into the inlet. The time between pipetting and the fluid starts to flow (the time to start), was recorded. Each image acquired included the number of seconds, since the first frame was acquired and the time was also included in the top left corner of each image allowing for the automated detection of each frame time (t).

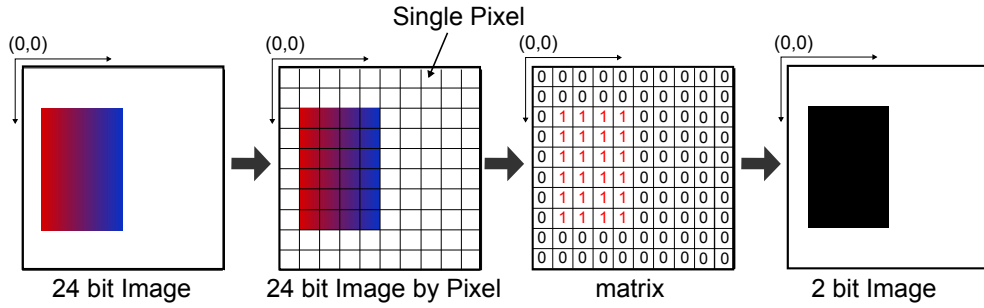


Figure D.3: Example of a 24bit image being converted into a matrix. A threshold is used to select which pixels should be included as part of the feature (1) or set as background (0) within the binary matrix.

Figure D.3 shows how images were individually masked and a binary matrix was created where zero represented a single pixel of background and one a pixel of fluid. When an image is masked each pixel is compared to a predefined threshold value, any pixel below that value is the background, and given a value of 0 (Black), while pixels with a greater value will be classed as part of the object and given a value of 1 (white). The 2 bit image shown in Figure D.3(derived from the original 24 bit image) can be treated as a simple matrix, making it easy to manipulate and fast to process.

D.2 Simple Channel Detection

Figure D.4-A shows two images acquired from the camera at $t=n$ and $t=n+1$. By subtracting the matrixes for time $t=n$ from $t=n+1$ the num-

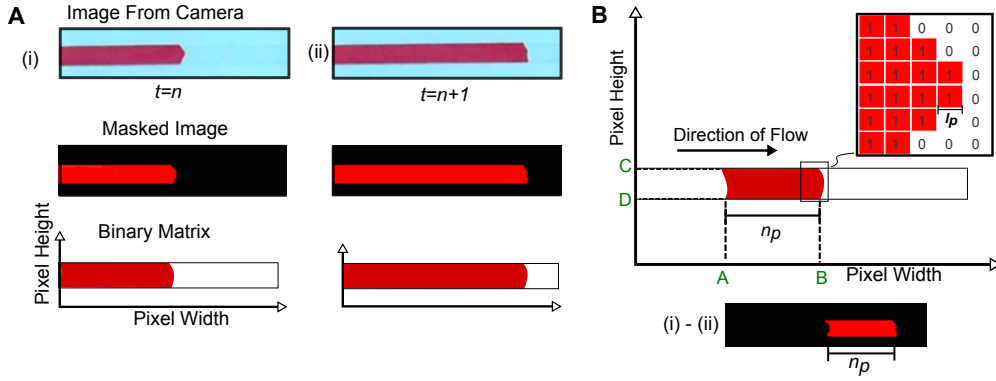


Figure D.4: Conversion of image acquired from camera into a binary matrix. A) (i) Sample image taken at $t=n$ and masked, (ii) Sample image taken at $t=n+1$ and masked. From the masked images a binary matrix is produced and subtracted to determine the n_p (B).

ber of pixels the fluid moved in the direction of flow was converted into a fluid velocity. Where l_p = length of a single pixel in the image. L_{known} = a known length between two points in the image measured in meters (m). $L_{total\ pixels}$ = total number of pixels between the same two points used to calculate L_{known} . V_f = fluid velocity, t = time, a = width of channel (meters) and b = height (meters). The distance $|AB|$ shown on the x axis of Figure D.4-B yields a value for the number of pixels moved n_p :

$$n_p = B - A$$

Therefore, the length of a single pixel in meters is:

$$l_p = L_{known} \div L_{total\ pixels} \quad (D.1)$$

The cross-sectional area equals:

$$A_f = (a \times b)[m^2] \quad (D.2)$$

The fluid velocity equals:

$$v_f = \frac{l_p \times n_p [m]}{t [s]} \quad (D.3)$$

From the velocity and channel cross sectional area (A_f) the flow rate (Q) can be calculated.

$$\begin{aligned} Q &= v_f \times A_f \frac{[m^3]}{[s]} \\ Q &= \frac{l_p \times n_p}{t} (a \times b) \frac{[m^3]}{[s]} \end{aligned} \quad (D.4)$$

The height of channel (a) and width of channel (b) are also a function of the shear rate therefore, the shear Equation 3.1 can be write as:

$$\begin{aligned} \tau_w &= \frac{6\mu}{a^2b} \times \frac{l_p \times n_p}{t} (a \times b) \\ \tau_w &= \frac{6\mu}{a} \times \frac{l_p \times n_p}{t} \end{aligned} \quad (D.5)$$

The software assumed that the inlet remained full so that there was no effect on shear rate caused by the fluid head, while at the same time the fluid flowed continuously from the inlet to the fluid front. The results from the software correlated well when tested against the manual solution. The manual solution required the operated to take measurements from a ruler placed alongside the channel. This comparison was made by manually checking the length the fluid had moved along the channel for each image with that recorded from the software. The software allows for both the manual and automated solution to be used, with the user able to manually measure and review each image before accepting the automated results.

D.3 Complex Channel Detection

The DXF file contains a list of values (appearing one after another within the file), the first describing the data type and the second the value assigned

to that data type. A data type can be broadly classed as containing text or a number, with a total of 1071 used to declare a wide range of objects from the X (20) value of a data point to the colour of a line (62). The subsection ACDBPolyline, contained within ENTITIES, stores a list of vertices and bulges used to create a closed polygon. To demonstrate how effective this system is, a section of text from a DXF file encompassing a single ACDBPolyline is reproduced in Figure D.5.

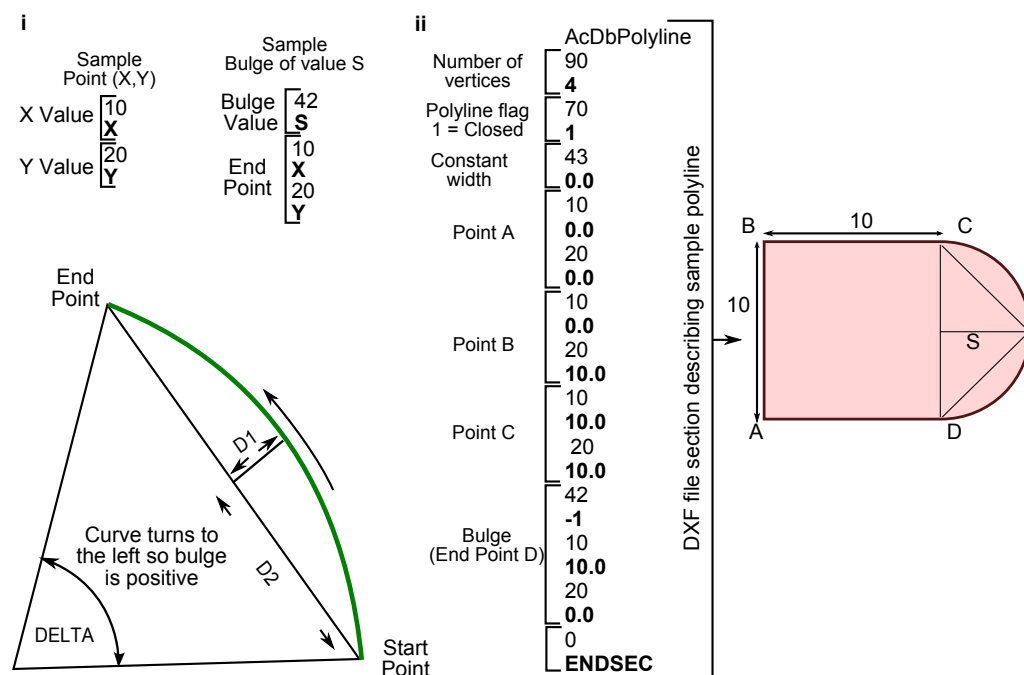


Figure D.5: DXF file section describing a polyline. i) Sample showing how a point and bulge can be described within a DXF file. ii) Part of a DXF file containing the [ACDBPolyline] for a sample shape, with the first three codes containing information about the polyline (90, 70 and 43). While the rest of the text contains the vertices (points) used to draw the shape.

The sample polygon shown in Figure D.5 consists of a 10×10 square and a single bulge from point C to D. Once the polygon is set-up the point A is introduced as the start of the polygon before B and C are declared. The start point of the bulge is the last declared point (in this case C) while the end point is included within the bulge declaration. The bulge is the

tangent of one fourth the included angle for an arc segment, made negative if the arc goes clockwise from the start point to the endpoint. A bulge of 0 indicates a straight segment, and a bulge of 1 is a semicircle. The bulge shown in Figure D.5 is a semicircle and the closed polygon [A, B, C, D, A] is drawn clockwise, therefore the value for this bulge (data type 42) is -1. Once the value equals ENDSEC the ACDBPolyline has ended (when the polygon is closed) the last point and first point are the same, when the closed flag is set to 1 within the polygon definition. Once the polygon has been extracted from the file the user can scale the shape to fit over the channel using software developed to determine the flow rate.

DXF Stencil

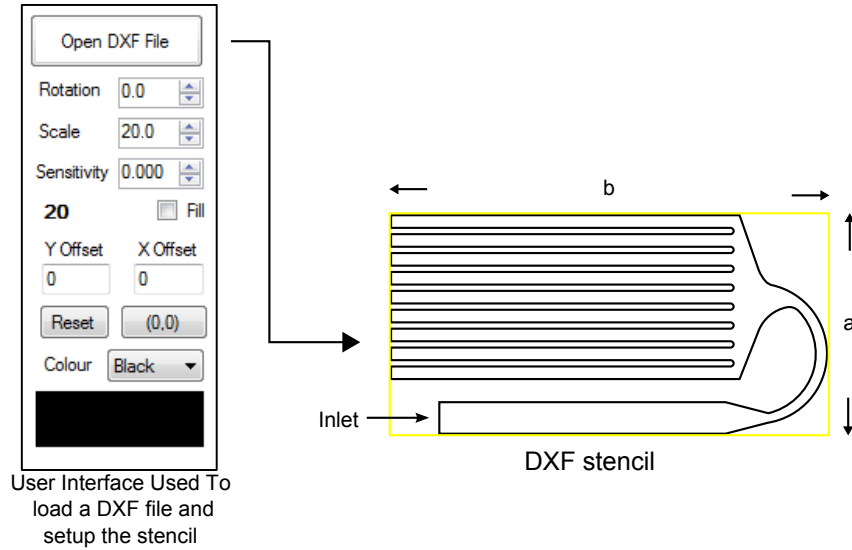


Figure D.6: User interface and sample DXF stencil.

Once the polygon has been extracted from the file a rectangle is drawn around the polygons extent to define the minimum required area for a given stencil, this area is used to crop the image. The stencil defines the area within the channel that can be filled with fluid. Figure D.6 shows a sample stencil for a channel with a single inlet, alongside a user interface used to set-

up the stencil. From the user interface the channel can be scaled, rotated, inverted and coloured to make it easier to see against differed backgrounds. Figure 3.5 shows how the stencil can be placed over the image acquired for the camera and a series of regions extracted.

Appendix E

Mini Individual Platelet Adhesion (MiPA) Unused Chip Designs

E.1 Movement Of Rocking Table

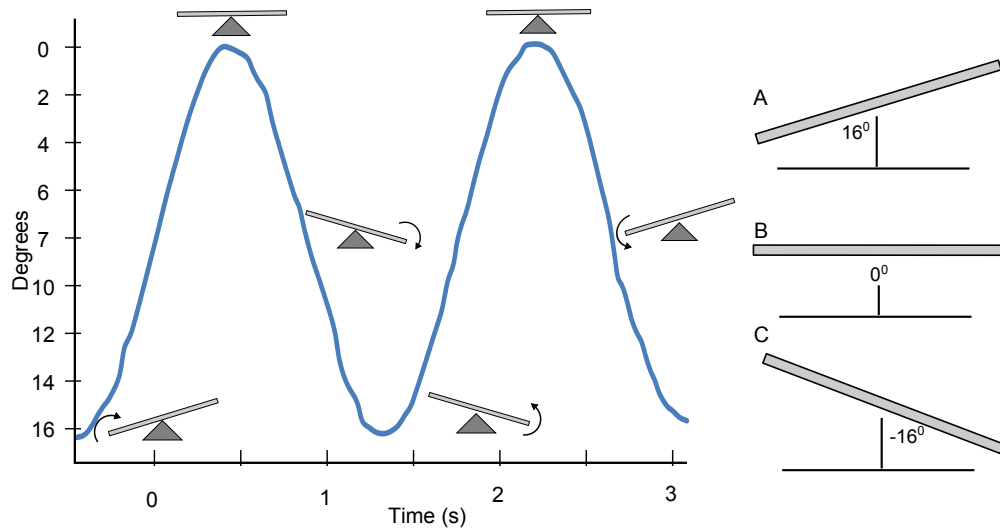


Figure E.1: Rocking table oscillation $\pm 16^\circ$.

The movement of the rocking table was also recorded using software

developed in Java, with the sensors available on a smart phone. Figure E.1 show the table top moving through a full oscillation, starting at 16° before the table returned to the flat (0°), moving through to -16° before returning back to -16° . Data was recorded for 5 minutes at a number of different oscillations per minute and showed smooth, reproducible, oscillations across all speeds tested. Using the accelerometer sensor a maximum acceleration of 0.05 m/s^2 was recorded for a speed of 30 oscillations per minute rising to 0.15 m/s^2 for 100 oscillations per minute, all data was recorded at the centre of the table. A height of 0.85 mm was calculated for a volume of $50\text{ }\mu\text{l}$ of blood 0° , a minimum height of 0.22 mm was calculated at $\pm 16^\circ$. This change in height was expected as the blood is only flowing with the aid of gravity (see Section 2.1.3) and as $50\text{ }\mu\text{l}$ was already selected a low volume and high volume (maximum fluid height of 0.73 mm) well was tested to determine if the change in height would affect the resulting % of occupied spots.

E.2 Comparison of Substrates Used With iPA

A comparison was made between the optimised MiPA and iPA assays on both a glass and zeonor substrates to determine if there was a difference between the % platelet adhesion across the two assays. The Zeonor substrate was tested as it has a number of advantages over the glass substrate currently used, its low cost, availability in any size, ability to be cut to shape, optical properties and the removal of any possible sharps injury (associated with glass) make it ideal for use in a point-of-care device. The Health Service Executive (HSE) requires that any new devices meet certain requirements. The term “sharp safe” refers to the removal of any glass or needles that by cause injury from the device. The results from Figure E.2-A and B indicate Zeonor can be substituted for glass without any significant fall off in perfor-

mance across both assays, there was also a smaller % adhesion achieved by the MiPA on both substrates when compared to iPA. This difference may be explained by the volume of blood used for each assay, or as a result of the way the blood moves across the surface.

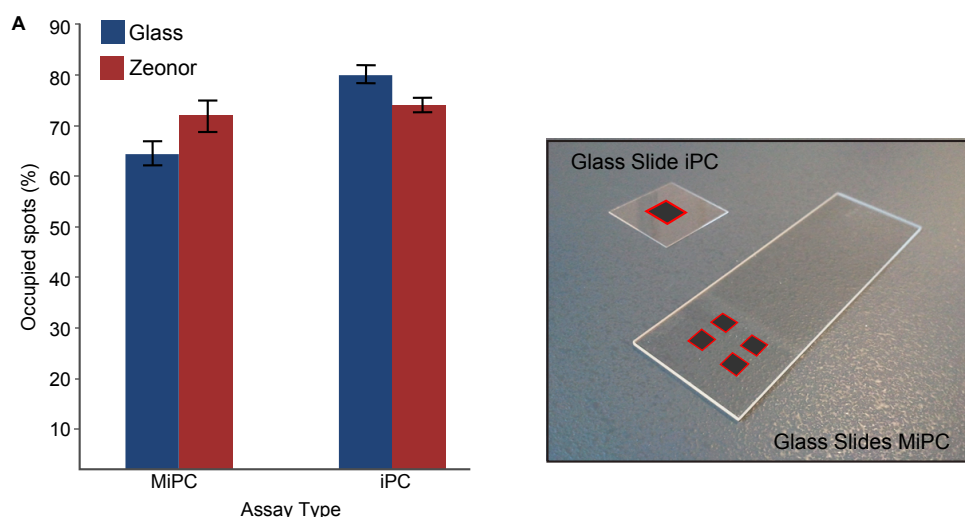


Figure E.2: Comparison of substrates used in both MiPA and iPA. (A) Comparison of glass and Zeonor to determine if a change in substrate material would have a meaningful effect of % platelet adhesion, no significant difference between the two was recorded, with a smaller % adhesion when MiPA is compared to iPA. The glass cover slid and glass slide used, with the area of printed 6 μm spots (in red) is also shown.

E.3 Integrated Chip Designs

The gen1 closed chip consists of seven layers, three of PMMA, three PSA gaskets used to create the well assembly (layers 2, 3 and 4) and filling assembly (layers 5, 6 and 7) and one Zeonor substrate (Figure E.3). The two sub-assemblies are adhered together before the monovette connector (8) and Zeonor substrate (1) are added to create a fully assembled chip. The blood passes through the connector which is secured in place between layers 7, 6, and 5 before passing into the channels within the filling layer (4), the

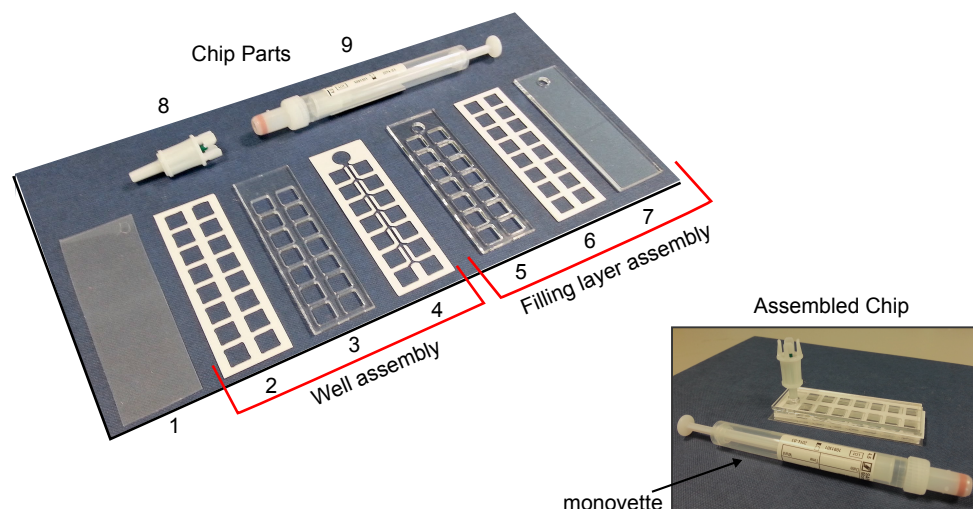


Figure E.3: First generation closed chip layers. Seven layers make up the closed version of the gen1 chip starting with the Zeonor layer cut to size from a bigger sheet, (2) pressure sensitive adhesive (PSA) gasket between the Zeonor and the assay wells, (3) assay wells laser cut from PMMA, (4) PSA filling layer, (5) PMMA spacer layer, PSA gasket between spacer and top layer, (7) PMMA top layer, (8) monovette connector, (9) monovette syringe. The assembled chip is also shown with the transparent PMMA layer and the white PSA gasket and filling layer along the syringe.

two nearest wells are filled first before the blood starts to fill the next two wells, once all wells are full the chip was rocked for 30 minutes. The initial results showed zero % platelets adhered to the 6 μm spots indicating that further optimisation of blood volume may be required.

Version 1

The First of these is shown in Figure E.4 and is made up of 6 layers with a PSA gasket between each one, unlike the gen1 closed chip the fill layer was made from PMMA along with layer 1, 2, 4, and 5. A green dot shows where fluid passes from one layer to another through the delivery layer into the assay wells below and into the volume indicator wells located to the right of the chip. The fluid enters the filling layer and starts to fill the four well

Appendix E. Mini Individual Platelet Adhesion (MiPA) Unused Chip Designs

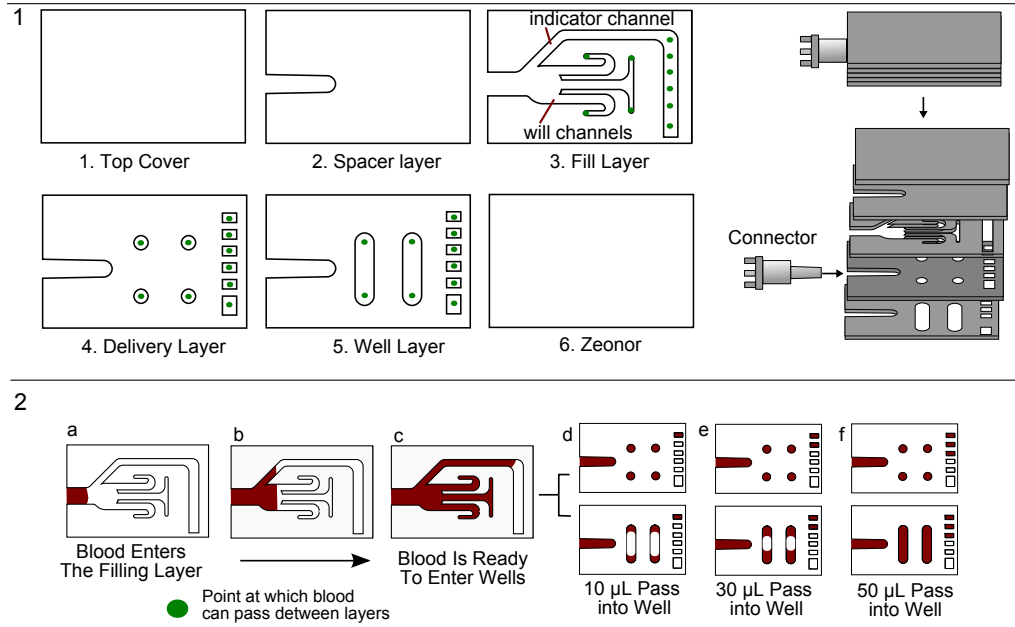


Figure E.4: Version 1 of the second generation design. The layers shown exclude the PSA gasket between each. As the connector was moved to the side of the chip an additional spacer layer was required. The progress of flow is also shown, starting as the blood leaves the connector and moves along the filling layer before reaching the inlets into the assay well and indicator well at the same time, with the 10 μl filled by the first indicator well and 20 μl of blood added to the assay well by each subsequent well filled.

channels along with the volume indicator channel with the fluid reaching the end of the well channels and the first indicator well at the same time, as the volume of fluid each channel can hold is equal. At this point the fluid passes through the delivery layer and into the wells below with the first indicator well holding 10 μl and each subsequent indicator well holding 20 μl of fluid the user can deliver fluid in increments of 20 μl to the assay wells. This difference is to account for the length of channel the fluid must move before reaching the next indicator well, resulting in a maximum possible user error of 10 μl between each indicator well.

When this design was tested with water the overall performance was excellent with each well filling with the same volume of fluid. However, when whole blood was introduced its increased viscosity caused it to favour

filling the indicator channel over the assay wells as there was no need to pass through the holes within the delivery layer to reach the assay wells. Even when these holes were increased in size there was no improvement to chip performance with the assay wells only beginning to fill when the indicator channel had nearly completely filled with blood. To address these issues the chip was redesigned and a holding well introduced as the blood exited the connector.

The gen1 chip introduced the intergraded monovette connector for loading of the sample directly from a syringe through a PSA filling layer within the chip. When the connector was inserted into the chip it would tend to touch the PMMA layer below causing the chip to delaminate and blood to leak between the layers of the chip. The 50 μm filling layer made adjusting the height of the connector which was simply pushed into place in such a way as to prevent delamination and allow the blood to flow into the fill layer, without additional leaking around the inlet from a loose fit. There was also a difficulty associated with laser cutting the smaller features around where the blood flowed into the assay wells. The results from the gen1 chip show a number of important shortcomings in its design, in terms of volume delivery, fluid flow and manufacturability of a first stage prototype. The chip created a good foundation for the development of the second generation of chips with a requirement to further optimise of fluid flow within the assay well in an effort to increase % adhesion and a method to deliver the required blood volume to the assay well all within the confines of a closed chip.

Version 2

By moving the connector to the top of the chip from the side the need for a spacer layer was removed, this reduced the chance of leakage around the connector, materials used and the overall assembly time as an interference

Appendix E. Mini Individual Platelet Adhesion (MiPA) Unused Chip Designs

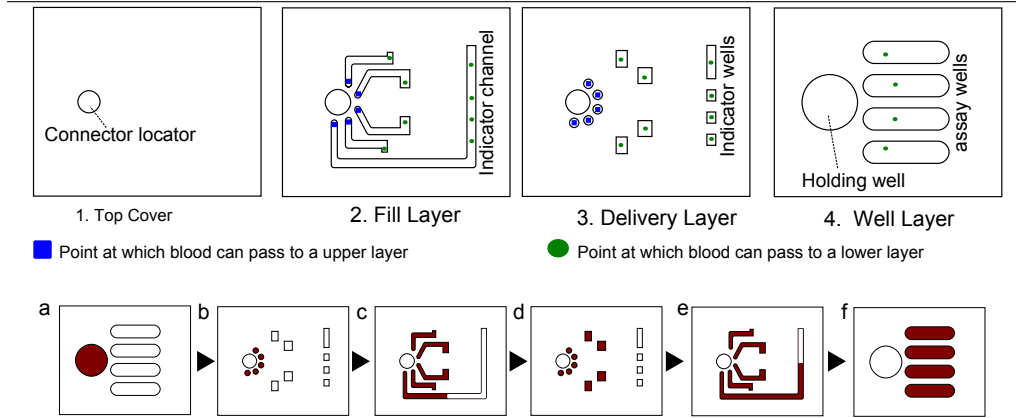


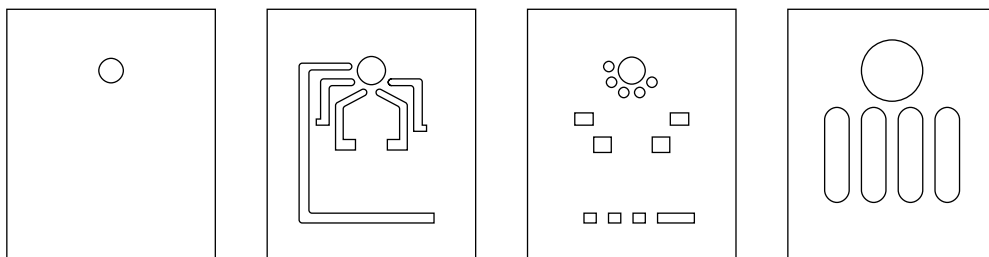
Figure E.5: Version 2 of the second generation design. The layer shown excludes the PSA gasket between each. The connector has been placed at the top of the chip removing the need for a spacer layer. The progress of flow is also shown, starting as the blood enters the holding well reaching the inlets into the delivery layer at the same time, before moving along the filling channels to the outlets of the delivery layer and faintly into the assay wells.

fit could be used. The holding well is an important component of this design and allows for blood to be delivered to the four filling channels and the indicator channel at the same time with an equivalent resistance to flow. As the fluid fills the holding well it remains level filling the bottom of the well first, with the viscosity of the fluid preventing it from entering the delivery layer before the well is completely full (Figure E.5). As the filling well is ten times the size of the outlet within the delivery layer the hydraulic force acting on each outlet is equal (assuming equivalent resistance to flow through each outlet) causing each channel to fill at the same rate. The fluid is now free to fill each assay well with the same volume as that within the indicator channels with a minimum delivery of $35 \mu\text{l}$ of fluid. This design performed very well with water but again experienced issues with some blood samples as air within the sample prevented the holding channel from filling completely or in some cases bubbles blocking the outlet. If additional force was applied to the syringe the bubbles could be displaced with the effect that some wells would fill more than others, making the indicator a

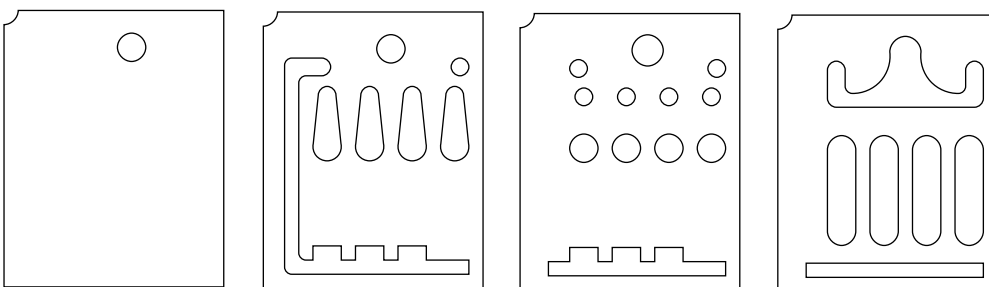
useless guide.

Many of the features found within the earlier iterations of the chip can be seen within the final chip design. Figure shows the layers for three versions of the chip, with the smaller rectangular well used for these designs.

Version 4



Version 5



Version 6

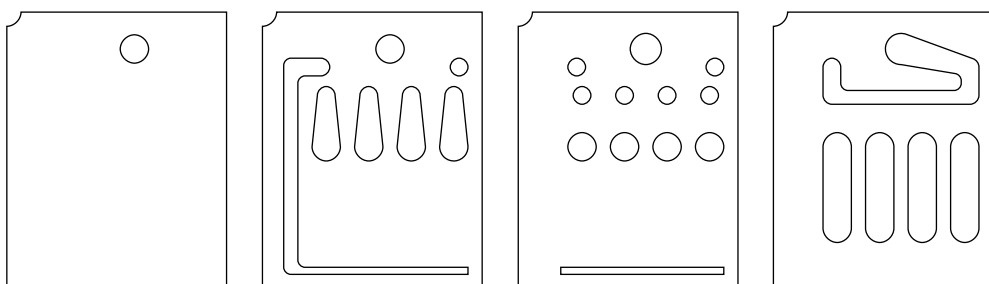


Figure E.6

Appendix F

Detection Software Principles

F.1 Blob Analysis

Blob analysis allows for each object or region within an image to be individually identified according to a predefined threshold. An analysis technique is applied to a given image to determine which pixels make up the object, a blob is therefore a list of these pixels. The blob itself has no properties and requires further post-processing before any useful information can be determined. Laplacian (Laplace) of Gaussian (LOG) is one of the most commonly used techniques, a Gaussian blur is first applied to the image before the Laplace filter can be applied. The Laplace filter is less sensitive to noise if the image is first blurred, without the blur many small blobs can be created thereby taking pixels away from the objects within the image and creating many useless fragments. The Laplacian $L(x, y)$ for a given image with pixel intensity values is given by:

$$L(x, y) = \frac{\partial^2 I}{\partial x^2} + \frac{\partial^2 I}{\partial y^2} \quad (\text{F.1})$$

A convolution kernel can be used to approximate the second derivatives

within Equation F.1 using:

$$\begin{bmatrix} 0 & -1 & 0 \\ 0 & 4 & -1 \\ 0 & -1 & 0 \end{bmatrix} \quad \begin{bmatrix} -1 & -1 & -1 \\ -1 & 8 & -1 \\ -1 & -1 & -1 \end{bmatrix} \quad (\text{F.2})$$

Equation F.2 convolution show two commonly kernels used discrete approximations to the Laplacian filter, started in the left corner the kernel is slid over the image as to move through all positions within a given image. Each kernel position corresponds to a single output pixel, the value of which is calculated by multiplying together the kernel value and the underlying image pixel value for each of the cells in the kernel (Equation F.3).

$$I = \begin{bmatrix} I_{11} & I_{12} & I_{13} & I_{14} & I_{15} & I_{16} & I_{17} \\ I_{21} & I_{22} & I_{23} & I_{24} & I_{25} & I_{26} & I_{27} \\ I_{31} & I_{32} & I_{33} & I_{34} & I_{35} & I_{36} & I_{37} \\ I_{41} & I_{42} & I_{43} & I_{44} & I_{45} & I_{46} & I_{47} \\ I_{51} & I_{52} & I_{53} & I_{54} & I_{55} & I_{56} & I_{57} \\ I_{61} & I_{62} & I_{63} & I_{64} & I_{65} & I_{66} & I_{67} \end{bmatrix} \quad K = \begin{bmatrix} K_{11} & K_{12} & K_{13} \\ K_{21} & K_{22} & K_{23} \\ K_{31} & K_{32} & K_{33} \end{bmatrix} \quad (\text{F.3})$$

Using the image matrix (I) and kernel matrix (K) (shown in Equation F.3) an output pixel P can be calculated , take I_{45} as an example:

$$\begin{aligned} O_{45} = & I_{45}K_{11} + I_{46}K_{12} + I_{47}K_{13} + I_{55}K_{21} + I_{56}K_{22} + I_{57}K_{23} \\ & + I_{65}K_{31} + I_{66}K_{32} + I_{67}K_{33} \end{aligned} \quad (\text{F.4})$$

If the image has M rows and N columns, and the kernel has m rows and n columns, then the size of the output image will have $M - m + 1$ rows, and $N - n + 1$ columns, allowing the convolution to be written as:

$$O(i, j) = \sum_{k=1}^m \sum_{l=1}^n I(i + k - 1, j + l - 1) K(k, l) \quad (\text{F.5})$$

where i runs from 1 to $M - m + 1$ and j runs from 1 to $N - n + 1$.

As the Kernels are approximating a second derivative measurement on the image they are very sensitive to noise. While the Gaussian smoothed can be performed separately it is possible to combine both the equations and thereby Increase the performance of an image processing system as only a single calculation is required per pixel (Equation F.6).

$$LoG(x, y) = -\frac{1}{\pi\sigma^4} \left[1 - \frac{x^2 + y^2}{2\sigma^2} \right] e^{-1 - \frac{x^2 + y^2}{2\sigma^2}} \quad (F.6)$$

Equation F.6 can also be approximated by a 7×7 kernel. For most real time image processing applications the kernel is typically slid to all pixels within the array, this will result in no corresponding value for some kernel positions at the edge of the image. However, as no values are available for the rest of the kernel (now outside of the image) there can be some distortion at the side and bottom edges of the output. It is however beneficial to use all positions within the array, as the resulting output image is of the same size.

By applying a zero crossing detector to the output it is possible to create a binary image highlighting features. A zero crossing detector looks for places in the Laplacian output of an image where the value of the Laplacian passes through zero (change in sign). These changes occur in an area where there is a big difference in intensity and normally denote the edge of an object, but this is not always the case and requires additional post-processing to determine which feature can be treated as a blob or which feature is noise. From the output image it is possible to determine different blob features including the object area, centre of gravity, rectangle size and if the blob is a standard shape. The iPlatelet software uses basic filters adapted from the AForge .net framework available under General Public License (LGNU V3).

The result of applying a Gaussian blur, to a region of an image containing platelets adhered to a surface is shown in Figure F.1-B. While the blur has the effect of removing noise and thereby limiting the number of features to be investigated, there are three platelets missing from the output (highlighted within the red boxes). As these platelets have a low intensity the blur moves these pixels into the same value range as a background pixel. Although these platelets are somewhat visible in Figure F.1-A, there is also a lot of noise visible making the output difficult to work with. Figure F.1-C attempts to solve this problem with the addition of two pre-processing filters. First a scaling filter is applied to increase the intensity of each platelet, before a mid-pass filter (MPF) is applied to the input image. By setting any pixel below a set value to 0 and any value above a set value to a pre-defined maximum the MPF filter can reduce noise and decreases the intensity of platelets that may saturate the image.

While two of the three platelets are now visible, within the red box in Figure F.1-C, the filters were unable to detect the platelet of the lowest intensity. For the iPlatelet software the lower boundary of the MPF was reduced to allowing non-platelet features to be included within the output, thereby requiring a feature selection step to be added in post-processing.

F.1.1 Spot Region Detection

The rotation of the stamp during the μ -contact printing process does not affect the results when calculating the % occupancy, when using the matched feature methods. However, as SLD only needs a single image there is no way to determine if a spot is missing or badly-printed without a pre-defined reference, required to match the expected location of each point within the array to a blob extracted from the input image. By using the four crosses encapsulating a 13×13 array of spots as processing markers, the

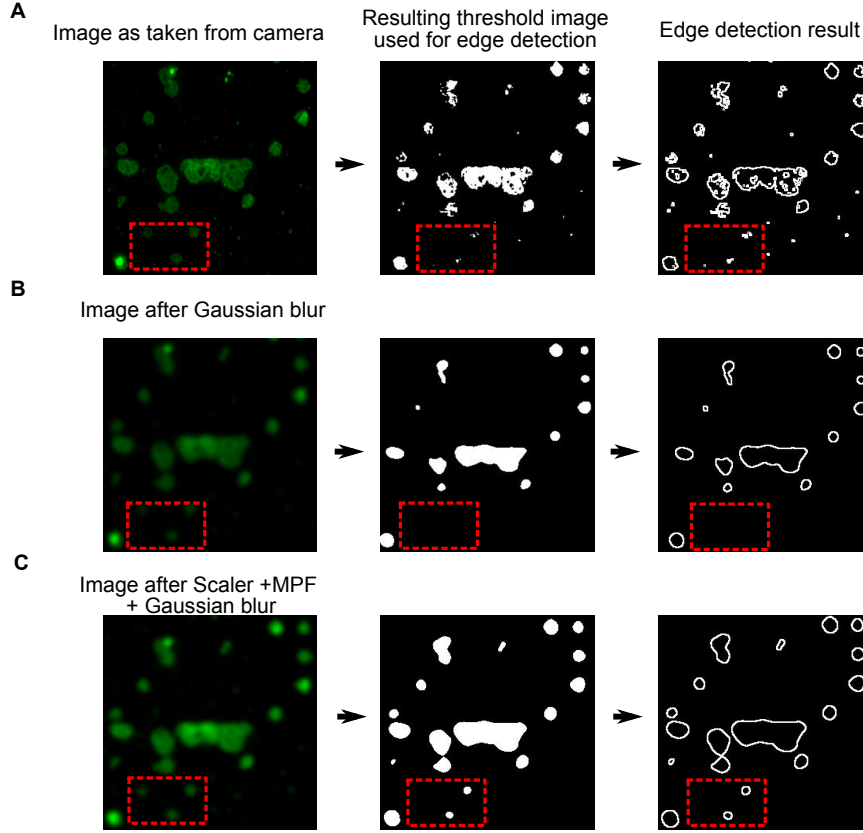


Figure F.1: The effects of applying a Gaussian blur to a sample region of a platelet image. 1. Unfiltered region, 2. region after Gaussian blur, 3. region after Gaussian blur, scaling filter and mid-pass filter (MPF) is applied. The effects on the output image are shown when both a threshold filter and edge detection are applied, with an area of the bottom left hand corner (highlighted in red) used to demonstrate some common issues with blob detection.

rotation of the array and therefore the expected location of each spot, can be calculated. Figure F.2-A shows the 13×13 array at 0° and rotated by an angle θ and the four process markers surrounding it. As the arrays are printed next to each other a marker is shared by up to four arrays of spots requiring the software to process 1 to n number of arrays within a single image. The centroid for each of the four crosses is first determined and an id is assigned (a, b, c and d), using these four centroids a centre point (O) for a given array can be calculated. By determining the angle between two lines,

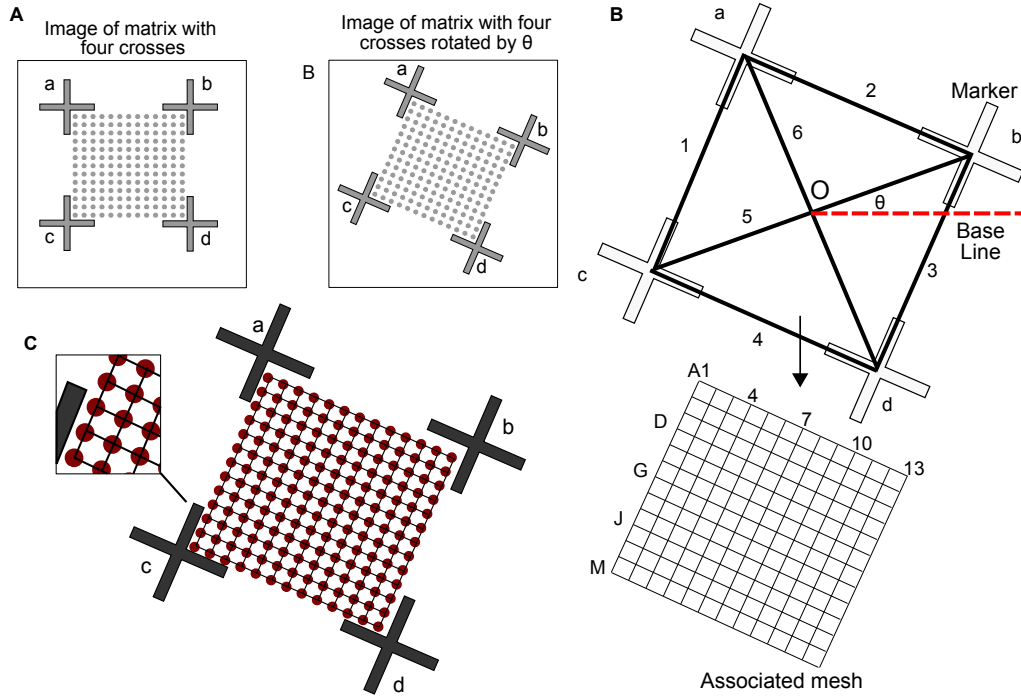


Figure F.2: Details how a mesh is built and fitted to an input image to account for image rotation. A) shows two arrays of spots along with the crosses used as image processing markers, with one array rotated by an angle θ . B) illustrates the lines used to calculate the rotation and therefore the spot locations, an associated mesh is also shown and numbered. C) demonstrates how a mesh is laid over the input image to extract the region around each spot.

starting at each of the four markers and intersecting at the centre point O , both the rotation and quality of the resulting mesh can be calculated. If one of the four markers has not been correctly printed or is not fully shown within an image, the centre of gravity for the marker will move resulting in the array failing quality checks and being excluded from the calculated % occupancy. The resulting mesh is shown in Figure F.2-B and is made up of a grid with each intersection representing a the location of a spot, the mesh is built in real time for each image thereby automatically being scaled for the magnification used with the microscope.

List of Figures

1.1	A cross-section of a vessel with vascular damage showing platelets in their different states of response seen during vascular injury. .	3
1.2	Light Transmission Aggregometry	6
1.3	PFA-100 [®]	8
1.4	(A) Whole blood is first loaded into the well.(B) The cone is lowered into the well and rotated and the blood sheared. (C) The plate is then washed and the platelets stained. (D) The platelets can now be imaged.	9
1.5	VerifyNow [®] cartridge	10
1.6	(A) vacutainer is connected. (B) A vacuum pumps the blood into the staging well. (C) Blood is moved from the staging well into the detection wells. (D) Blood is mixer bead to help the aggregation of platelets.	11
1.7	Whole blood is incubated on a substrate array of platelet-specific protein. Single platelets adhere to the protein spots, creating arrays of single platelets on the substrate and the percentage adhesion is quantified by use of fluorescence microscopy.	14
1.8	Use of labelling within the iPA assay. 1) cy3 label used to label the 6 μm fibrinogen spots, arrayed in squares of 13 \times 13. 2) Image of platelets adhered to spots, labelled with Alexa-488 and visible under FIFC filter.	15

1.9	Excitation and emission wavelength values for fluorescent dyes uses as part of the iPA assay, Alexa-488 and Cy3 are shown.	16
1.10	Steps required to fabricate microfluidic channels using photolithog- raphy. (1) The wafer is cleaned and readied for use in pho- tolithography. (2) A photoresist is then deposited onto a sub- strate. (3) The mask is applied along with a light source, to transfer the pattern onto the wafer. (4) Development. (5) Etch- ing. (6) Resist removal.	23
1.11	Lamination technologies. A) Types of PSA. B) Lamination through pressure and temperature. C) glass substrate laminated with PSA.	24
1.12	Technique to allow both single and multi-layer μ scale structures.	25
2.1	Diagram showing the relationship between apparent viscosity of normal blood, plasma at various shear rates made [6].	39
2.2	Flow between parallel plates.	40
2.3	Velocity profiles through rectangular ducts of varying aspect ratios.	42
2.4	Permeability of PDMS slab. Two views of a channel inside a PDMS slab are shown to demonstrate the diffusion of air into the material. The important values used to calculate the flux are also labelled.	44
2.5	A) Channel at zero degrees ($h = h_0$). B) Channel at θ therefore $h = h_f$	47
2.6	Viscous flow down an inclined plane.	49

3.1	Principle and of degas-driven flow device. A) Assembly of DDF device using PDMS slab and poly(cycloolefin) (COP) sheet. B) Principle of DDF flow shown in a single length channel. i) Diagram of a section of the channel with a total length (L) as the fluid enters and the air starts to degas at $t = 0$. ii) Diagram of a section of the channel after the flow has moved a length dx along the total length (L) thereby reducing the available channel by $x - dx$	56
3.2	Preparation of PSA mould for manufacture of PDMS Chip. A) The location of the GraphTec cutter blade and housing are shown along with the backing sheet. B) Shows the four steps required to remove the channel from the waste PSA and roll it onto the surface of a petri dish.	58
3.3	Microscope Images (20x magnification) of (A) PSA the mould alongside an image of (B) the channel in PDMS chip created from the mould.	59
3.4	Calculation of flow rate using acquired images	60
3.5	Screen shot of software used to calculate flow rates for a complex channel using a DXF file. 1-2) The imported DXF file is shown in a yellow box, the box is placed over the image before a threshold is applied. 3) The DXF stencil is applied to the threshold image which sets any pixel outside of the channel to 0 (black) and at the same time crops the image to the stencil size. 4) Image of the stencil and a series of cropped images showing how only the area within the channel is extracted from each image.	62
3.6	Simple and complex flow rate detection methods compared. . .	63
3.7	PDMS Mixing. The PDMS is first mixed (10:1) before it can be poured into the mould and heated at $70^{\circ}C$ for 60 <i>min</i> . Once cured, the slab can now be removed and cut to size.	64

3.8	A) Percentage of channel filled after 1000s for both sets 1 and 2. B) Example of the flow rate profile for the first 1000s of flow in a DDF device split into three stages.	67
3.9	Comparison between devices with equivalent footprint areas. The maximum flow rate across different footprints (A), the flow rate after 500 seconds (B) were plotted. Set 1 includes channels of widths 1 <i>mm</i> to 4 <i>mm</i> while Set 2 includes channels 20 <i>mm</i> to 80 <i>mm</i> . As a channel id 4 is included in both sets of data only one column is shown. Each figure has an n=7.	68
3.10	The maximum shear rate for the two sets is shown. The max shear rates increase with the increase in length while the shear rate remains constant when the width is increased from 1 to 4 <i>mm</i> .	70
4.1	A semantic of three devices device designed to compare the shear rate in both water and blood. $n = 4$	75
4.2	A) Shear rate observed in devices containing 2,3 and 4 legs after 7min amount of flow of water. B) Shear rate observed in devices containing 2,3 and 4 legs after 7min amount of flow of blood. $n = 5$ for both water and blood.	76
4.3	The % of occupied spots for 5 <i>mm</i> PPF channel at 20, 50, 100, 150 s^{-1} alongside the results for the iPA assay. $n = 5$	78
4.4	The % of occupied spots for 5 <i>mm</i> PPF channel when the array was printed at the inlet, centre and outlet. $n = 7$	79

4.5	Optimisation of conditions in the parallel plate flow devices for platelet adhesion to surface coated 6 μm spots of fibrinogen. (A) Adhesion of platelets (% occupied dots) to 6 μm dots of fibrinogen measured after 9 mins of blood flow in parallel plate flow device containing channel widths of 4, 5, 6 and 7 mm at a shear rate of 20 s^{-1} ($n = 5$). (B) Time-dependent adhesion of platelets (% occupied dots) to 6 μm dots of fibrinogen using 6 mm wide channel at a shear rate of 20 s^{-1} ($n = 5$).	80
4.6	2-D representation of the six channel designs created with 1, 2, 3, 6, 7 and 9 legs each of 2 mm width. The green square shows the location of the 6 μm spot array, along the 6 mm width test area. The array contains 24336 spots made up of 144 blocks of 13×13 spots.	81
4.7	Shear rate profile for 9 leg device. The shear rate decreases from a high of approximately 120 s^{-1} to 10 s^{-1} after 8 minutes. The shear rate stays between 100 s^{-1} and 20 s^{-1} for 5 minutes which is between the range of shear rates determined with the use of parallel plate flow for adhesion of platelets to 6 μm spots. $n = 7$	82
4.8	(A) Detection of <i>in-vitro</i> $P2Y_{12}$ inhibition using DDF device. Platelet adhesion to fibrinogen dots (% occupied spots) in 3 separate blood draws on separate days for a single healthy donor with no agonists with 20 μM ADP, and with 20 μM ADP in the presence of 10 μM cangrelor, which effectively abrogates the ADP effect, demonstrating detection of $P2Y_{12}$ inhibition. Error bars represent standard deviations for the 3 separate blood draws. (B) Photos of the chip during flow and a picture of platelets adhered to the spots used to calculate the % adhesion are shown in Figure4.8-B.	84

5.1	Open square well chip compared with current assay. (A) The seesaw rocking table used in the current iPA assay can hold 25 samples, the equivalent to only two square-well chips. (B) The chip fits on a standard glass slide chip and contains 14 or 16 wells in two rows of 7 and 8, respectively. (C) A 16 well chip filled with 25, 50 and 100 μl of blood shows how 25 μl fails to cover the surface of the well and 100 μl fills the well completely, thereby preventing the blood from moving over the surface. . . .	91
5.2	Optimisation of chip. (A) Five different volumes of blood were tested from 100 to 25 μl within the well of the chip and the % platelet adhesion recorded for each volume, with the highest achieved at 50 μl . (B) With the volume optimised the effect of rocking speed on platelet adhesion was tested at 30, 60 and 100 oscillations per minute with 50 μl of blood.	93
5.3	Detection of <i>in-vitro</i> $P2Y_{12}$ inhibition using square wells (50 μl of whole blood per well). Platelet adhesion to fibrinogen dots (% occupied spots). The three columns show the result for untreated whole blood, blood treated with an agonist (20 μM ADP), and ADP in the presence of 10 μM Cangrelor (which effectively abrogates the ADP effect). This is the same agonist and drug shown in Figure 4.8.	95
5.4	Effects on % platelet adhesion as a result of changes to flow length. (A) The square well at both 0° and 45° and the difference in flow length. (B) Effects on % platelet adhesion for a square well placed at both the middle and edge of the table, at an angle of 0° and 45°	96

5.5	Comparison between open and closed chips. The assay wells of both the open and closed versions of the chip were loaded with 50 μl and 110 μl of blood and the % of occupied spots recorded. The corresponding images of the protein spots and the platelets adhered to these spots are also shown.	98
5.6	Effects of channel shape on platelet adhesion. Five different shaped wells were tested each with different flow lengths, results shown are for wells at their maximum flow length. The maximum % platelet adhesion was recorded for the small rectangle. One of each well type (numbered 1-5) was tested using the same whole blood sample, this was repeated five times (n=5) with a total of 25 chips tested	99
5.7	Optimisation of blood volume within rectangular well. Four different volumes of blood were tested from 70 μl to 100 μl in increments of 10 μl for both an open and closed well. No statistical difference in the % of occupied spots was recorded for the open well.	100
5.8	Optimisation of flow length. A channel with the same flow length as the petri dish (38 mm) is compared alongside a glass slide and APTES treated Zeonor (shown in red). The 17 mm (Well 5) long channel is the same as that shown in Figure 5.8.	101
5.9	A) iPA assay compared to research chip filled with 100 μl , 150 μl and 200 μl of blood. B) Pictures illustrating how the chip is filled and the flow length of the iPA assay and chip can be compared.	102
5.10	A) Comparison between iPA and COiPA. B) The detection of <i>in-vitro</i> P2Y ₁₂ inhibition using the research chip. B) Platelet adhesion to fibrinogen dots (% occupied spots) in 4 healthy donors in whole blood, whole blood + 20 μM ADP, and with ADP in the presence of 10 μM Cangrelor. (n = 5)	104

5.11	Monovette System used with device.	105
5.12	The final version of the chip. (A) The four layers that make up the chip excluding the Zeonor substrate and PSA gaskets. (B) A detailed view of each layer with the important features indicated.	105
5.13	The finish chip and how blood is loaded using the syringe to fill the staging wells.	107
5.14	Detection of <i>in-vitro</i> P2Y ₁₂ inhibition using the integrated chip. Three chips used with four wells per chip.	108
6.1	Snapshot of window used to manually count adhered platelets to 6 μm spots. The image was captured from within the iPlatelet software, with the image of arrayed fibrinogen displayed on the left and the platelet image to the right of the window.	116
6.2	Snapshot of window used to calculate the % occupancy for a single image set using the automated matched feature method (AMFM). The image was captured from within the iPlatelet software. The image of arrayed fibrinogen is displayed on the left and the platelet image to the right of the window. The platelets are marked with a green dot while the corresponding 6 μm spot is marked with a red dot.	117
6.3	Image of an array of spots showing the output of the quality control test applied to each spot, a missing, misprinted and fully printed spot are each highlighted. Missing and misprinted spots are removed from the calculation even if a platelet has adhered at that location.	119
6.4	Images of both labelled fibrinogen and labelled platelets with two spots highlighted, with and without a platelet adhered. The difference in intensity makes it possible to determine the of a platelet.	121

6.5	Two images of a corresponding area using both a cy3 filter and brightfield. The brightfield image shows platelets are clearly visible and match spot locations, indicating platelet labelling is not required for LFD.	122
6.6	Graphical demonstration that combines a mesh alongside the LFD filter. A) Sample image with mesh applied alongside a region highlighting the output of the LFD Filter. B and C) histograms for a single spot detailed the change in output used to classify a spot. The green line shows the curve before the filter is applied and the red line shows the output curve.	123
6.7	Plot of the average curves used during the second pass characterisation. A) Shows the curves for a 5×6 sample array used to calculate the upper and lower bands. The green curve represents no platelets detected, while the red curve (lower average intensity) represents adhered platelets. B) An image of the area averaged with the spots containing platelets circled, alongside a colour image of a filter used to show the operator which spot LFD may select.	124
6.8	The resulting % of occupied spots using different detection methods. Image sets were taken from a single donor and the resulting % of occupied spots calculated using the available methods. . .	125
C.1	Control volume showing mass flow in x direction	141
C.2	Notation for stresses	143
C.3	Control volume showing surface forces in x direction	144
D.1	Block diagram showing software components used to develop image processing software. The user interface talks with the .net framework, from inside a virtual machine, which in turn uses the DirectShow API to acquire images from the camera. . .	147

D.2	Demonstration of the effect of changing the resolution has on the same image.	148
D.3	Example of a 24bit image being converted into a matrix. A threshold is used to select which pixels should be included as part of the feature (1) or set as background (0) within the binary matrix.	149
D.4	Conversion of image acquired from camera into a binary matrix. A) (i) Sample image taken at $t=n$ and masked, (ii) Sample image taken at $t=n+1$ and masked. From the masked images a binary matrix is produced and subtracted to determine the n_p (B). . .	150
D.5	DXF file section describing a polyline. i) Sample showing how a point and bulge can be described within a DXF file. ii) Part of a DXF file containing the [ACDbPolyline] for a sample shape, with the first three codes containing information about the polyline (90, 70 and 43). While the rest of the text contains the vertices (points) used to draw the shape.	152
D.6	User interface and sample DXF stencil.	153
E.1	Rocking table oscillation $\pm 16^\circ$	155
E.2	Comparison of substrates used in both MiPA and iPA. (A) Comparison of glass and Zeonor to determine if a change in substrate material would have a meaningful effect of % platelet adhesion, no significant difference between the two was recorded, with a smaller % adhesion when MiPA is compared to iPA. The glass cover slid and glass slide used, with the area of printed $6\ \mu m$ spots (in red) is also shown.	157

E.3	First generation closed chip layers. Seven layers make up the closed version of the gen1 chip starting with the Zeonor layer cut to size from a bigger sheet, (2) pressure sensitive adhesive (PSA) gasket between the Zeonor and the assay wells, (3) assay wells laser cut from PMMA, (4) PSA filling layer, (5) PMMA spacer layer, PSA gasket between spacer and top layer, (7) PMMA top layer, (8) monovette connector, (9) monovette syringe. The assembled chip is also shown with the transparent PMMA layer and the white PSA gasket and filling layer along the syringe.	158
E.4	Version 1 of the second generation design. The layers shown exclude the PSA gasket between each. As the connector was moved to the side of the chip an additional spacer layer was required. The progress of flow is also shown, starting as the blood leaves the connector and moves along the filling layer before reaching the inlets into the assay well and indicator well at the same time, with the 10 μl filled by the first indicator well and 20 μl of blood added to the assay well by each subsequent well filled.	159
E.5	Version 2 of the second generation design. The layer shown excludes the PSA gasket between each. The connector has been placed at the top of the chip removing the need for a spacer layer. The progress of flow is also shown, starting as the blood enters the holding well reaching the inlets into the delivery layer at the same time, before moving along the filling channels to the outlets of the delivery layer and faintly into the assay wells.	161
E.6		162

F.1	The effects of applying a Gaussian blur to a sample region of a platelet image. 1. Unfiltered region, 2. region after Gaussian blur, 3. region after Gaussian blur, scaling filter and mid-pass filter (MPF) is applied. The effects on the output image are shown when both a threshold filter and edge detection are applied, with an area of the bottom left hand corner (highlighted in red) used to demonstrate some common issues with blob detection. . . .	167
F.2	Details how a mesh is built and fitted to an input image to account for image rotation. A) shows two arrays of spots along with the crosses used as image processing markers, with one array rotated by an angle θ . B) illustrates the lines used to calculate the rotation and therefor the spot locations, an associated mesh is also shown and numbered. C) demonstrates how a mesh is laid over the input image to extract the region around each spot.	168

List of Tables

3.1	List of 13 different geometries characterised. Split into two sets of corresponding footprint areas Set 1 contains channels changing in width from 1 to 4 <i>mm</i> in increments of 0.5 <i>mm</i> while Set 2 contains channels changing in length from 20 to 80 <i>mm</i> in increments of 10 <i>mm</i> . Channel 4 is included in both Sets 1 and 2. The average area of exposed PDMS (AAEP) is also listed alongside the foot print area (FPA) for each set of corresponding channels. AAEP includes all surfaces within the channel, while FPA only includes the top surface and not the side walls of the channel.	66
A.1	List of surface membrane glycoprotein receptors in blood.	135
A.2	Platelet function Analysis Systems	136
C.1	Mass flow table	141
C.2	Table of control fluxes	142